Investigating Stress Concentrations near Boreholes in Anisotropic Formations and the Mechanical Behavior of Drilling-induced Tensile Fractures

by

Qing (Suzie) Jia

A thesis submitted in partial fulfillment of the requirements for the degree of

Master of Science

in

Geophysics

Department of Physics
University of Alberta

Abstract

With the increasing exploitation of unconventional reservoirs, the demands of implementing geomechanics to improve the exploration and development process have been greater than before. Knowledge of *in-situ* stresses and rock failure mechanisms is key for building a comprehensive geomechanical model. Consequently, it is necessary to evaluate the state of stress in the Earth in order to design and efficiently operate engineered geothermal systems. The goal of this study is to investigate the variations of near-wellbore stress concentrations as a function of formation anisotropy, stress regimes and borehole relative orientations with respect to the *in-situ* stress, and then further examine the mechanical behavior of drilling induced tensile fractures. This is done by developing various MATLAB^{TM} based analytical programs, creating numerical models and conducting lab simulations. Results from analytical models demonstrate that effects of formation anisotropy on borehole stress rise with increasing degree of anisotropy and the drilling-induced tensile fractures are not symmetrical when the borehole axis is not aligned with any of the *in-situ* stresses. Those models can also be integrated with different industry data sets to estimate the stress states in the formation of interest and enable us have better insights for drilling optimization, hydraulic fracturing design, completion planning and production maximization. Moreover, in the lab, both axial and *en echelon* drilling-induced tensile fractures were generated and their failure mechanisms agree with the general theory. Numerical models are not fully completed as the final goal is to develop a dynamic 3-D model based upon the current static model to simulate the lab processes in real-time.

Acknowledgement

First, I would like to express my keen appreciation to my supervisor, Dr. Doug Schmitt, for his patience, guidance and support throughout my master study. I am very grateful for the precious opportunity to work on a geomechancis related subject, to know more people in numerous meetings, and to participate in the field work in Fort McMurray. It was you giving me the chance to expand my view and enhance my technical skills. Thank you again for being such a nice and considerate supervisor, not just to me, but to all your students.

This work was funded by Helmholtz-Alberta Initiative (HAI), which is a research collaboration between German and Canadian researchers regarding to geothermal energy. Thank you to all the people organizing this collaboration which made this project possible.

I would also like to express my gratitude to all the members of the Experimental Geophysics Group, especially Randy Kofman and Xiwei Chen for their generous assistance in the laboratory work, and Gautier Njiekak for his help in the Stress Map project. I would like to acknowledge Kristine Haug towards her help in sharing those FMI data from Alberta Geological Survey to me.

Thanks to my parents for their supports no matter how far away I am from home, and my husband for being with me and taking care of me throughout the good times and the bad times. Last but not least, I would like to thank all my friends who have given me all those joyful moments over countless lunch gatherings and casual chats. Thank you, all!

Table of Contents

List of Figures

List of Tables

List of Symbols and Abbreviations

a	Well radius
a_{ij}	Direction cosines
A_{ijkl}	The tensor of compliances
C	Compressibility
C_{ijkl}	The fourth order tensor of elastic constants
C_{Reuss}	The effective compressibility from Reuss's method
C_{Voigt}	The effective compressibility from Voigt method
E_i	Young's modulus
$\boldsymbol{f}_b$	Vector of external body forces
g	Gravitational constant
G	Shear modulus
G_{ij}	Shear modulus
K	Bulk modulus or incompressibility
l_t	Length of drilling-induced tensile fractures on the borehole wall
$\boldsymbol{n}$	Matrix consists of cosines of the outwards normal on the boundary and the bar means the prescribed value of forces
Pa	Pascal
P_P^{hydro}	Hydrostatic pore pressure
P_w	Wellbore Pressure
R	The degree of anisotropy: the ratio between E_h and E_v
S_0	Cohesion
T_0	Tensile strength
V_b	Bulk volume
V_m	Matrix or solid grain volume
V_p	Pore volume
V_P	Velocities of compression waves

V_S	Velocities of shear waves
w	The out-of-plane displacement
z	Depth from the earth surface to the point of interest underground
α	Biot coefficient
σ	Normal stress
τ	Shear stress
Θ	Breakout width
v_{ij}	Poisson's ratio
β_{ij}	Reduced strain coefficients
$\Phi_i(z_i)$	Analytic function
λ	Lame's constant
μ	Coefficient of internal friction
δ_{ij}	The Kronecker detla
ε_{ij}	Strain in the *i-j* plane
ω	Orientation of *en echelon* fractures with respect to the borehole axis
θ_t	Span of drilling-induced tensile fractures on the borehole wall
ρ	Density
ρ_w	Water or seawater density
l, m and *n*	Direction cosines
L_2, L_3 and L_4	Linear differential operators
r, *θ*, and ξ	Cylindrical coordinate system: *r* represents the distance from the borehole axis, *θ* is the azimuth of the point from the *x*-axis and ξ is the vertical position
S_1, S_2 and S_3	The three *in-situ* principal stresses, and $S_1 \geq S_2 \geq S_3$
S_H, S_h and S_v	The maximum horizontal stress, the minimum horizontal stress and the vertical stress
u_x, u_y, and u_z	Displacement in the x, y and z direction
α, β and γ	The Eulerian angles

σ_1, σ_2 and σ_3	Three principal stresses, and $\sigma_1 \geq \sigma_2 \geq \sigma_3$
$\mathfrak{E}$, γ and δ	The Thomsen's anisotropic parameters
ASTM	American Society for Testing and Materials standards
BC	Boundary condition
DFIT	Diagnostic fracture injection test
DITF	Drilling-induced tensile fracture
DOF	Degree of freedom
DST	Drill Stem test
F and Ψ	Stress functions
FBP	Formation breakdown pressure
FCP	Fracture closure pressure
FEM	Finite element method
FPP	Fracture propagation pressure
ISIP	Instantaneous shut-in pressure
L-A	Lekhnitskii-Amadei model
LOP	Leak-off pressure
UCS or C_0	Unconfined compressive strength
VTI	Vertical transversely isotropy
WCSB	Western Canadian Sedimentary Basin
XLOT	Extended leak-off test

Chapter 1

Overview

This thesis is part of the geothermal theme of the Helmholtz-Alberta Initiative (HAI), which is the research collaboration between scientists in Germany and Canada on energy projects for cleaner energy production. Conventional geothermal systems can only exploit formations with sufficient heat, water and permeability to generate power economically. To minimize limitations on site selection, enhanced geothermal systems (EGS) have been widely developed in recent years. This technique can enhance energy productions by hydraulic stimulating hot reservoirs with low water content and low permeability. A proper control on the stimulation process is critical as it has big influences on fracture propagations, fluid migrations and borehole stabilities. Hence, simulating the fracturing process is necessary prior to exploitations, and geomechanical parameters, such as *in-situ* stress states and rock elastic properties, are essential inputs to the simulation process helping us better predict rock behaviors under different circumstances. This motivates us to improve the systematic geomechanical analysis on the fracture characterization and *in-situ* stress estimation in unconventional reservoirs.

A direct method to evaluate stress orientation is through the usage of image logs (Fig. 1.1), which record images of the borehole wall and can reveal a certain kind of property (*e.g.* resistivity, acoustic velocity, etc.) of surrounding formation rocks (*Barton et al.*, 1997; *Chan*, 2013). Fractures identified from borehole images can be utilized to refer the horizontal stress orientations with the assumption that one of the principal stress is in the vertical direction. In addition to stress orientations, the range of stress magnitude can be constrained based on the observations of borehole images. Therefore, knowledge of borehole fracture behaviors is critical, and developing techniques that can link the fracture mechanism with stresses becomes necessary. In this thesis we examine two aspects of this problem: i) the effects of rock anisotropy on stress distributions near boreholes, and ii) the related issue of how such boreholes fail.

In stress analysis, workers rarely take formation anisotropy into consideration; this is in part because it can be difficult to characterize the anisotropy. But, if the trend of developing

unconventional resources usually held within strongly anisotropic rocks continues, there will be a great deal of drilling at all directions through anisotropic formations. Therefore, in this study, I coded in MATLAB™ programs to investigate the impacts of formation anisotropy on borehole stresses and the consequential growth of drilling-induced tensile fractures. Then these programs were also used to validate the numerical model created from a finite element solver, called ANSYS™. This numerical model could be further developed into a dynamic model to compare its results with those obtained from the photoelasticity lab measurements.

The photoelasticity lab tests were designed to simulate the initiation and propagation of drilling-induced tensile fracture and hydraulic fracture. Several glass cubes with identical dimensions were drilled with holes in different orientations. This could help us identify the influence of the relative orientation of borehole axis with respect to the principal stresses on fracture behaviors.

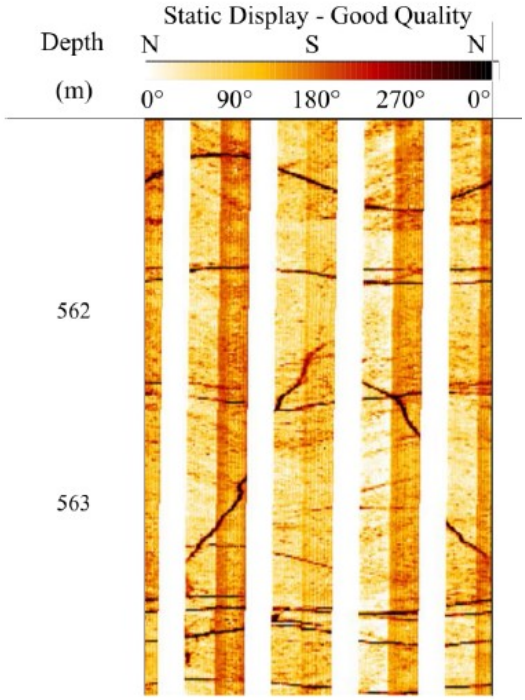

Figure 1.1 An interval of the processed Formation Microimager (FMI) log of the Hunt well demonstrating resistivity changes of the formation on an unwrapped borehole image. Dark color indicates higher conductivity; whereas, brighter color indicates higher resistivity. In this figure, those lines with dark color may represent fractures. Static display means that the colorbar of the

image is consistent throughout the whole well, and does not dynamically change based on different depth intervals. Adapted from *Chan* (2013).

Chapter 2 focuses on introducing some basic principles related to this study. As the objective of this research is to improve techniques for stress estimations, the concept of crustal stresses is first presented including the mathematical expressions, the classification of stress regime and the corresponding measurement for each stress component. This chapter continues with providing some basic information on elasticity related to this research, *e.g.* reviews on the relationship between stress and strain, the effective stress, dominant types of rock intrinsic anisotropy and their constitutive relationships. Last, this chapter ends with revisiting two of the most prevailing modes of rock failure in geomechanics, and they are compressive failure and tensile failure. This section will lay a solid foundation for the following introductions on borehole failure and borehole fractures.

Before moving towards presenting borehole stresses in anisotropic formation, **Chapter 3** first reviews the isotropic scenario, including the analytical solution for the stress distributions around the borehole wall, the borehole failure mechanism and the classifications of borehole fractures. In this section, two MATLAB^{TM} based analytical programs are presented, one enables us to visualize the stress concentration around the borehole in a plain view, and the other shown as lower hemisphere diagrams calculates the tendency of fracture initiations for all possible well orientations. I presented these results at the AGU Fall meeting in 2013 and CSEG Geoconvention in 2014 (*Jia et al.*, 2014). The last section discusses the results of the photoelasticity tests carried out in the laboratory in order to study the mechanical behavior of tensile fractures generated around the borehole wall. These observations provide us with some interesting preliminary qualitative conclusions which can be integrated with the interpretation process for borehole imaging. These results will be presented at the ISRM Congress in 2015 (*Jia et al.*, 2015).

Chapter 4 and **Chapter 5** focus on the investigations of the impacts of formation intrinsic anisotropy on near-wellbore stresses and the consequential fracture traces. First, we revisite the closed-form solutions for borehole stress calculations in an anisotropic formation, which are developed by *Amadei* (1983) and *Lekhnitskii* (1981). Then, based on these solutions, a program

is presented showing the differences in terms of stress magnitude through changing material properties. One thing needs to be mentioned is that even though this program can handle all types of anisotropy, this study only shows the transversely isotropic case, which is expected to be the anisotropic type of shale. Since fracture traces vary with borehole stresses, chapter 5 provides a comprehensive discussion on the manner in which the formation properties affect drilling-induced tensile fracture traces. I presented these results at the 48th US Rock Mechanics/Geomechanics Symposium and the CESG Geoconvention in 2014 (*Jia and Schmitt*, 2014; *Jia et al.*, 2014).

The last part of the work **Chapter 6** shows some preliminary work of our numerical models built in a finite element solver ANSYS^{TM}. This chapter begins with introducing some detailed descriptions about the 3-D model including the model geometry, element attributes, meshing and boundary conditions. The next section illustrates the development of the 3-D from a 2-D simplified model and its validations. This chapter ends with providing a roadmap for future study which aims to create a dynamic 3-D numerical model enabling us to compare the results with those from the photoelasticity tests.

Chapter 7 summarizes all the results from the analytical programs, lab tests and numerical models. Also, some suggestions for future investigations on stress estimations and geothermal system design are included in this chapter.

The **Appendix A** mainly explains the principals of the photoelasicity experiments conducted on glasses. Other **Appendices** are the text version of all my MATLAB^{TM} codes.

References

Amadei, B. (1983), *Rock anisotrpy and the theory of stress measurements*, Springer-Verlag, Berlin.

Barton, C. A., D. Moos, P. Peska, and M. D. Zoback (1997), Utilizing wellbore image data to determine the complete stress tensor: Application to permeability anisotropy and wellbore stability, *The Log Analyst*, *38*(06), 21-33.

Chan, J. (2013), Subsurface geophysical characterization of the crystalline canadian shield in Northeastern Alberta: Implications for geothermal development, M.Sc. Thesis, 259 pp, University of Alberta, Edmonton, Canada.

Jia, Q., and D. R. Schmitt (2014), Effects of formation anisotropy on borehole stress concentrations: implications to drilling induced tensile fractures, 48th US Rock Mechanics / Geomechanics Symposium, American Rock Mechanics Association, Minneapolis, MN, USA, June 1-4.

Jia, Q., D. Schmitt, I. Moeck, and R. Kofman (2014), Improving borehole instability analysis by investigating the impacts of stress and rock anisotropy, CSEG Geoconvention 2014, Calgary, Alberta, May 12-16.

Jia, Q., D. Schmitt, X. Chen, and R. Kofman (2015), Investigating the failure mechanism of drilling induced tensile fractures utilizing transparent glass cubes in the laboratory, ISRM Congress 2015, International Congress on Rock Mechanics, Montreal, Quebec, May 10-13.

Lekhnitskii, S. G. (1981), *Theory of elasticity of an anisotropic body*, Mir Publications, Moscow.

Chapter 2

General Considerations

2.1 Overview

As the trend of enhanced geothermal system exploitations rises, more issues attract people's attention, such as borehole instabilities, stimulation designs and production optimizations. Among all those aspects, geomechanics play a key role. In order to develop a comprehensive geomechanics model, *in-situ* stresses and rock elastic properties are essential inputs. Building a complete crustal stress tensor requires different measuring techniques that are practical to apply during the oil and gas exploitations (*Zoback*, 2007). Section 2.2 reviews some basic points about the characterizations of crustal stresses including the mathematical form of *in-situ* stress, stress transformations among different coordinates, E. M. Anderson's classification in terms of the faulting regime and the measurement techniques for each stress components.

In the next section of this chapter, I briefly introduce the concept of rock elasticity which is of fundamental importance for rock mechanics as the knowledge of rock elastic property is the key for predicting rock behaviors under stresses. First, some terminologies are established and will be used with consistent names throughout the thesis to avoid confusion. Second, poroelasticity describing the elastic behavior of a porous rock saturated with fluids is discussed since pore fluids can influence the response of a rock to an external force. Lastly, four typical types of rock anisotropy and their corresponding constitutive relationships are reviewed.

In the last section of the chapter, several basic principles of rock failure in compression and tension are introduced. A stable well is not one in which not a single well failure is formed. For example, borehole breakouts, a kind of compressive failure, are usually present in the vicinity of the borehole without causing any borehole stability problems when their widths are not large enough to put the well into a floating status; however, without proper mud weight control, they can grow in terms of azimuth leading to borehole stability problems. Therefore, it is important to learn about the rock failure mechanism in order to prevent borehole fracture from growing out of control. In the first section, I discuss the concept of the rock compressive strength and its

corresponding lab measurement methods. From the theoretical perspective, I also address the Mohr-Coulomb failure criterion, which is the most common criterion to predict rock strength as a function of pore pressure and confining pressure. The second part is about rock tensile failure mechanism which is a much simpler failure mode compare to the compressive failure as the rock tensile strength is close to zero. Tensile failure is mainly of application to drilling-induced tensile fractures created at the borehole wall (Chapter 3) and hydraulic fracturing. The former does not harm borehole stability but the latter results from excessive mud weight that can lead to circulation loss. Moreover, all those considerations are based on the assumption that rocks are isotropic, linear elastic, continuous and homogeneous. The anisotropic conditions for borehole compressive and tensile failure are discussed in Chapter 4 and 5.

2.2 Earth Crustal Stress

2.2.1 Stress Notation and Transformation

Stress is a second-rank tensor defined as the distribution of forces on a given area usually expressed in the unit of Pascals (Pa). As illustrated in Fig. 2.1a, for an infinitesimal cube in the Earth's crust at depth the stresses it bears can be classified into two kinds: normal stresses (σ), whose tractions are normal to cube faces, and shear stresses (τ), whose tractions are parallel to the faces. To be more specific, stress is commonly written as the following matrix form:

$$\sigma = \begin{bmatrix} \sigma_{xx} & \tau_{xy} & \tau_{xz} \\ \tau_{yx} & \sigma_{yy} & \tau_{yz} \\ \tau_{zx} & \tau_{zy} & \sigma_{zz} \end{bmatrix} \tag{2.1}$$

where the first subscript indicates the normal of the face on which the stress acts and the second subscript refers to the direction to which the stress points. This stress tensor gives the values for the x-y-z coordinate as shown in Fig. 2.1a. In this and most of the following chapters excepting Chapter 6, a positive stress magnitude indicates compression as is the convention used in geosciences. In other disciplines, such as Physics and Mechanical Engineering, the opposite convention with compression negative is applied. Whether the sign is positive or negative for compression is not important as long as the convention is applied consistently. We assume that the infinitesimal cube is in equilibrium and it is not translating or rotating; this means that forces on it are balanced and with regards to rotation:

$$\tau_{xy} = \tau_{yx}, \tau_{xz} = \tau_{zx}, \tau_{yz} = \tau_{zy} \tag{2.2}$$

so that there are only six independent components in the matrix Eq. 2.1.

The matrix of Eq. 2.2 is called a second-order Cauchy stress tensor and as such the values will change with the frame of references used even though, regardless of the spatial co-ordinate reference, the tensor still carries the same information. To transform between co-ordinate frames, the stress tensor can be rotated via direction cosines (a_{ij}) into different arbitrary coordinate systems, and its magnitude for each component will change against upon the orientation of the coordinate. The direction cosines describe the relative orientation of a newly defined coordinate system with respect to the reference coordinate system (*Jaeger et al.*, 2007). To specify direction cosines, we need three stress magnitudes and three Eulerian angles between the two Cartesian coordinate systems. The mathematical equation is

$$\sigma' = A^T \sigma A \tag{2.3}$$

where A is defined as

$$A = \begin{bmatrix} a_{xx'} & a_{xy'} & a_{xz'} \\ a_{yx'} & a_{yy'} & a_{yz'} \\ a_{zx'} & a_{zy'} & a_{zz'} \end{bmatrix} \tag{2.4}$$

where a_{ij} is the direction cosine. Or it can be written as the following form (*Fjaer et al.*, 2008)

$$\sigma' = R(\alpha, \beta, \gamma)\sigma R^T(\alpha, \beta, \gamma) \tag{2.5}$$

and

$$R(\alpha, \beta, \gamma) = R_z(\alpha)R_y(\beta)R_z(\gamma)$$
$$= \begin{bmatrix} cos\gamma cos\beta cos\alpha - sin\gamma sin\alpha & cos\gamma cos\beta sin\alpha + sin\gamma sin\alpha & -cos\gamma sin\beta \\ -sin\gamma cos\beta cos\alpha - cos\gamma sin\alpha & sin\gamma cos\beta cos\alpha + cos\gamma sin\alpha & sin\gamma sin\beta \\ sin\beta cos\alpha & cos\beta cos\alpha & cos\beta \end{bmatrix} \tag{2.6}$$

where α, β and γ are the Eulerian angles in the 3-D coordinate rotation processes (Fig. 2.2). To simplify the problem, stress tensor is usually rotated into a principal coordinate system x'-y'-z' where all shear stresses disappear (Fig. 2.1b), and the rotated stress tensor can be written as

$$\sigma' = \begin{bmatrix} \sigma_{x'x'} & 0 & 0 \\ 0 & \sigma_{y'y'} & 0 \\ 0 & 0 & \sigma_{z'z'} \end{bmatrix} \tag{2.7}$$

Whereas, for the crustal stress, as the overburden (or vertical stress) is usually one of the principal stresses, the other two principal stresses will be in the horizontal direction. These three principal stresses are orthogonal, and can be written in the following matrix form:

$$\sigma' = \begin{bmatrix} S_H & 0 & 0 \\ 0 & S_h & 0 \\ 0 & 0 & S_v \end{bmatrix} \tag{2.8}$$

where S_H, S_h and S_v are the maximum horizontal compressive stress, the minimum horizontal compressive stress and the vertical compressive stress, respectively. Hence, in order to define the Earth crustal stress under the presumption that the one of the principal stresses remains vertical, four parameters should be defined, and they are the three principal stresses and the azimuthal angle of the maximum or the minimum horizontal stress (*Zoback*, 2007). This concept is assumed to be applicable to the upper crust close to the Earth surface, which is nearly horizontal (*Anderson*, 1951).

The reason that the stress transformation is very important for crustal stress calculations is that because the assumption cannot always be valid. Fluids (i.e., brine and salt) embedded underground cannot support shear tractions; thus, the principal plane becomes tangential to the fluid surface (*Zoback*, 2007). Moreover, stress orientations can also be disturbed around major fault zones, in convergent sedimentary basins and deformed zones (*Bachu et al.*, 2008). Therefore, attention shall be paid on stress directions around complex geological structures as the *in-situ* principal stresses are not necessarily in the horizontal direction or the vertical direction.

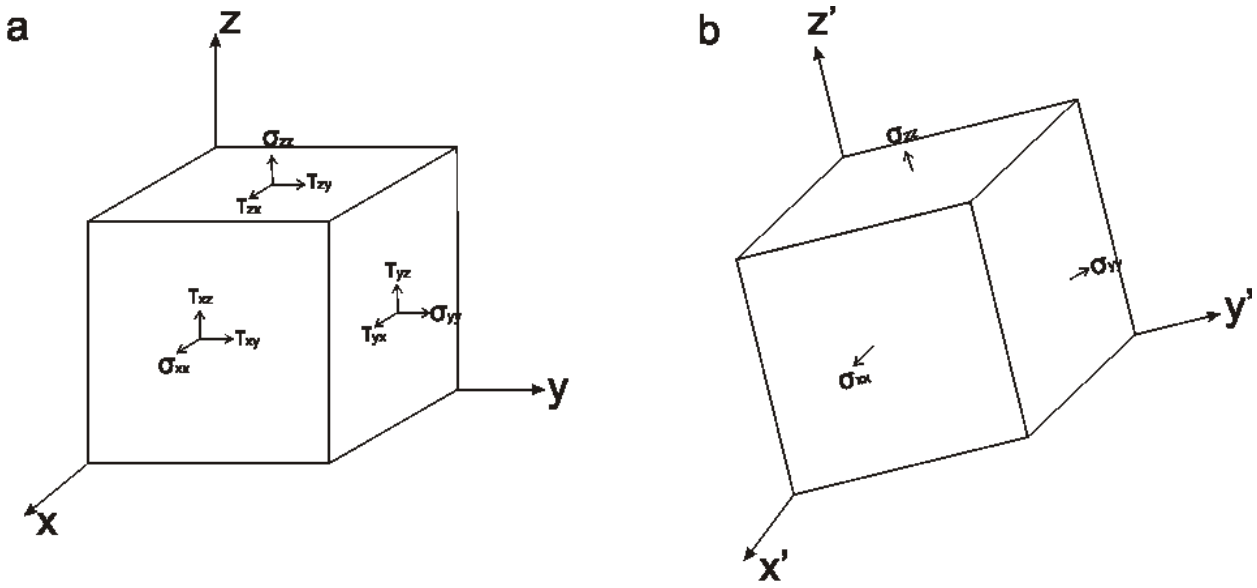

Figure 2.1 a) The stress state of an infinitesimal cube in the Earth's crust showing both normal stresses and shear stresses in the coordinate system x-y-z. b) The stress state after the stress transformation into another arbitrary coordinate system x'-y'-z' in which all shear stresses disappear leaving only three principal stresses acting in the normal direction. Modified from *Schmitt et al.* (2012).

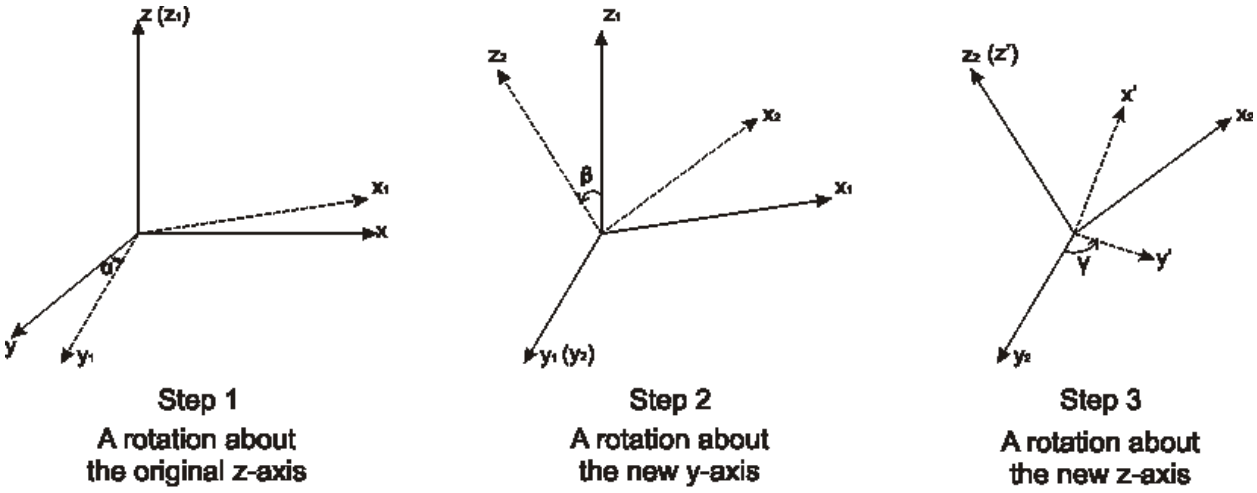

Figure 2.2 Illustration of the coordinate rotation processes in 3-D. The mathematical forms are listed in Eq. 2.5 & 2.6.

2.2.2 Relative Stress Magnitudes in a Sedimentary Basin and their Measurements

As mentioned in the previous section, the principal stresses in the Earth's crust is always considered to consist of the maximum horizontal stress, S_H, the minimum horizontal stress, S_h, and the vertical stress, S_v. As shown in Fig. 2.3, other than those three external stresses, a rock volume in the Earth is also subjected to its own internal pressure, which is referred to as pore pressure caused by the existence of pore fluids. Pore pressure provides an opposite stress effect with respect to the external pressure.

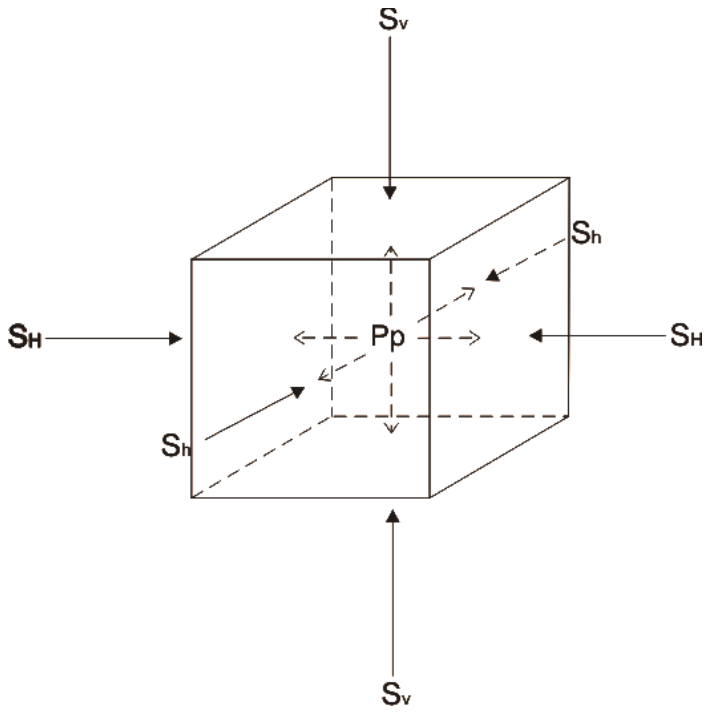

Figure 2.3 The stress state on an infinitesimal rock volume in the Earth. It is under both external stresses (three *in-situ* principal stresses) and an internal stress (pore pressure).

The relative magnitudes of the three principal *in-situ* stresses with respect to one another are critical to crustal movements and fault styles. In order to differentiate different scenarios, *Anderson* (1951) proposed three faulting regimes based on the relative magnitude of Sv with respect to the horizontal stresses, and they are referred to as (Fig.2.4):

1) Normal faulting regime: Sv is the maximum principal stress, S_1.
2) Strike-slip faulting regime: Sv is the intermediate principal stress, S_2.
3) Reverse faulting regime: Sv is the minimum principal stress, S_3.

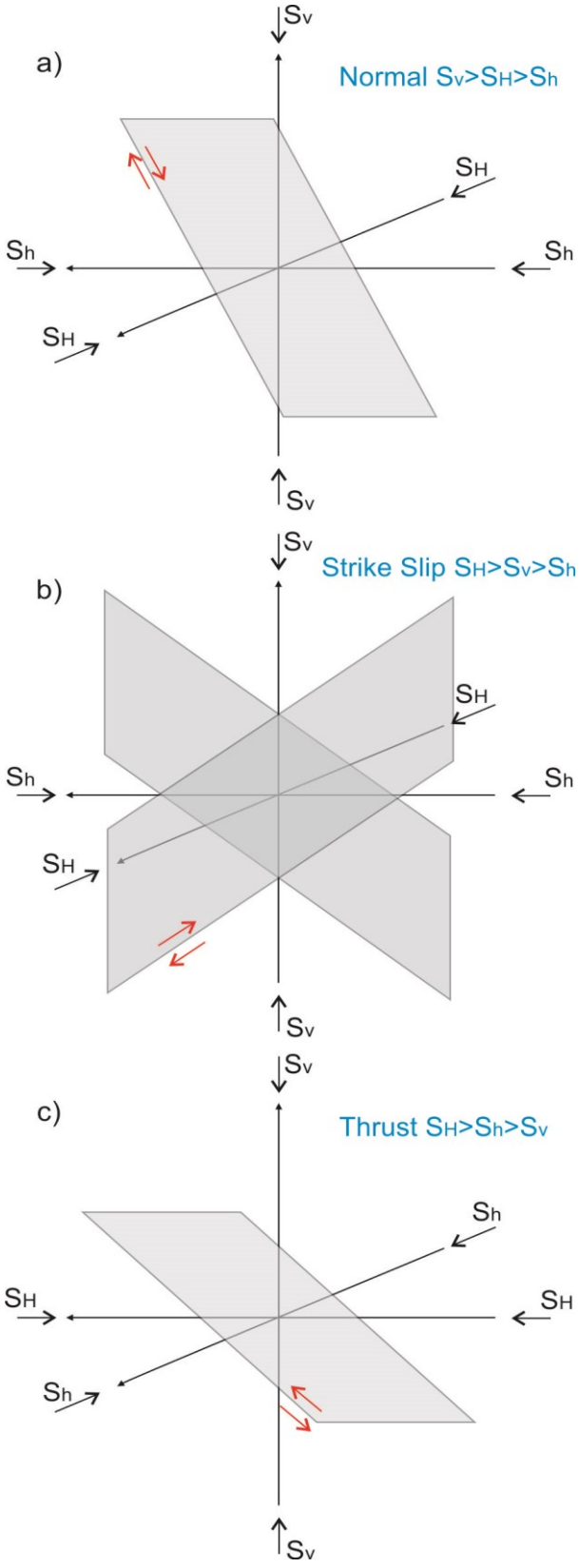
a)
Normal Sv>SH>Sh
Sv
SH
Sh
Sh
SH
Sv
b)
Strike Slip SH>Sv>Sh
Sv
SH
Sh
Sh
SH
Sv
c)
Thrust SH>Sh>Sv
Sv
Sh
SH
SH
Sh
Sv

Figure 2.4 E. M. Anderson's classification for stress regimes: a) normal faulting environment with normal faults dipping ~60°; b) strike-slip faulting environment with strike-slip faults; c) reverse faulting, also often called thrust faulting environment with thrust faults dipping ~30°. Red arrows indicate the movement direction of the hanging wall and the foot wall. Modified from *Schmitt et al.* (2012).

The magnitude of Sv is the integration of rock densities, ρ, from the Earth surface to the depth, z:

$$S_v = \int_0^z \rho(z)\, g dz \tag{2.9}$$

where g is the gravitational constant. For typical siliciclastic sedimentary rocks, the gradient will be around 23MPa/km (*Zoback*, 2007). If the area of interest is offshore, the weight of water upon the seafloor needs to be taken into consideration as well, so that the gradient of Sv in the seawater interval will be a bit higher than 10MPa/km. Sv is the easiest stress to be estimated comparing to the other two principal stresses. A direct way is by using density logs, which should be as complete as possible; if not, other estimates need to be made. Moreover, rock density generally increases with depth due to compaction, and as such, the gradient of Sv is also increasing, this has been observed in most sedimentary basins.

Pore pressure is crucial for hydraulic fracture design, drilling risk assessments and caprock integrity analyses. Special attention should be paid when dealing with an overpressured reservoir as both the shear failure and the tensile failure can be generated more easily. Pore pressure can be hydrostatic, P_P^{hydro}, when the depth of interest is hydraulically interconnected to the surface through pore and fracture network, and it can be written as (*Zoback*, 2007):

$$P_P^{hydro} = \int_0^z \rho_w\,(z) g dz \tag{2.10}$$

where ρ_w is water density. So this can be implied as the pressure is generated by the water from the surface to the depth of interest. However, if the pore volume is confined, pore pressure will exceed the hydrostatic value. Theoretically, the rock tensile strength is always negligible, and pore pressure should be smaller than the minimum horizontal stress; otherwise, hydraulic fracture will occur. Pore pressure can be determined directly from drill stem tests (DST), diagnostic fracture injection test (DFIT) and wireline formation tests (*Reis et al.*, 2013), or

estimated from seismic data (*Carcione et al.*, 2003; *Eaton*, 1975; *Sayers et al.*, 2002). But for shale formation, it is not reliable to use direct measurement; thus, the pore pressure extrapolation method becomes necessary (*Reis et al.*, 2013).

The azimuth of S_h can be determined from earthquake focal mechanisms, wellbore images, caliper logs and recent geologic indicators (*Zoback*, 2007). The magnitude of S_h can be estimated by various hydraulic fracturing methods in both normal and strike-slip stress regimes in which S_h is the minimum principal stress. These methods are micro-fracture tests, mini-fracture tests, extended leak-off tests and massive hydraulic fracturing (*Bachu et al.*, 2008; *Hawkes et al.*, 2005; *Zoback*, 2007). Such tests involve processes of fluid injections with certain rates generating fractures in the formation of interest. Based on the reliability of previously measured data and test procedures, the accuracies of those tests decrease from the micro-fracture test to the massive hydraulic fracturing (*Bell and Bachu, 2003*).

Before proceeding to the detailed descriptions of these fracture treatment tests, some concepts indicated in Fig. 2.5 should be defined. The leak-off pressure (LOP) is the moment that the fluid starts to leak-off into the formation leading to a deviation of the data points from the initial straight line (*Bachu et al.*, 2008; *Raaen et al.*, 2006). After the LOP, the formation is kept pressurized until reaching the peak pressure during the whole process, defined as the formation breakdown pressure (FBP), which is followed by an instant drop in pressure indicating a larger volume of leak-off fluid into the fractures compared to the volume of pump-in fluid (*Raaen et al.*, 2006; *Schmitt et al.*, 2012; *Zoback*, 2007). Then the pressure curve stays in a plateau, and the corresponding pressure is referred to as the fracture propagation pressure (FPP). The instantaneous shut-in pressure (ISIP) is the pressure right after the moment the pumping stops, while the fracture closure pressure (FCP) corresponds to the pressure at the moment of fracture closing (*Raaen et al.*, 2006).

During micro-fracture tests, low viscosity fluids are injected in a low rate within a small interval of formation through perforation or open hole to open and close a tensile fracture several times until a fairly constant fracture closure pressure is observed (*Bell*, 2006). But since the micro-fracture method is expensive, it is not widely-used in the Western Canadian Sedimentary Basin (WCSB). Similar to micro-fracturing, mini-fracture tests evolves fluids with high viscosity injected rapidly into formations to record closure pressure (*Bachu et al.*, 2008). As a viscous

fluid is utilized, larger friction losses will cause a higher value of FPP; thus, the magnitude of S_h is better to be interpreted as the value of the FCP (*Zoback*, 2007).

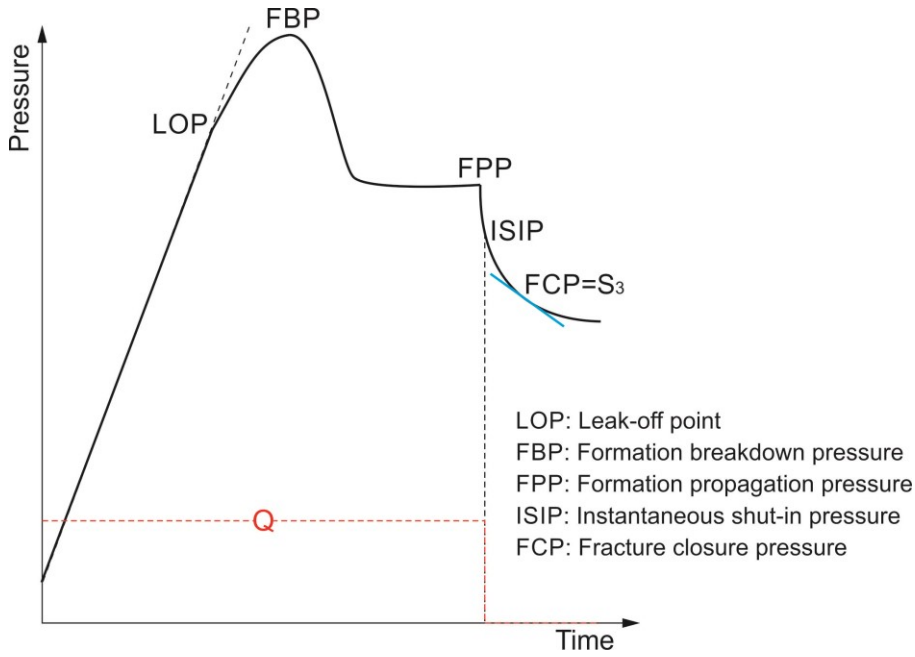

Figure 2.5 A typical micro/mini-frac or extended leak-off test record showing pressure versus time. Modified after *Gaarenstroom et al.* (1993).

The conventional leak-off test is stopped once leak-off pressure, P_{lo}, is recorded in an open hole; thus, it is impossible to estimate the instantaneous shut-in pressure (ISIP) and the fracture closure pressure (*Hawkes et al.*, 2005). If a pre-existing or induced fracture is perpendicular to the minimum horizontal stress before the test, then the leak-off pressure is approximately equivalent to S_h as this test becomes a fracture reopening process (*Bachu et al.*, 2008). Otherwise, in order to equate the LOP as S_h, the tests are required to be conducted in an in-gauge impermeable borehole and the formation of interest is assumed to act elastically during pressurization (*Addis et al.*, 1998). As those required factors are hard to control, LOTs usually lead to overestimations for S_h (*Addis et al.*, 1998; *Hawkes et al.*, 2005).

Comparing to the conventional leak-off tests, extended three-cycle leak-off tests are more preferable to estimate S_h, but they are rarely conducted (*Addis et al.*, 1998; *Bachu et al.*, 2008). Extended leak-off tests (XLOTs) are conducted similar to LOTs during the first cycle. A constant FPP is observed on the next two more cycles since the tensile strength of the formation

and the borehole stresses have already been overcome in the first cycle (*Addis et al.*, 1998). And the ISIPs achieved on second and third cycles provide good estimations of the S_h (*Addis et al.*, 1998). On the other hand, the formation breakdown pressure obtained during massive hydraulic fracturing which breaks down formations and generates enormous fractures provides the least accurate result (*Bachu et al.*, 2008; *Bell and Bachu*, 2003; *Haimson and Fairhurst*, 1969).

The magnitude of S_H is the most difficult component to derive within the full stress tensor. This is the final step for stress estimations; in other words, all other stress values and rock elastic properties should be constrained in order to estimate S_H. A general bound can be achieved using stress polygon, but this is not important for this study, so that we won't discuss it specifically here. An alternative method is based on observations of wellbore failures from image logs (Chapter 3). This study combines theoretical models with image log data to further study the mechanical behavior of borehole failures under different stress regimes and formation types.

So far, numerous studies have been conducted to analyze the stress state in the WCSB (*Bachu et al.*, 2008; *Bell*, 2006; *Bell and Gough*, 1979; *Bell and Bachu*, 2003; 2004; *Bell et al.*, 1994; *Grasby et al.*, 2012; *Hawkes et al.*, 2005; *McLellan*, 1987; *Reiter et al.*, 2014; *Teichrob et al.*, 2010). The most accurate method for determining S_h magnitude is the mini/micro-frac test. For estimating S_h azimuth, the widely used approach is through the observations of borehole failure using image logs. Moreover, systematic stress mapping was carried out generating some stress maps in Paleozoic and Mesozoic rocks in WCSB (*Bell*, 2006; *Bell and Bachu*, 2003; *Bell et al.*, 1994).

2.3 Elasticity

2.3.1 Overview

Elasticity is the ability of a material to support external forces and recover from the resulting deformations, which is the building-block for rock mechanics (*Fjaer et al.*, 2008). The simplest type of elasticity is linear elasticity where the relationship between the forces and the corresponding deformations is linear and the deformation is fully recoverable (*Timoshenko and Goodier*, 1970; *Zoback*, 2007). The most basic concepts in elasticity are stress and strain which are introduced in Section 2.2 and Section 2.3.2, respectively. Some elastic moduli relating

stresses and strains and their dynamic measurements are discussed in Section 2.3.3. A porous elastic rock saturated with pore fluids behaves significantly different than a simple conceptualized non-porous solid rock as the pore fluid has profound effects on the rock elastic behaviors. The theory of poroelasticity discussed in Section 2.3.4 describes the behavior of a porous rock under external forces. Most rocks present anisotropic properties to some extent. Elastic anisotropy can influence a rock elastic behavior in several aspects, such as elastic wave propagations, stress distributions (Chapter 4), and failure mechanisms (Chapter 5). In Section 2.3.5, we introduce four of the most typical intrinsic formation anisotropy and their corresponding constitutive relationships; moreover, shale elastic properties will be discussed as well.

2.3.2 Strain

A sample can be shifted by being applied with an external force (Fig. 2.6). The position of a specific particle within this sample is denoted as (x, y, z). After the action of the force, the new position becomes (x', y', z') with the displacements in x, y, z directions by u_x, u_y, u_z, respectively. Therefore, the new position can be expressed as (*Fjaer et al.*, 2008)

$$x' = x - u_x$$
$$y' = y - u_y$$
$$z' = z - u_z \tag{2.11}$$

If the signs of the displacements are positive, the particle is shifted in the negative direction of the axes, and vice versa.

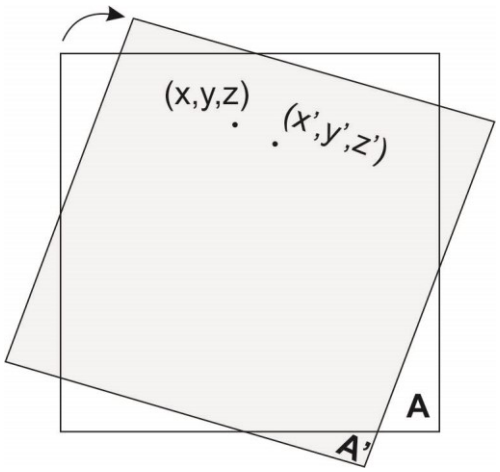

Figure 2.6 The deformation of a sample.

However, in rock mechanics, the use of stress and strain is more preferable, rather than the use of force and displacement. Strain is a relative measurement in terms of the displacement instead of the absolute value. This term can be explained in one dimension. As shown in Fig. 2.7, a one-dimensional fiber with a length of L is shifted in the x direction. Initially, its left point is in the position of x and its right is in the position of $x+L$. After the action of force, its left and right edge are at the position of x-$u(x)$ and $x+L$-$u(x+L)$, respectively. The current length of the bar has been changed by ΔL. Hence the linear strain is

$$\varepsilon = \frac{\Delta L}{L} = \frac{L-\{[x+L-u(x+L)]-[x-u(x)]\}}{L} = \frac{u(x+L)-u(x)}{L} \tag{2.12}$$

In this case, following our compressive stress positive sign convention, the shortening of the bar is defined as a positive strain; whereas, extension of the bar is defined as a negative strain. If the bar is considered to be infinitesimal, the strain at point x is (*Jaeger et al.*, 2007)

$$\varepsilon(x) = \lim_{L\to 0}\frac{\Delta L}{L} = \lim_{L\to 0}\frac{u(x+L)-u(x)}{L} = \frac{du_x}{dx} \tag{2.13}$$

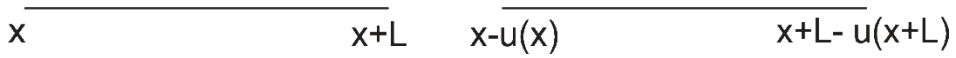

Figure 2.7 Displacement of a fiber in a material whose length can change in one dimension to define the strain.

And in two dimensions, the strain, ε_{ij}, is

$$\varepsilon_{ij} = \frac{1}{2}\left(\frac{\partial u_i}{\partial j} + \frac{\partial u_j}{\partial i}\right) \tag{2.14}$$

where i and j represent axis directions, u_i and u_j are the displacement with respect to i and j axes. Thus the complete strain matrix in two dimensions can be written as (*Jaeger et al.*, 2007)

$$\varepsilon = \begin{bmatrix} \varepsilon_{xx} & \varepsilon_{xy} \\ \varepsilon_{yx} & \varepsilon_{yy} \end{bmatrix} = \begin{bmatrix} \frac{\partial u_x}{\partial x} & \frac{1}{2}\left(\frac{\partial u_x}{\partial y} + \frac{\partial u_y}{\partial x}\right) \\ \frac{1}{2}\left(\frac{\partial u_y}{\partial x} + \frac{\partial u_x}{\partial y}\right) & \frac{\partial u_y}{\partial y} \end{bmatrix} \tag{2.15}$$

For a two-dimensional sample under uniaxial compression, as illustrated in Fig. 2.8 (left), its strain components are listed as the following:

$$Axial\ Strain \qquad \varepsilon_{xx} = \frac{\partial u_x}{\partial x} \tag{2.16}$$

$$Lateral\ Strain \qquad \varepsilon_{yy} = \frac{\partial u_y}{\partial y} \tag{2.17}$$

On the other hand, a sample under a simple shear stress (Fig. 2.8 right) mainly has shear strain, and it can be written as (*Barber*, 2010)

$$\varepsilon_{yx} = \varepsilon_{xy} = \frac{1}{2}\left(\frac{\partial u_y}{\partial x} + \frac{\partial u_x}{\partial y}\right) \tag{2.18}$$

One thing should be noted is that 'engineering strains' are often used in most literatures, which are defined as $\gamma_{xy} = 2\varepsilon_{xy}$ and $\gamma_{xx} = \varepsilon_{xx}$ as these are the ones we actually measure.

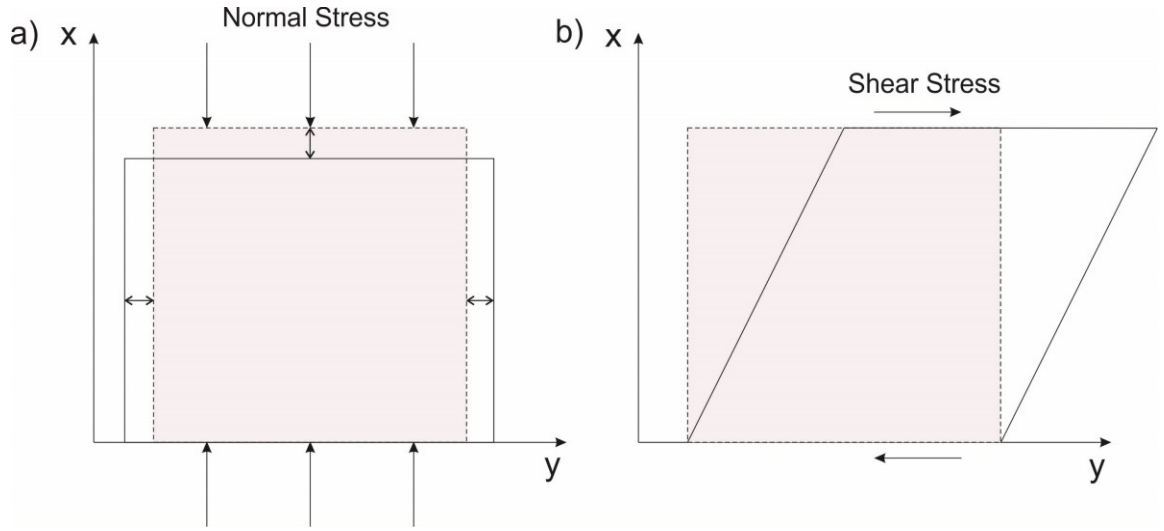

Figure 2.8 Different types of deformations for a two-dimensional sample under a) the normal stress and b) the shear stress.

2.3.3 Elastic Moduli and Elastic Wave Propagation

In this section, we only consider intact and homogeneous elastic materials, which behave linearly, under the application of external forces in three dimensions. The deformation can be fully recovered after stress relaxation. In uniaxial compression without any confinement (force is only in the *i*-direction), the relationship between stress and strain can be expressed in terms of Young's modulus, which can be written as the following

$$E_i = \frac{\sigma_{ii}}{\varepsilon_{ii}} \tag{2.19}$$

where all other stresses except σ_{ii} equal to zero. Note that double subscriptions do not imply Einstein summation convention; instead, they refer to the stress in the normal direction and the strain in the same direction. Poisson's ratio, v_{ij}, relates to the ratio of the strain along the axis *j* and *i* with the stress applied along axis *i (Jaeger et al., 2007)*

$$v_{ij} = \frac{-\varepsilon_{jj}}{\varepsilon_{ii}} \tag{2.20}$$

For an isotropic material, stress can be related to strain through elastic moduli as follows (*Timoshenko and Goodier*, 1970)

$$\sigma_{ij} = \lambda\delta_{ij}\varepsilon_{00} + 2G\varepsilon_{ij} \tag{2.21}$$

where λ is the Lame's constant, ε_{00} equals to $\sigma_{11} + \sigma_{22} + \sigma_{33}$, and G_{ij} is the shear modulus, is given by

$$G_{ij} = \frac{1}{2}\left(\frac{\sigma_{ij}}{\varepsilon_{ij}}\right) \tag{2.22}$$

and δ_{ij} is the Kronecker detla, can be defined as

$$\delta_{ij} = 1 \quad i = j$$

$$\delta_{ij} = 0 \quad i \neq j \tag{2.23}$$

Upon expansion, Eq. 2.21 can be written in the *x, y, z* coordinate system as

$$\sigma_{xx} = (\lambda + 2G)\varepsilon_{xx} + \lambda\varepsilon_{yy} + \lambda\varepsilon_{zz}$$

$$\sigma_{yy} = \lambda\varepsilon_{xx} + (\lambda + 2G)\varepsilon_{yy} + \lambda\varepsilon_{zz}$$

$$\sigma_{zz} = \lambda\varepsilon_{xx} + \lambda\varepsilon_{yy} + (\lambda + 2G)\varepsilon_{zz}$$

$$\tau_{yz} = 2G\varepsilon_{yz}$$

$$\tau_{xz} = 2G\varepsilon_{xz}$$

$$\tau_{xy} = 2G\varepsilon_{xy} \tag{2.24}$$

Additionally, K is another common elastic modulus, called bulk modulus or incompressibility, representing the stiffness of a material under hydrostatic compression, and it can be given as the ratio of the mean stress, σ_{00}, relative to the volumetric strain, ε_{00}

$$K = \frac{\sigma_{00}}{\varepsilon_{00}} = \frac{\frac{1}{3}(\sigma_{11}+\sigma_{22}+\sigma_{33})}{\varepsilon_{11}+\varepsilon_{22}+\varepsilon_{33}} \tag{2.25}$$

And the corresponding compressibility is

$$C = \frac{1}{K} \tag{2.26}$$

Elastic moduli can be estimated using static laboratory measurements, which change slowly with time; whereas dynamic measurements utilize wave velocities, which change rapidly with time. Although those two methods are distinguished from each other, their relationships can be established empirically but great care needs to be taken in such applications. A further complication is that static and dynamic measurements are isothermal or adiabatic, respectively; and the differences between the isothermal and adiabatic bulk moduli can be significant in some cases particularly if the sample holds fluids (*Schmitt*, 2014).

The elastic moduli can be determined based on the velocities of compression waves, V_P, and shear waves, V_S. The equations are given as following (*Mavko et al.*, 2009)

$$V_P = \sqrt{\frac{K+4G/3}{\rho}} \tag{2.27}$$

$$V_S = \sqrt{\frac{G}{\rho}} \tag{2.28}$$

Since fluids cannot bear any shear force, G and V_S are both zero in fluids.

2.3.4 Poroelasticity: Effective Stress

The poroelasticity theory for consolidated rocks is developed based on the conceptual model of porous rocks: an interconnected porous system filled with fluids having a volume relatively small compared to the volume of the whole system exists inside the formation rocks (*Jaeger et al.*, 2007; *Zimmerman*, 1991). If the porous system is not interconnected, the fluid inside these isolated vugs cannot flow under the application of external pressure providing zero contribution to the drainage process (*Jaeger et al.*, 2007). For unconsolidated rocks, the poroelastic behavior is similar to the case for soils and will not be considered in this study.

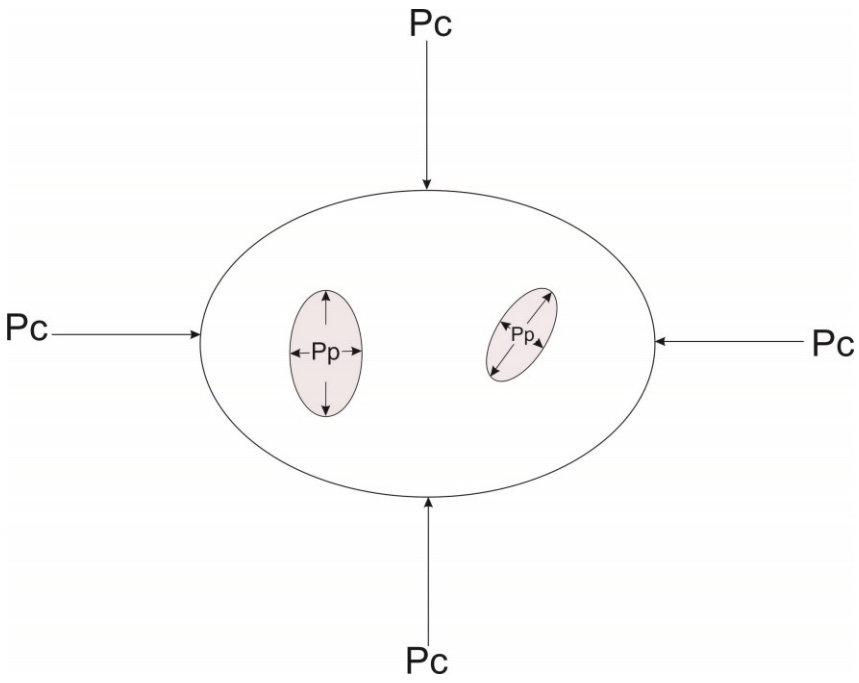

Figure 2.9 Illustration of the influence of pore fluids on the effective stress. *Pc*, the confining pressure, and *Pp*, the pore pressure. Shaded area is the pore space inside a solid grain.

For a consolidated porous rock, as shown in Fig. 2.9, its bulk volume is V_b, its pore volume is V_p and its solid grain volume is V_m, therefore,

$$V_b = V_m + V_p \tag{2.29}$$

To quantify its porous space relative to the whole grain, porosity is introduced as

$$\phi = V_p/V_b \tag{2.30}$$

Because of its simplicity, a popular method to estimate the effective compressibility of a rock is the Voigt-Reuss-Hill which provides bounds to the moduli of a mixture of components. For a solid rock containing different materials, under a uniform pressure over its outer surface, the stress and deformation of each grain may not be the same (*Zimmerman*, 1991). However, to simplify the problem, Reuss's method (*Hill*, 1952) assumes the state of stress stays the same in the whole rock body and the displacement discontinuity is ignored. The effective compressibility of the whole rock is

$$C_{Reuss} = (1-\phi)C_s + \phi C_f \tag{2.31}$$

where C_s is the compressibility of the solid frame, and C_f is the compressibility of the pore fluid.

Thus, Eq. 2.25 can be rewritten as (*Fjaer et al.*, 2008)

$$\varepsilon_{00} = (1-\phi)\frac{\sigma_{00}}{K_s} + \phi\frac{\sigma_{00}}{K_f} \tag{2.32}$$

where K_s and K_f are the intrinsic bulk modulus of the solid itself and the bulk modulus of the pore fluid, respectively. And the effective bulk modulus of the mixture, K_{eff}, is

$$\frac{1}{K_{eff}} = \frac{1-\phi}{K_s} + \frac{\phi}{K_f} \tag{2.33}$$

On the other hand, Voigt method (*Hill*, 1952) assumes the strains are the uniform for all grains. The effective compressibility of the whole rock is

$$C_{Voigt} = \left[\frac{(1-\phi)}{C_s} + \frac{\phi}{C_f}\right]^{-1} \tag{2.34}$$

The Voigt and Reuss methods provide the upper and lower bounds of the actual effective compressibility, as the experimental results always stay in between these bounds (*Hill*, 1952). To find the most accurate results, it is better to use the Voigt-Reuss-Hill method, which utilizes the average of these two bounds. Again, these are bounds and should be used with care.

There are two kinds of tests when dealing with porous media, the drained test and the undrained test. For the drained test, the pore fluid is allowed to flow out of the porous sample during loading; hence, the pore pressure isn't changing with time, and the stress-strain curve can be conceptualized as

$$\sigma_{00} = K_{fr}\varepsilon_{00} \tag{2.35}$$

where K_{fr} is the drained bulk modulus of the porous medium's framework. Eq. 2.32 shows that the deformation is proportional to the total stress for a drained system. However, it is not the case for an undrained system as the fluid cannot escape during loading. The effective stress for volumetric deformation represents the actual stress is applied on the solid material after subtracting the stress carried by the pore fluid, which is defined by (*Schön*, 2011)

$$\sigma'_{ij} = \sigma_{ij} - \delta_{ij}\alpha p_f \tag{2.36}$$

Since δ_{ij} is the Kronecker symbol, we can infer that pore pressure can only affect normal stresses, not shear stresses. Moreover, α is called Biot coefficient (*Nur and Byerlee*, 1971)

$$\alpha = 1 - \frac{K_{fr}}{K_s} \tag{2.37}$$

On the other hand, the bulk modulus of the undrained system, *K*, is defined by the Gassmann equation (*Gassmann*, 1951)

$$K = K_{fr} + \frac{K_f}{\phi}\frac{\left(1-\frac{K_{fr}}{K_s}\right)^2}{1+\frac{K_f}{\phi K_s}\left(1-\phi-\frac{K_{fr}}{K_s}\right)} \tag{2.38}$$

2.3.5 Anisotropy

2.3.5.1 Introduction

The general assumption in the common practice is that rocks are isotropic, homogeneous, continuous and linearly elastic. However, most rocks are to some extent anisotropic, heterogeneous, discontinuous, nonlinear, and inelastic. Anisotropy means the properties of a material vary with direction. Heterogeneity means that the properties of a material are non-uniform from point to point. A medium is discontinuous if there are sharp discontinuities in the stress field within a sample that may result from faults and fractures (*Amadei*, 1983). Anisotropy in sedimentary rocks may be the result of textural anisotropy (i.e., shale formation), layering or preferred orientation of an isotropic mineral (i.e., flat-lying platelets) of pore texture and cracks (*Thomsen*, 1986). *Barla* (1974) proposed a classification for anisotropic rocks that consists of two parts: Class A and B. Class A refers to the intrinsically isotropic rocks that display anisotropic properties (as might be induced for example by the *in-situ* state of stress). On the

contrary, Class B rocks are intrinsically anisotropic and showing apparent anisotropic properties. The objective of this section is to review the constitutive relations for Class B rocks with a focus on shales, and the content is mainly based on the earlier studies conducted by *Amadei* (1983), *Ong* (1994) and *Thomsen* (1986).

2.3.5.2 Generalized Hooke's Law

For an anisotropic, linearly elastic, homogeneous and continuous medium, the constitutive relation can be described as follows

$$\sigma_{ij} = C_{ijkl}\varepsilon_{kl} \tag{2.39}$$

which is the generalized Hooke's law. C_{ijkl} is the fourth order tensor of elastic constants with 81 independent components ($1 \leq i, j, k, l \leq 3$). However, due to the symmetrical properties of both strain and stress tensors ($\sigma_{ij} = \sigma_{ji}$ and $\varepsilon_{kl} = \varepsilon_{lk}$), C has the right and left minor symmetries leading to only 36 components, implying

$$C_{ijkl} = C_{jikl} \quad and \quad C_{ijkl} = C_{ijlk} \tag{2.40}$$

The number of components can be further reduced to 21 if a strain energy function (the change of internal strain energy is balanced with the external forces) is assumed to exist, thus (*Lekhnitskii*, 1981)

$$C_{ijkl} = C_{klij} \tag{2.41}$$

For problems in the x, y, z coordinate system, Eq. 2.39 can be rewritten as the following matrix form

$$\begin{pmatrix} \sigma_{xx} \\ \sigma_{yy} \\ \sigma_{zz} \\ \tau_{yz} \\ \tau_{zx} \\ \tau_{xy} \end{pmatrix} = \begin{pmatrix} C_{11} & C_{12} & C_{13} & C_{14} & C_{15} & C_{16} \\ C_{12} & C_{22} & C_{23} & C_{24} & C_{25} & C_{26} \\ C_{13} & C_{23} & C_{33} & C_{34} & C_{35} & C_{36} \\ C_{14} & C_{24} & C_{34} & C_{44} & C_{45} & C_{46} \\ C_{15} & C_{25} & C_{35} & C_{45} & C_{55} & C_{56} \\ C_{16} & C_{26} & C_{36} & C_{46} & C_{56} & C_{66} \end{pmatrix} \begin{pmatrix} \varepsilon_{xx} \\ \varepsilon_{yy} \\ \varepsilon_{zz} \\ \gamma_{yz} \\ \gamma_{zx} \\ \gamma_{xy} \end{pmatrix} \tag{2.42}$$

The inverse form of Eq. 2.39 is represented by the tensor of compliances, A_{ijkl}, as follows

$$\varepsilon_{ij} = A_{ijkl}\sigma_{kl} \tag{2.43}$$

To have an insight into the physical meanings of compliances, Eq. 2.42 can be given as the following form (*Lekhnitskii*, 1981; *Ong*, 1994)

$$\begin{pmatrix} \varepsilon_{xx} \\ \varepsilon_{yy} \\ \varepsilon_{zz} \\ \gamma_{yz} \\ \gamma_{zx} \\ \gamma_{xy} \end{pmatrix} = \begin{pmatrix} \frac{1}{E_x} & \frac{-\upsilon_{yx}}{E_y} & \frac{-\upsilon_{zx}}{E_z} & \frac{\eta_{x,yz}}{G_{yz}} & \frac{\eta_{x,xz}}{G_{xz}} & \frac{\eta_{x,xy}}{G_{xy}} \\ \frac{-\upsilon_{xy}}{E_x} & \frac{1}{E_y} & \frac{-\upsilon_{zy}}{E_z} & \frac{\eta_{y,yz}}{G_{yz}} & \frac{\eta_{y,xz}}{G_{xz}} & \frac{\eta_{y,xy}}{G_{xy}} \\ \frac{-\upsilon_{xz}}{E_x} & \frac{-\upsilon_{yz}}{E_y} & \frac{1}{E_z} & \frac{\eta_{z,yz}}{G_{yz}} & \frac{\eta_{z,xz}}{G_{xz}} & \frac{\eta_{z,xy}}{G_{xy}} \\ \frac{\eta_{yz,x}}{E_x} & \frac{\eta_{yz,y}}{E_y} & \frac{\eta_{yz,z}}{E_z} & \frac{1}{G_{yz}} & \frac{\mu_{yz,xz}}{G_{xz}} & \frac{\mu_{yz,xy}}{G_{xy}} \\ \frac{\eta_{xz,x}}{E_x} & \frac{\eta_{xz,y}}{E_y} & \frac{\eta_{xz,z}}{E_z} & \frac{\mu_{xz,yz}}{G_{yz}} & \frac{1}{G_{xz}} & \frac{\mu_{xz,xy}}{G_{xy}} \\ \frac{\eta_{xy,x}}{E_x} & \frac{\eta_{xy,y}}{E_y} & \frac{\eta_{xy,z}}{E_z} & \frac{\mu_{xy,yz}}{G_{yz}} & \frac{\mu_{xy,xz}}{G_{xz}} & \frac{1}{G_{xy}} \end{pmatrix} \begin{pmatrix} \sigma_{xx} \\ \sigma_{yy} \\ \sigma_{zz} \\ \tau_{yz} \\ \tau_{zx} \\ \tau_{xy} \end{pmatrix} \tag{2.44}$$

where

1) E_i is the Young's Modulus to the direction of *i*;
2) υ_{ij} is the Poisson's ratio representing the ratio of the strain in the *j*-direction to the strain in the *i*-direction with an external force applying in the *i*-direction;
3) G_{ij} is the shear modulus for *i-j* plane;
4) $\mu_{ij,kl}$ characterizes that the shear in the *i-j* plane induces the tangential stress in the *k-l* plane;
5) $\eta_{i,kl}$ is the coefficient of mutual influence of the first kind representing the stretching in the *k*-direction induced by shear stresses applying in the *i-j* plane; whereas, $\eta_{ij,k}$ is the coefficient of mutual influence of the second kind characterizing a shear in the *i-j* plane generated by the normal stress acting in the *k*- direction.

If a medium contains any symmetry, the components of the compliance tensor can be reduced to be less than 21. In this study, four types of symmetry will be discussed:

1) One plane of elastic symmetry (monoclinic case);
2) Three orthogonal planes of elastic symmetry (orthotropic case);

3) One rotational axis of elastic symmetry (hexagonal or transversely isotropic case);

4) Complete symmetry (isotropic case).

One Plane of Elastic Symmetry if the elastic properties within a medium show reflected image of one another with respect to a plane, this medium has one plane of elastic symmetry. If the *x-y* plane is the symmetry plane, then

$$a_{4i} = a_{5i} = a_{46} = a_{56} = 0, \;\; i = 1,2,3 \tag{2.45}$$

Therefore, the constitutive relation is reduced to 13 independent components

$$\begin{pmatrix} \varepsilon_{xx} \\ \varepsilon_{yy} \\ \varepsilon_{zz} \\ \gamma_{yz} \\ \gamma_{zx} \\ \gamma_{xy} \end{pmatrix} = \begin{pmatrix} \frac{1}{E_x} & \frac{-\upsilon_{yx}}{E_y} & \frac{-\upsilon_{zx}}{E_z} & 0 & 0 & \frac{\eta_{x,xy}}{G_{xy}} \\ & \frac{1}{E_y} & \frac{-\upsilon_{zy}}{E_z} & 0 & 0 & \frac{\eta_{y,xy}}{G_{xy}} \\ & & \frac{1}{E_z} & 0 & 0 & \frac{\eta_{z,xy}}{G_{xy}} \\ & & & \frac{1}{G_{yz}} & \frac{\mu_{yz,xz}}{G_{xz}} & 0 \\ & & & & \frac{1}{G_{xz}} & 0 \\ & & & & & \frac{1}{G_{xy}} \end{pmatrix} \begin{pmatrix} \sigma_{xx} \\ \sigma_{yy} \\ \sigma_{zz} \\ \tau_{yz} \\ \tau_{zx} \\ \tau_{xy} \end{pmatrix} \tag{2.46}$$

Three Orthogonal Planes of Elastic Symmetry if three orthogonal planes of elastic symmetry exist in the medium and they are perpendicular to x, y, or z, the following conditions apply other than Eq. 2.45

$$a_{16} = a_{26} = a_{36} = a_{45} = 0 \tag{2.47}$$

Then, Eq. 2.46 can be further reduced to 9 independent components (Note that the matrix is symmetrical about the diagonal)

$$\begin{pmatrix}\varepsilon_{xx}\\ \varepsilon_{yy}\\ \varepsilon_{zz}\\ \gamma_{yz}\\ \gamma_{zx}\\ \gamma_{xy}\end{pmatrix}=\begin{pmatrix}\frac{1}{E_x} & \frac{-\upsilon_{yx}}{E_y} & \frac{-\upsilon_{zx}}{E_z} & 0 & 0 & 0\\ & \frac{1}{E_y} & \frac{-\upsilon_{zy}}{E_z} & 0 & 0 & 0\\ & & \frac{1}{E_z} & 0 & 0 & 0\\ & & & \frac{1}{G_{yz}} & \frac{\mu_{yz,xz}}{G_{xz}} & 0\\ & & & & \frac{1}{G_{xz}} & 0\\ & & & & & \frac{1}{G_{xy}}\end{pmatrix}\begin{pmatrix}\sigma_{xx}\\ \sigma_{yy}\\ \sigma_{zz}\\ \tau_{yz}\\ \tau_{zx}\\ \tau_{xy}\end{pmatrix} \tag{2.48}$$

One Axis of Elastic Symmetry of Rotation If the axis of elastic symmetry exists in a material, all the planes perpendicular to this axis show isotropic properties. This property is also called transversely isotropic, and will be further discussed later. For instance, if the axis coincides with *z*-axis, all the planes parallel to the *x*-*y* plane are isotropic, and this is the vertical transversely isotropic case (VTI). The number of elastic constants is now reduced to 5, and they are

$$\begin{gathered}E_h = E_x = E_y \qquad E_v = E_z\\ \upsilon_h = \upsilon_{xy} = \upsilon_{yx} \qquad \nu_v = \upsilon_{zx} = \upsilon_{zy}\\ G_v = G_{yz} = G_{xz} \qquad \mathrm{G}_h = \frac{E}{2(1+\nu)}\end{gathered} \tag{2.49}$$

Hence, the constitutive relationship becomes

$$\begin{pmatrix}\varepsilon_{xx}\\ \varepsilon_{yy}\\ \varepsilon_{zz}\\ \gamma_{yz}\\ \gamma_{zx}\\ \gamma_{xy}\end{pmatrix}=\begin{pmatrix}\frac{1}{E_h} & \frac{-\upsilon_h}{E_h} & \frac{-\upsilon_v}{E_v} & 0 & 0 & 0\\ & \frac{1}{E_h} & \frac{-\upsilon_v}{E_v} & 0 & 0 & 0\\ & & \frac{1}{E_v} & 0 & 0 & 0\\ & & & \frac{1}{G_v} & 0 & 0\\ & & & & \frac{1}{G_v} & 0\\ & & & & & \frac{1}{G_h}\end{pmatrix}\begin{pmatrix}\sigma_{xx}\\ \sigma_{yy}\\ \sigma_{zz}\\ \tau_{yz}\\ \tau_{zx}\\ \tau_{xy}\end{pmatrix} \tag{2.50}$$

Complete Symmetry This property is also called isotropic, and the number of elastic constants is reduced to only 2: *E* and *v*

$$E = E_x = E_y = E_z$$

$$\nu = \nu_{yx} = \nu_{zx} = \nu_{zy} \tag{2.51}$$

$$\mathrm{G} = \frac{E}{2(1+\nu)}$$

To satisfy the positive strain energy requirement, these two parameters should be in the following ranges (*Ong*, 1994)

$$E > 0 \qquad -1 \leq \nu \leq 0.5 \tag{2.52}$$

2.3.5.3 Elastic Properties of Shale and the Degree of Anisotropy

The presence of fine-scale lamination feature in shales, which is mainly due to the preferred depositional orientation of clay minerals in the matrix, leads to a series of directionally dependent rock properties, such as acoustic velocity, permeability and elastic modulus (*Waters et al.*, 2011). The important factors that can influence shale anisotropy include kerogen content, fluid interaction, porosity and stress-induced cracks (*Vernik and Nur*, 1992; *Vernik and Liu*, 1997). And shale anisotropy, which is expected to be transversely isotropic, should be considered regarding hydraulic fracture propagation prediction, analysis of borehole stability and stress assessment (*Waters et al.*, 2011).

For all those geomechanical applications, Young's modulus and Poisson's ratio are essential inputs showing some patterns resulted from anisotropy. To explain this, we exclusively consider a shale medium in a right-handed coordinate system with x_3-axis as the symmetry axis (Figure 2.10). In such a medium, the corresponding elastic stiffness contains five independent stiffness moduli in the following matrix form (*Amadei*, 1983; *Melendez and Schmitt*, 2013)

$$\begin{pmatrix} \sigma_{xx} \\ \sigma_{yy} \\ \sigma_{zz} \\ \tau_{yz} \\ \tau_{zx} \\ \tau_{xy} \end{pmatrix} = \begin{pmatrix} C_{11} & (C_{11}-2C_{66}) & C_{13} & & & \\ & C_{11} & C_{13} & & & \\ & & C_{33} & & & \\ & & & C_{44} & & \\ & & & & C_{44} & \\ & & & & & C_{66} \end{pmatrix} \begin{pmatrix} \varepsilon_{xx} \\ \varepsilon_{yy} \\ \varepsilon_{zz} \\ \gamma_{yz} \\ \gamma_{zx} \\ \gamma_{xy} \end{pmatrix} \tag{2.53}$$

And the Young's moduli and Poisson's ratio is given by (*Banik and Egan*, 2012)

$$E_3 = C_{33} - \frac{2C_{13}^2}{C_{11}+C_{12}} \tag{2.54}$$

$$E_1 = C_{11} + \frac{C_{13}^2(C_{12}-C_{11})+C_{12}(C_{13}^2-C_{12}C_{33})}{C_{33}C_{11}-C_{13}^2} \tag{2.55}$$

$$\nu_{31} = \nu_{32} = \frac{C_{13}}{C_{11}+C_{12}} \tag{2.56}$$

$$\nu_{13} = \nu_{23} = \frac{C_{13}(C_{11}-C_{12})}{C_{33}C_{11}-C_{13}^2} \tag{2.57}$$

$$\nu_{12} = \nu_{21} = \frac{C_{12}C_{33}-C_{13}^2}{C_{33}C_{11}-C_{13}^2} \tag{2.58}$$

Based on *Sayers* (2013) and *Sone and Zoback* (2013), the following empirical relationships exist

$$E_1 > E_3 \qquad \nu_{31} > \nu_{12} \qquad \nu_{13} > \nu_{31} \tag{2.59}$$

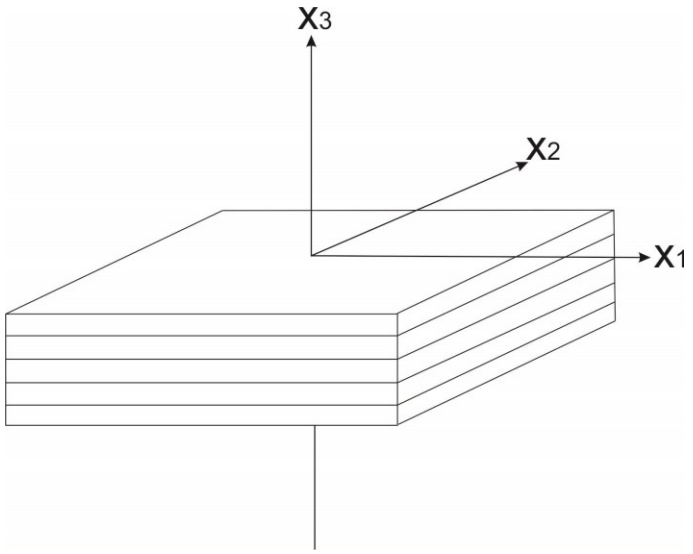

Figure 2.10 Illustration of the anisotropic symmetry of a vertical transversely isotropic shale medium located in a right-handed coordinate system. X_3 axis is the symmetry line.

Acoustic wave velocity anisotropy measurements can help us achieve elastic stiffness of anisotropic shale samples, and this have been conducted by many researchers (*Cholach and Schmitt*, 2006; *Dewhurst and Siggins*, 2006; *Johnston and Christensen*, 1995; *Melendez and Schmitt*, 2011; *Melendez and Schmitt*, 2013; *Sarout and Gueguen*, 2008; *Vernik and Nur*, 1992; *Vernik and Liu*, 1997; *Wong et al.*, 2008). Moreover, *Walsh et al.* (2008) pointed out that four out of five stiffness moduli (except C_{13}) can in principle be estimated by the dipole and the

monopole Stoneley wave measurements. To quantify the degree of anisotropy, the elastic anisotropy can be described in terms of the Thomsen's anisotropic parameters Ɛ, γ and δ (*Thomsen*, 1986), which are

$$\varepsilon = \frac{C_{11}-C_{33}}{2C_{33}} \tag{2.60}$$

$$\gamma = \frac{C_{66}-C_{55}}{2C_{55}} \tag{2.61}$$

$$\delta = \frac{(C_{13}-C_{55})^2-(C_{33}-C_{55})^2}{2C_{33}(C_{33}-C_{55})} \tag{2.62}$$

Those parameters are non-dimensional and decreases with decreasing anisotropy. For materials with 'weak anisotropy', Thomsen parameters should be $\ll 1$ (*Thomsen*, 1986).

2.4 Rock Failure

2.4.1 Introduction

The purpose of this section is to review the principles of rock failure in both compression and tension, and those principles are foundations for understanding borehole failures addressed in the following chapters. Rock strength is the maximum stress that a rock can support before it fails. Failure can lead to a change in its internal structure permanently or even complete failure by fracture. Rock failure enables us to estimate the rock strength directly and is the building block for studying the failure mechanisms of borehole instability. Therefore, we could have a better insight of rock behaviors in the process of drilling, production and completion to prevent borehole failures.

In this section, rocks are assumed to be homogeneous and isotropic. Anisotropic rocks are discussed in Chapter 4 to investigate the impacts of anisotropy on borehole stresses. Rock failure is a complex process and phenomenon which still needs more research work in the future. But this section only considers the simplified models. In the first part, the subject addressed is the rock strength in compression and the Mohr-Coulomb failure criterion. For the second part, the topic focuses on tensile failures.

Before entering the next section discussing about rock failure, it is necessary to start with rock strength measurements and introducing some basic concepts to understand the complexity of

rock behavior. According to the American Society for Testing and Materials (ASTM) standards, a desirable test specimen shall have a thickness-to-diameter ratio between 2:1 to 2.5:1 (*ASTM International*, 2010). During the test, the specimen shall be placed in the test chamber which consistently provides homogeneous confining compression, σ_3, to the whole specimen. While the upper and lower platens apply gradually increased axial compression, σ_1, to the both ends of the specimen until it fails (Fig. 2.11a). If the confining stress is zero, a uniaxial compressive test is conducted and the strength measured is unconfined compressive strength (UCS); otherwise, the test is called triaxial compression test.

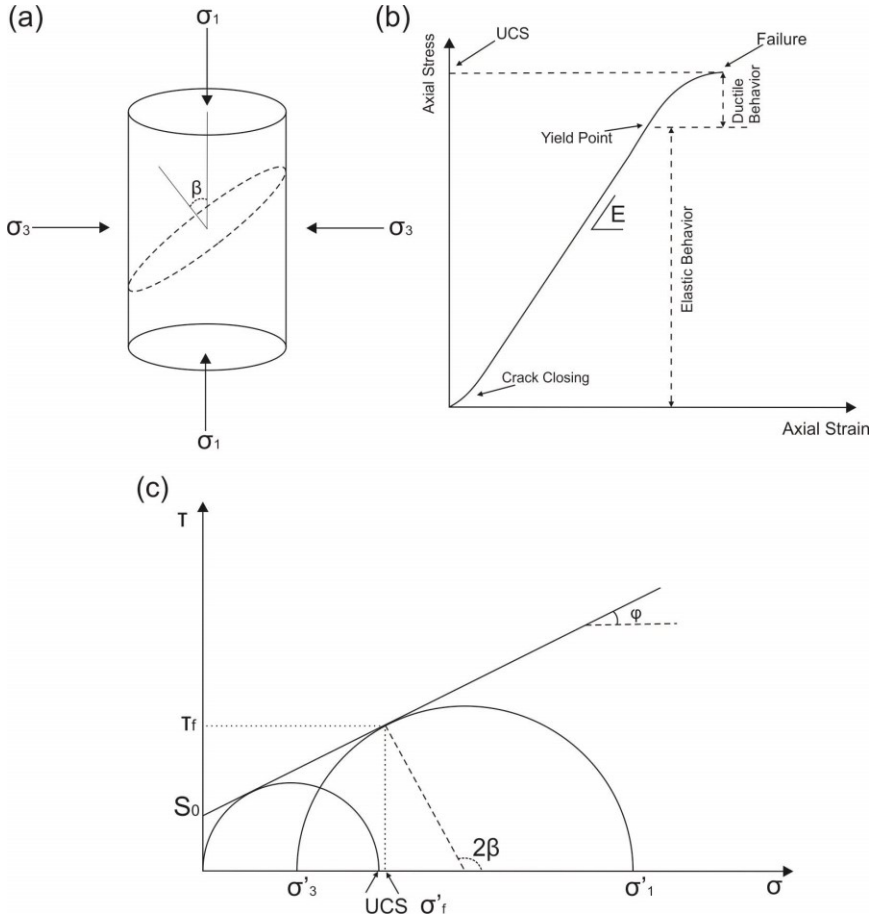

Figure 2.11 (a) A rock core fails under the triaxial compression test forming a fracture plane (dashed line). σ_3 is the confined pressure and σ_1 is the gradually increased axial pressure. β is the angle of core axis with respect to the direction that is normal to the fracture. (b) Typical laboratory stress-strain data for an intact sandstone in a uniaxial compressive test. (c) The linearized form of the Mohr-Coulomb failure envelope.

Now we focus our attention on the rock behavior of a cylindrical specimen in a uniaxial compressive test. Fig. 2.11b illustrates a typical failure behavior for a well-cemented rock in a uniaxial test. At the beginning of the process, the stress-strain data does not form a straight line due to crack closing. Then the specimen behaves elastically with a reversible deformation until the yield stress is reached. In the elastic region, the slope of the stress-strain curve is supposed to be the static Young's Moduli, *E*. At the yield point, the specimen starts to exhibits inelastic behavior or ductile behavior with the ability to withstand stress, but the damage to the rock is permanent. When the axial load is sufficiently large (~UCS), the specimen starts to fall apart losing the ability to support load quickly.

2.4.2 Compressive Failure

When the stresses applied to rock exceed the compressive strength, the rock can fail in compression. The failure process involves all the stresses; therefore, the compressive strength of rock depends on its confining stress, and the pore pressure. All study results agree that the sample strength increases with the effective confining pressure (*Zoback*, 2007). In order to take all these stresses into consideration, the most frequently used criterion is the Mohr-Coulomb criterion.

Assuming there is a failure plane existing in a rock core after the triaxial compression strength test, the effective principal stresses acting on the core are σ_1' and σ_3' ($\sigma_1' > \sigma_3'$), and β is the angle between the direction normal to the fracture surface and σ_1' (Fig. 2.11a). At the moment of failure, the shear stress, τ_f, and the effective normal stress, σ_f', acting on the failure surface is

$$\tau_f = 0.5(\sigma_1' - \sigma_3')sin2\beta \tag{2.63}$$

$$\sigma_f' = 0.5(\sigma_1' + \sigma_3') + 0.5(\sigma_1' - \sigma_3')cos2\beta \tag{2.64}$$

The failure of a rock during the triaxial compression test can be represented by a Mohr circle in the τ-σ' space (Fig. 2.11c). The radius of the Mohr circle increases with the difference between σ_1' and σ_3'. Failure occurs when the circle 'touches' the Mohr-Coulomb failure envelope, and the point of intersection corresponds to the stresses acting on the failure plane at the moment of failure. The empirical Mohr failure envelope can be determined by a series of triaxial tests with different confining pressures. Unlike the one shown in Fig. 2.11b, the envelope is not a straight

line in the real case, and flattens as confining pressure increases. However, most rock failures can be considered in terms of the linearized Mohr failure envelop, which can be expressed in the following mathematical form

$$|\tau| = S_0 + \mu\sigma' \tag{2.65}$$

where the slope, μ, is the coefficient of internal friction describing the resistance of a rock to compressional failures ($\mu = tan\varphi$), and S_0 is cohesion, which is not possible to be measured directly, but is feasible to be calculated based on its relationship with the unconfined compressive strength (UCS or C_0)

$$C_0 = 2S_0[(\mu_i^2 + 1)^{0.5} + \mu_i] \tag{2.66}$$

Fig. 2.11c also shows the angle, 2β, giving the line connecting the center of the circle and the point where the circle touches the envelope. Note that based on the geometry, the relationship between β and φ is

$$\beta = \frac{\pi}{4} + \frac{\varphi}{2} \tag{2.67}$$

The linearized form of the Mohr-Coulomb failure criteria is given as

$$\sigma_1 = C_0 + q\sigma_3 \tag{2.68}$$

And

$$q = [(\mu_i^2 + 1)^{0.5} + \mu_i]^2 = \tan^2\left(\frac{\pi}{4} + \frac{\varphi}{2}\right) = \tan^2\beta \tag{2.69}$$

Even though the Mohr-Coulomb is the most dominant method in determining rock compressive failure, it does not account for the influence of the intermediate stress; and the other criterion with the similar case is the empirical Hoek-Brown criterion (*Hoek and Brown*, 1980). According to *Zoback* (2007), those two approaches are suitable for the triaxial test with a uniform confining pressure ($\sigma_1 > \sigma_2 = \sigma_3$); whereas, in terms of polyaxial criteria ($\sigma_1 > \sigma_2 > \sigma_3$), other failure criteria considering the effects of σ_2 are more desirable to be adopted, and they are the modified Lade criterion (*Ewy*, 1999), the modified Wiebols-Cook criterion (*Wiebols and Cook*, 1968; *Zhou*, 1994), the Drucker-Prager criterion (*Drucker and Prager*, 1952), and the Mogi-Coulomb approach (*Al-Ajmi and Zimmerman*, 2006).

2.4.3 Tensile Failure

Tensile failure occurs when the effective tensile stress exceeds the tensile strength (T_0) of the rock sample. For isotropic rocks, the tensile failure criterion is given as

$$\sigma_3' = -T_0 \tag{2.70}$$

Compared to the compressional strength of rock, the tensile strength is less important due to the following reasons: (1) rock tensile strength is quite low especially when cracks pre-exist in the rock, and in this study, it is considered to be zero; (2) it is extremely rare in nature to have tensile *in situ* stress at depth (*Jaeger et al.*, 2007; *Zoback*, 2007). The tensile fracture plane usually initiated from pre-existing flaws with its orientation approximately normal to the direction of the minimum principal stress.

Even though the tensile failure is rare in nature because the rock at depth in the Earth is almost always in compression, it can occur in the vicinity of boreholes as the virgin stress state was disturbed during and after the drilling process (Chapter 3). Moreover, the S_h magnitude measurements discussed in section 2.1.2 (e.g., mini-frac tests, leak-off tests) are processes forming tensile fractures when fluid pressure becomes higher than the minimum principal stress. Hydraulic fracturing is also a form of tensile failure that utilizes the opening of tensile fractures in order to enhance the formation permeability.

2.5 Summary

In this chapter, we mainly reviewed the following content

- Some basic principles of Earth crustal stress state including its mathematical form, transformation among different coordinates, classifications based on their relative magnitudes;
- Estimation methods for crustal stresses with emphasis on presenting the concepts of fracking.
- Rock elasticity: mathematical terminologies, their relationships with elastic wave velocities, poroelasiticity effects and the four classical types of rock intrinsic anisotropy;
- Rock failure mechanisms on compressive failures and tensile failures.

2.6 References

Addis, M. A., T. H. Hanssen, N. Yassir, D. R. Willoughby, and J. Enever (1998), A Comparison Of Leak-Off Test And Extended Leak-Off Test Data For Stress Estimation, Society of Petroleum Engineers, SPE/ISRM 47235, Trondheim, Norway, 8-10 July.

Al-Ajmi, A. M., and R. W. Zimmerman (2006), Stability analysis of vertical boreholes using the Mogi–Coulomb failure criterion, *International Journal of Rock Mechanics and Mining Sciences*, *43*(8), 1200-1211.

Amadei, B. (1983), *Rock anisotrpy and the theory of stress measurements*, Springer-Verlag, Berlin.

Anderson, E. M. (1951), *The dynamics of faulting and dyke formation with applications to Britain*, 2nd ed., Oliver and Boyd, London and Edinburgh.

ASTM International D7012-10 (2010), Standard test method for compressive strength and elastic moduli of intact rock core speciments under varying states of stress and temperatures, ASTM International, West Conshohocken, Pennsylvania.

Bachu, S., K. Haug, and K. Micheal (2008), Stress regime at acid-gas injection operations in western canada, *Energy Resources Conservation Board Special Report 094*, 42 pp, Edmonton, Canada.

Banik, N. C., and M. S. Egan (2012), Effects of VTI anisotropy on shale reservoir characterization, SPE Middle East Unconventional Gas Conference and Exhibition, Society of Petroleum Engineers, Abu Dhabi, UAE, 23-25 Janurary.

Barber, J. R. (2010), *Elasticity*, 3rd rev. ed., Springer Verlag, Dordrecht; New York.

Barla, G. (1974), Rock anisotropy - Theory and laboratory testing. Rock mechanics, Muller, L. (Editor), (Course held at the Department of Mechanics of Solids, Udine, Italy), pp. 131-169.

Bell, J. S. (2006), In-situ stress and coal bed methane potential in Western Canada, *B Can Petrol Geol*, *54*(3), 197-220.

Bell, J. S., and D. I. Gough (1979), Northeast-southwest compressive stress in Alberta - evidence from oil-wells, *Earth and Planetary Science Letters*, *45*(2), 475-482.

Bell, J. S., and S. Bachu (2003), In situ stress magnitude and orientation estimates for Cretaceous coal-bearing strata beneath the plains area of central and southern Alberta, *B Can Petrol Geol*, *51*(1), 1-28.

Bell, J. S., and S. Bachu (2004), In-Situ stress magnitudes in the Alberta Basin-regional coverage for petroleum engineers, Canadian International Petroleum Conference, Petroleum Society of Canada, PETSOC-2004-155, Calgary, Alberta, 8-10 June.

Bell, J. S., P. R. Price, and P. J. McLellan (1994), In-situ stress in the Western Canada Sedimentary Basin, in *Geological Atlas of Western Canada Sedimentary Basin, G. Mossop and I. Shetsen (comps.)*, edited, Canadian Society of Petroleum Geologists and Alberta Research Council, p. 439-446.

Carcione, J. M., H. B. Helle, N. H. Pham, and T. Toverud (2003), Pore pressure estimation in reservoir rocks from seismic reflection data, *Geophysics*, *68*(5), 1569-1579.

Cholach, P. Y., and D. R. Schmitt (2006), Intrinsic elasticity of a textured transversely isotropic muscovite aggregate: Comparisons to the seismic anisotropy of schists and shales, *Journal of Geophysical Research: Solid Earth*, *111*(B9), B09410.

Dewhurst, D. N., and A. F. Siggins (2006), Impact of fabric, microcracks and stress field on shale anisotropy, *Geophys J Int*, *165*(1), 135-148.

Drucker, D. C., and W. Prager (1952), Soil mechanics and plastic analysis or limit design, *Quarterly of Applied Mathematics*, *10*(2), 157-165.

Eaton, B. A. (1975), The equation for geopressure prediction from well logs, Society of Petroleum Engineers, SPE-5544-MS, Dallas, Texas, 28 September-1 October.

Ewy, R. T. (1999), Wellbore-stability predictions by use of a modified Lade criterion, *SPE Drilling & Completion*, *14*(2), 85-91.

Fjaer, E., R. M. Holt, P. Horsrud, A. M. Raaen, and R. Risnes (2008), *Petroleum related rock mechanics*, Elsevier, Amsterdam, the Netherlands.

Gaarenstroom, L., R. A. J. Tromp, M. C. Dejong, and A. M. Brandenburg (1993), Overpressures in the central North-Sea implications for trap integrity and drilling safety, Petroleum Geology of Northwest Europe: Proceedings of the 4th Conference, v. 4.

Gassmann, F. (1951), Über die elastizität poröser medien, *Viertel. Naturforsch. Ges. Zürich*, *96*, 1-23.

Grasby, S. E., D. M. Allen, S. Bell, Z. Chen, G. Ferguson, A. Jessop, M. Kelman, M. Ko, J. Majorowicz, M. Moore, J. Raymond, and R. Therrien (2012), Geothermal energy resource potential of Canada, Geological Survey of Canada, Open File 6914, 322p, doi: 10.4095/291488.

Haimson, B., and C. Fairhurst (1969), In-situ stress determination at great depth by means of hydraulic fracturing, American Rock Mechanics Association, ARMA-69-0559, Berkeley, California, 16-19 June.

Hawkes, C. D., S. Bachu, K. Haug, and A. W. Thompson (2005), Analysis of in-situ stress regime in the Alberta Basin, Canada, for performance assessment of CO_2 geological sequestration sites, Fourth Annual Conference on Carbon Capture and Sequestration, DOE/NETL, May 2–5.

Hill, R. (1952), The elastic behaviour of a crystalline aggregate, *Proceedings of The Physical Society. Section A*, *65*(5), 349-354.

Hoek, E., and E. T. Brown (1980), Empirical strength criterion for rock masses, *Journal of the Geotechnical Engineering Division-Asce*, *106*(9), 1013-1035.

Jaeger, J. C., N. G. W. Cook, and R. W. Zimmerman (2007), *Fundamentals of rock mechanics*, 4th ed., Blackwell Pub, Malden, MA.

Johnston, J. E., and N. I. Christensen (1995), Seismic anisotropy of shales, *Journal of Geophysical Research: Solid Earth*, *100*(B4), 5991-6003.

Lekhnitskii, S. G. (1981), *Theory of elasticity of an anisotropic body*, Mir Publications, Moscow.

Mavko, G., T. Mukerji, and J. Dvorkin (2009), *The rock physics handbook [electronic resource] : tools for seismic analysis of porous media / Gary Mavko, Tapan Mukerji, Jack Dvorkin*, 2nd ed., Cambridge University Press, Cambridge; New York.

McLellan, P. J. (1987), In-stu stress prediction and measurement by hydraulic fracturing, Wapiti, Alberta, Petroleum Society of Canada, PETSOC-87-38-58, Calgary, Alberta, June 7-10.

Melendez, J., and D. R. Schmitt (2011), Investigating anisotropy in rocks by using pulse transmission method, *CSEG Recorder*, *36*(10), 38-42.

Melendez, J., and D. R. Schmitt (2013), Anisotropic elastic moduli of carbonates and evaporites from the Weyburn-Midale reservoir and seal rocks, *Geophys Prospect*, *61*(2), 363-379.

Nur, A., and J. D. Byerlee (1971), An exact effective stress law for elastic deformation of rock with fluids, *Journal of Geophysical Research*, *76*(26), 6414-6419.

Ong (1994), Borehole stability, 344 pp, U. of Oklahoma, Norman, Oklahoma.

Raaen, A. M., P. Horsrud, H. Kjørholt, and D. Økland (2006), Improved routine estimation of the minimum horizontal stress component from extended leak-off tests, *International Journal of Rock Mechanics and Mining Sciences*, *43*(1), 37-48.

Reis, Á. F. C., F. H. R. Bezerra, J. M. Ferreira, A. F. do Nascimento, and C. C. Lima (2013), Stress magnitude and orientation in the Potiguar Basin, Brazil: Implications on faulting style and reactivation, *Journal of Geophysical Research: Solid Earth*, *118*(10), 2012JB009953.

Reiter, K., O. Heidbach, D. Schmitt, K. Haug, M. Ziegler, and I. Moeck (2014), A revised crustal stress orientation database for Canada, *Tectonophysics*, *636*(0), 111-124.

Sarout, J., and Y. Gueguen (2008), Anisotropy of elastic wave velocities in deformed shales: Part 2-Modeling results, *Geophysics*, *73*(5), D91-D103.

Sayers, C. M. (2013), The effect of anisotropy on the Young's moduli and Poisson's ratios of shales, *Geophys Prospect*, *61*(2), 416-426.

Sayers, C. M., G. M. Johnson, and G. Denyer (2002), Predrill pore-pressure prediction using seismic data, *Geophysics*, *67*(4), 1286-1292.

Schmitt, D. (2014), Seimic properties (in press), in *Treatise on Geophysics, 2 edition*, edited by G. Schubert, p. 44.

Schmitt, D., C. Currie, and L. Zhang (2012), Crustal stress determination from boreholes and rock cores: Fundamental principles, *Tectonophysics*, *580*, 1-26.

Schön, J. (2011), *Physical properties of rocks*, Oxford : Elsevier, 2011.

Sone, H., and M. D. Zoback (2013), Mechanical properties of shale-gas reservoir rocks - Part 1: Static and dynamic elastic properties and anisotropy, *Geophysics*, *78*(5), D378-D389.

Teichrob, R., A. Kustamsi, G. Hareland, and U. Odiegwu (2010), Estimating In Situ Stress Magnitudes And Orientations In an Albertan Field In Western Canada, 44th U.S. Rock Mechanics Symposium and 5th U.S.-Canada Rock Mechanics Symposium, ARMA-10-224, Salt Lake City, Utah, 27-30 June.

Thomsen, L. (1986), Weak elastic anisotropy, *Geophysics*, *51*(10), 1954-1966.

Timoshenko, S., and J. N. Goodier (1970), *Theory of elasticity [by] S. P. Timoshenko [and] J. N. Goodier*, 3rd ed., McGraw-Hill, New York.

Vernik, L., and A. Nur (1992), Ultrasonic Velocity and Anisotropy of Hydrocarbon Source Rocks, *Geophysics*, *57*(5), 727-735.

Vernik, L., and X. Z. Liu (1997), Velocity anisotropy in shales: A petrophysical study, *Geophysics*, *62*(2), 521-532.

Walsh, J. J., B. K. Sinha, T. J. Plona, D. E. Miller, and M. Ammerman (2008), Derivation of anisotropy parameters in a shale using borehole sonic data, SEG Technical Program Expanded Abstracts, American Rock Mechanics Association, 26, 1.

Waters, G. A., R. E. Lewis, and D. Bentley (2011), The effect of mechanical properties anisotropy in the generation of hydraulic fractures in organic shales, SPE Annual Technical Conference and Exhibition, Society of Petroleum Engineers, Denver, Colorado, USA, 30 October-2 November.

Wiebols, G. A., and N. G. W. Cook (1968), An energy criterion for the strength of rock in polyaxial compression, *Int J Rock Mech Min*, *5*(6), 529-549.

Wong, R. C. K., D. R. Schmitt, D. Collis, and R. Gautam (2008), Inherent transversely isotropic elastic parameters of over-consolidated shale measured by ultrasonic waves and their comparison with static and acoustic in situ log measurements, *Journal of Geophysics and Engineering*, *5*(1), 103-117.

Zhou, S. (1994), A program to model the initial shape and extent of borehole breakout, *Computers & Geosciences*, *20*(7–8), 1143-1160.

Zimmerman, R. W. (1991), *Compressibility of sandstones*, Elsevier ; New York, NY, USA: Distributors for the United States and Canada, Elsevier Science Pub. Co., Amsterdam ; New York.

Zoback, M. D. (2007), *Reservoir geomechanics*, Cambridge University Press, Cambridge.

Chapter 3

Borehole Stresses and Mechanical Behaviors of Borehole Fracture

3.1 Overview

The *in-situ* stress state is always in compression as a result of the overburden and tectonic effects (Chapter 2). After the drilling process, original solid materials which used to carries the load generated from far-field stresses are now replaced by a borehole. For an open hole, since only the fluid pressure can support the borehole, the stress concentration will redistribute and strongly vary with the azimuth of the wall and the distance from the wall (*Fjaer et al.*, 2008; *Zoback*, 2007). If the deviatoric stress exceeds the formation strength, wellbore failure in either tension or compression may occur during drilling. Therefore, knowledge of stresses around the borehole is essential in order to understand the manner in which the formation in the borehole vicinity responds to the stress redistribution.

The occurrence of wellbore failure observed in image logs *in-situ* is important information that allows one to refer the stress states and, in some cases, the rock strength. Wellbore failure mainly includes compressive failures known as breakouts (*Bell and Gough*, 1982) and tensile failures also called drilling-induced tensile fractures (DITF) (*Aadnoy*, 1990). The existence of breakouts is quite common due to high compressive stresses and low mud weights. An appropriate amount of breakouts will not create any risk for the wellbore; however, sufficiently wide breakouts or even washouts can lead to borehole instability problems, such bridges, stuck pipes, and tight spots. On the other hand, drilling-induced tensile fractures (DITFs) can be initiated by high mud weight and temperature effect (cooling) (*Zoback*, 2007). Excessively high mud weight can create hydraulic fractures accidentally causing incidents like lost circulations. Therefore, to avoid borehole instability, knowledge of the borehole failure mechanism is crucial, and these will be discussed in this chapter. Then, based on the program developed by *Peska and Zoback* (1995), the tendencies of failure initiation for an arbitrarily orientated borehole will also be addressed.

Additionally, to investigate the mechanical behavior of DITFs, a series of photoelasticty tests were carried out on clear glass blocks containing borehole aligned both with and at an angle with

respect to the principal stresses. The samples were illuminated with polarized light such that birefringent fringes could be video recorded during the measurements; this was useful in assessing states of stress and in determining fracture initiation. Axial drilling-induced tensile fractures were observed at the azimuths of the applied uniaxial stress as would be expected from the concentrated stresses. *En echelon* fractures were observed from the borehole deviated at 45° to the direction of the compression. These preliminary and currently qualitative results show that glass blocks serve as a useful test medium for studies of stress concentration and drilling induced fracture creation. This part of the thesis is developed from a submitted conference paper (*Jia and Schmitt*, 2014).

3.2 Stresses around a Borehole in an Isotropic Homogeneous Formation

The manner in which a vertical wellbore cavity disturbs the original stress state in the isotropic formation was first studied by *Kirsch* (1898) who examined the general 2-D plane strain problem of stress distributions around a circular cavity. This solution was then improved upon by *Hiramatsu and Oka* (1962) into a 3-D case of an arbitrarily oriented cylindrical cavity through an isotropic medium by changing coordinate systems to consider the nonalignment between the borehole and the *in-situ* stress. This section first introduces the mathematical method for stress transformation followed by a review of the general solution for borehole stress distribution in the isotropic formation. Some illustrations of the stress states are developed using a MATLAB™ based program coded to visualize the near-wellbore stress concentration in a 2-D plane perpendicularly intersecting the borehole in an isotropic continuum.

Before introducing the transformation formulas, several assumptions are made

- The formation is homogeneous, isotropic, continuous and elastic;
- The *in-situ* stress state consists of three principal stresses: the vertical stress, S_v, the maximum and minimum horizontal stresses, S_H and S_h, as introduced in Chapter 2;
- Poroelasticity, chemical and temperature effects are neglected;

- The wellbore is assumed to be infinitely long and subjected to identical forces normal to the borehole wall, so the solution can be simplified by the plane strain formulation (*Amadei*, 1983).

For the classical plane strain formulation, out-of-plane displacements, w, must vanish (*Amadei*, 1983); hence,

$$\epsilon_z = \gamma_{xz} = \gamma_{yz} = 0 \tag{3.1}$$

While the remaining three strain components ϵ_x, ϵ_y and γ_{xy} in the strain matrix are non-zero. This assumption cannot be utilized in the anisotropic formation as will be further discussed in Chapter 4.

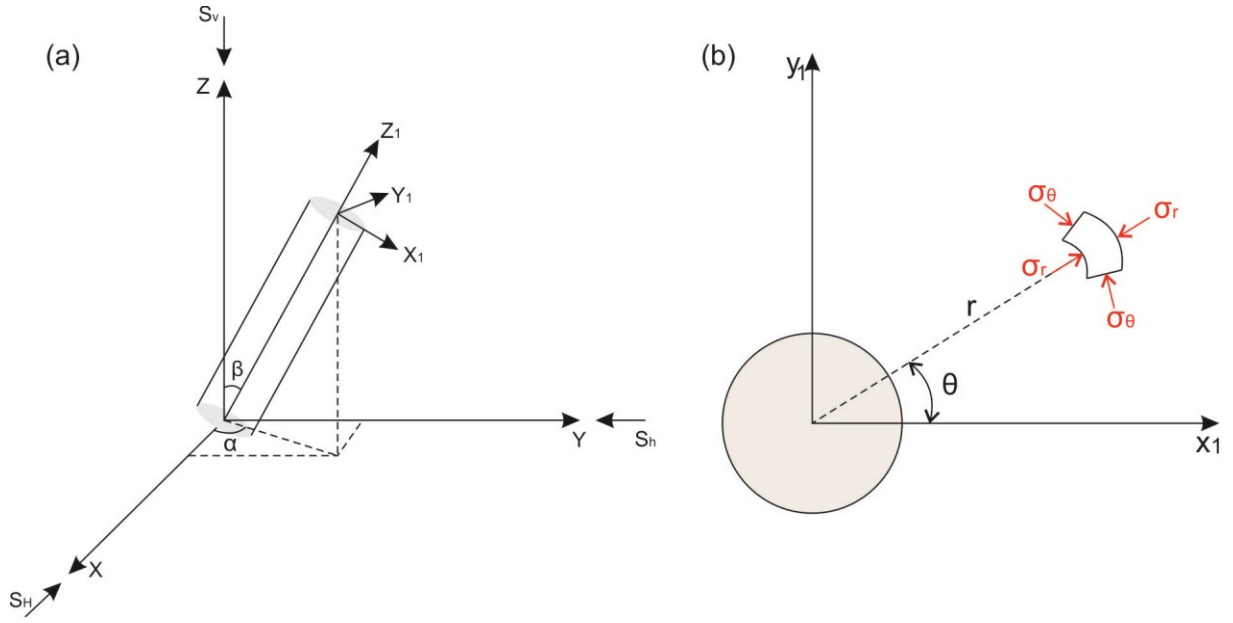

Figure 3.1 (a) Coordinate systems for the borehole stress model. The axes of the Cartesian coordinate system, X-Y-Z are all aligned with one of the *in-situ* stresses; whereas, the coordinate system X_1-Y_1-Z_1 are directly associated with the borehole. (b) Stresses (in red) are transferred in the cylindrical coordinate system in a plain plane view, and they are hoop stress and radial stress.

Fig. 3.1a shows the two coordinate systems defined in the stress model for the isotropic case, and they are: (1) the global or *in-situ* stress coordinate system, X-Y-Z, and (2) the borehole coordinate system, X_1-Y_1-Z_1. The relative orientation of the borehole system with respect to the stress system is defined by the plunge (*i.e.*, inclination relative to vertical) β and the trend (*i.e.*, azimuth from the X axis) α. To examine the stress distribution around the borehole wall, it is

necessary to transform the *in-situ* principal stress values into those in the borehole cylindrical coordinate system. Therefore, two steps are needed:

1. Stress transformations from X-Y-Z to X_1-Y_1-Z_1 (Fig. 3.1a);
2. Stress transformations from the X_1-Y_1-Z_1 Cartesian coordinate system to the ζ-θ-ξ cylindrical coordinate system (Fig. 3.1b), where r represents the distance from the borehole axis, θ is the azimuth of the point from the x-axis and ξ is the position along the borehole axis.

The first step can be achieved by the direction cosines *l, m* and *n*

$$\begin{gathered} l_1 = \cos\beta\cos\alpha\,, \qquad l_2 = -\sin\alpha\,, \qquad l_3 = \sin\beta\cos\alpha \\ m_1 = \cos\beta\sin\alpha\,,\ m_2 = \cos\alpha\,,\ m_3 = \sin\beta\sin\alpha \\ n_1 = -\sin\beta\,, \qquad n_2 = 0, \qquad n_3 = \cos\beta \end{gathered} \tag{3.2}$$

Then, the formation stresses expressed in the X_1-Y_1-Z_1 Cartesian coordinate system become

$$\sigma_x = l_1^2 S_H + m_1^2 S_h + n_1^2 S_v \tag{3.3}$$

$$\sigma_y = l_2^2 S_H + m_2^2 S_h + n_2^2 S_v \tag{3.4}$$

$$\sigma_z = l_3^2 S_H + m_3^2 S_h + n_3^2 S_v \tag{3.5}$$

$$\tau_{xy} = l_1 l_2 S_H + m_1 m_2 S_h + n_1 n_2 S_v \tag{3.6}$$

$$\tau_{yz} = l_2 l_3 S_H + m_2 m_3 S_h + n_2 n_3 S_v \tag{3.7}$$

$$\tau_{xz} = l_1 l_3 S_H + m_1 m_3 S_h + n_1 n_3 S_v \tag{3.8}$$

The stresses at an infinitesimal point in a cylindrical coordinate are denoted σ_r, σ_θ, σ_ζ, $\tau_{\theta\zeta}$, $\tau_{r\zeta}$ and $\tau_{r\theta}$. The transformation between stresses in the cylindrical and Cartesian coordinates can be expressed in the following mathematical forms:

$$\sigma_r = \frac{1}{2}(\sigma_x + \sigma_y) + \frac{1}{2}(\sigma_x - \sigma_y)cos2\theta + \tau_{xy}sin2\theta \tag{3.9}$$

$$\sigma_\theta = \frac{1}{2}(\sigma_x + \sigma_y) - \frac{1}{2}(\sigma_x - \sigma_y)cos2\theta - \tau_{xy}sin2\theta \tag{3.10}$$

$$\sigma_{\xi} = \sigma_z \tag{3.11}$$

$$\tau_{r\theta} = \frac{1}{2}(\sigma_y - \sigma_x)sin2\theta + \tau_{xy}cos2\theta \tag{3.12}$$

$$\tau_{r\zeta} = \tau_{yz}sin\theta + \tau_{xz}cos\theta \tag{3.13}$$

$$\tau_{\theta\zeta} = \tau_{yz}cos\theta - \tau_{xz}sin\theta \tag{3.14}$$

For the boundary condition, assuming that the well radius is *a*, and the *in-situ* stresses are applied at $r = R_0$, where $R_0 \gg a$, which indicates that the borehole effects on stresses vanishes as the distance increasing. The general solutions for the near-wellbore stress distribution can be written as:

$$\sigma_r = \frac{\sigma_x+\sigma_y}{2}\left(1 - \frac{a^2}{r^2}\right) + \frac{\sigma_x-\sigma_y}{2}\left(1 - 4\frac{a^2}{r^2} + 3\frac{a^4}{r^4}\right)cos2\theta + \tau_{xy}\left(1 - 4\frac{a^2}{r^2} + 3\frac{a^4}{r^4}\right)sin2\theta + P_w\frac{a^2}{r^2} \tag{3.15}$$

$$\sigma_\theta = \frac{\sigma_x+\sigma_y}{2}\left(1 + \frac{a^2}{r^2}\right) + \frac{\sigma_x-\sigma_y}{2}\left(-1 - 3\frac{a^4}{r^4}\right)cos2\theta + \tau_{xy}\left(-1 - 3\frac{a^4}{r^4}\right)sin2\theta - P_w\frac{a^2}{r^2} \tag{3.16}$$

$$\sigma_\zeta = \sigma_z - \nu\left[2(\sigma_x - \sigma_y)\frac{a^2}{r^2}cos2\theta + 4\tau_{xy}\frac{a^2}{r^2}sin2\theta\right] \tag{3.17}$$

$$\tau_{\theta\zeta} = \tau_{yz}\left(1 + \frac{a^2}{r^2}\right)cos\theta - \tau_{xz}\left(1 + \frac{a^2}{r^2}\right)sin\theta \tag{3.18}$$

$$\tau_{r\zeta} = \tau_{yz}\left(1 - \frac{a^2}{r^2}\right)sin\theta + \tau_{xz}\left(1 - \frac{a^2}{r^2}\right)cos\theta \tag{3.19}$$

$$\tau_{r\theta} = \frac{\sigma_x-\sigma_y}{2}\left(-1 - 2\frac{a^2}{r^2} + 3\frac{a^4}{r^4}\right)sin2\theta + \tau_{xy}\left(1 + 2\frac{a^2}{r^2} - 3\frac{a^4}{r^4}\right)cos2\theta \tag{3.20}$$

where P_w is the wellbore pressure and ν is Poisson's ratio. Therefore, at the wellbore wall, the equations can be simplified to the following forms:

$$\sigma_r = P_w \tag{3.21}$$

$$\sigma_\theta = \sigma_x + \sigma_y - 2(\sigma_x - \sigma_y)cos2\theta - 4\tau_{xy}sin2\theta - P_w \tag{3.22}$$

$$\sigma_\zeta = \sigma_z - \nu\left[2(\sigma_x - \sigma_y)cos2\theta + 4\tau_{xy}sin2\theta\right] \tag{3.23}$$

$$\tau_{\theta\zeta} = 2(-\tau_{xz}sin\theta + \tau_{yz}cos\theta) \tag{3.24}$$

$$\tau_{r\zeta} = \tau_{r\theta} = 0 \tag{3.25}$$

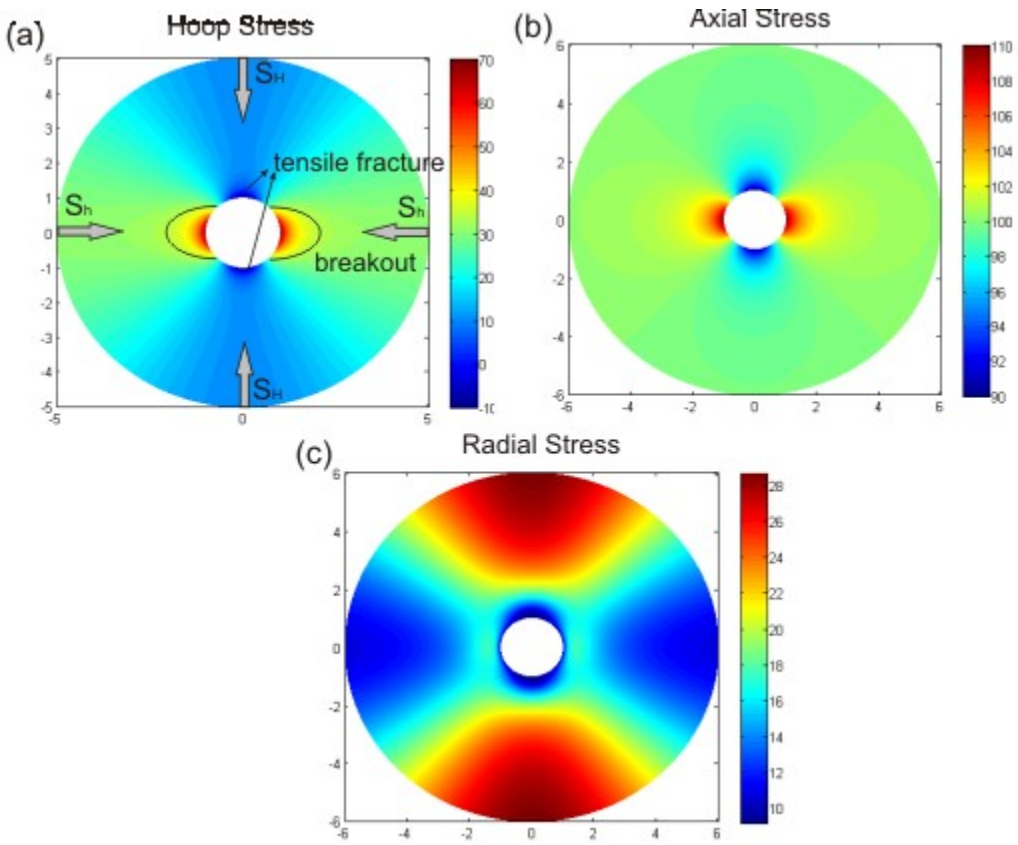

Figure 3.2 The distributions of (a) hoop stress, (b) axial stress, and (c) radial stress around a vertical wellbore in a linear elastic, isotropic and homogeneous formation. The stress orientations are indicated in grey arrows and borehole fractures are also shown in part (a). Hot colors represent more compressive stresses; whereas, cold colors represent less compressive stresses or even tensile stresses if in negative values.

Based on the analytical solutions introduced above, a MATLAB^{TM} based program was produced to visualize the stress concentration around an arbitrarily oriented borehole wall in a linear elastic, isotropic and homogeneous formation. Fig. 3.2 shows an example for a vertical borehole the axis of which coincides with the vertical principal stress. The input parameters of this example are

$S_H = 30MPa$ $S_h = 10MPa$ $S_v = 100MPa$ $P_w = 10MPa$ $\nu=0.25$

The results illustrate that in a compressional *in-situ* stress state, the hoop stress is more compressive than S_H in the direction of S_h; whereas, it is in tension at the azimuth of S_H due to the joint effects of the mud weight and the horizontal stress contrast. The dramatic stress change around the wellbore largely raises the possibility of formation failure, which yields important information regarding to the *in-situ* stress. Therefore, the failure mechanism is the key to understand the relationship between wellbore fractures and the *in-situ* stress.

3.3 Borehole Failure Mechanisms and the Corresponding Fractures

Without any preexisting fractures, borehole failures are most likely to initiate at the borehole wall where stresses are highly disturbed and concentrated. Therefore, to examine the failure mechanisms of borehole fracture, it is necessary to first calculate the principal stresses (with principal stresses, all shear stresses vanish) at a specific point on the borehole wall, which are given as (*Aadnoy*, 1990; *Aadnoy and Bell*, 1998):

$$\sigma_i = P_w \tag{3.26}$$

$$\sigma_j = \frac{1}{2}\left(\sigma_\theta + \sigma_\xi\right) + \frac{1}{2}\left[\left(\sigma_\theta - \sigma_\xi\right)^2 + 4\tau_{\theta\xi}\right]^{1/2} \tag{3.27}$$

$$\sigma_k = \frac{1}{2}\left(\sigma_\theta + \sigma_\xi\right) - \frac{1}{2}\left[\left(\sigma_\theta - \sigma_\xi\right)^2 + 4\tau_{\theta\xi}\right]^{1/2} \tag{3.28}$$

where, $\sigma_j > \sigma_k$, and σ_i acts normal to the borehole wall pointing outward. In this case, the pore pressure is neglected. After determining the relative magnitudes of these principal stresses with a given set of *in-situ* stress, they can be relabeled as σ_1, the largest principal stress, σ_2, the intermediate principal stress and σ_3, the minimum principal stress at the borehole wall.

The rock surrounding the borehole wall can be considered subject to the three principal stresses defined in Eq. 3.26 – Eq. 3.28. If the stresses exceed the rock strength, breakouts, a kind of fracture resulted from compressive failure, may first occur at the azimuth of S_h. Utilizing a compressive failure criteria (i.e., Mohr-Coulomb failure criteria), the zone of compressive failure can be determined (Fig. 3.2a), and those are the places where breakouts initiate. Various studies have been carried out to study the failure behaviors of borehole breakout using linear elastic

models (*Aadnoy and Bell*, 1998; *Al-Ajmi and Zimmerman*, 2006; *Peska and Zoback*, 1995; *Zheng et al.*, 1989). *Wang et al.* (1994) developed an analytical nonlinear elastoplastic model to estimate the yielding zone and predict borehole failure. However, the actual mechanisms of borehole breakout are still not fully understood. Breakouts can be avoided by increasing the mud weight during drilling, but they become very sensitive and more likely to occur in over-pressured formations (*i.e.*, those with pore fluid pressure in excess of that expected due to normal hydrostatic increase with depth) because a larger pore pressure shifts the Mohr circle closer to the Mohr failure envelope without changing other conditions.

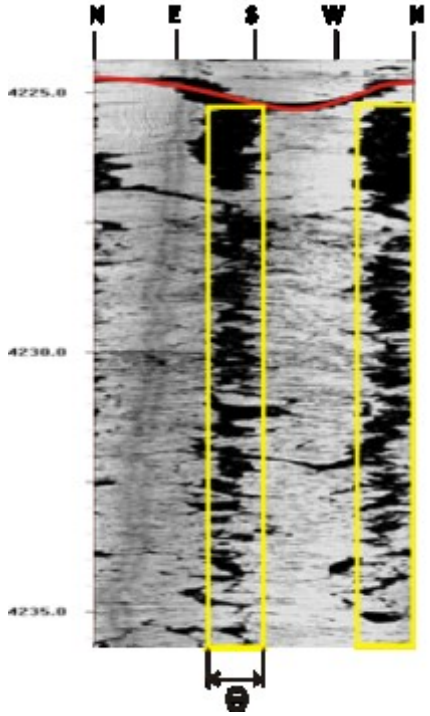

Figure 3.3 Borehole televiewer image data from southern Idaho shows a planar feature (red line) and borehole breakouts (yellow boxes). Based on a work that is done by (*Shervais et al.*, 2013).

Borehole breakouts are observed from oriented caliper logs (*e.g.*, dipmeter) and image logs. Fig. 3.3 shows an unwrapped ultrasonic borehole televiewer image collected from Southern Idaho as part of the International Continental Drilling Program Project Hotspot (*Shervais et al.*, 2013), The yellow boxes in Fig. 3.3 highlight the borehole breakouts. Note that breakouts appear in pairs on both sides of the borehole wall due to the symmetrical stress patterns as indicated in Fig. 3.2. In this example, the direction of the minimum principal stress referred from the strikes of

breakouts is in the SE-NW direction. Furthermore, the breakout width, Θ, has been used to estimate the magnitude of S_H based on the assumptions that (1) the breakout width does not change as the breakout deepens; (2) at the edge of the breakout width at the borehole wall, the compressive stress equals to the limit of rock strength (*Barton et al.*, 1988; *Schmitt et al.*, 2013).

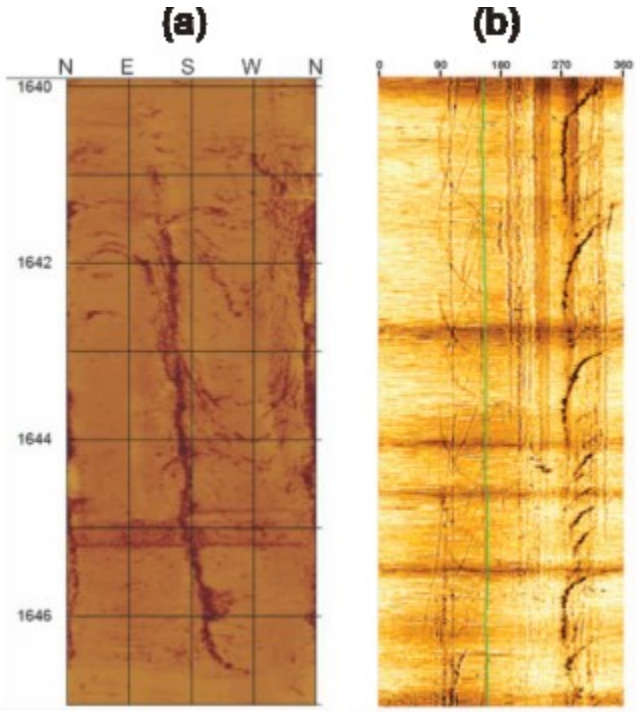

Figure 3.4 (a) Ultrasonic borehole televiewer data from the Hunt well, N. Alberta (*Chan*, 2013) displaying axial DITF. (b) *En-echelon* DITF from formation microscanner data of *Barton and Moos* (2010) used with permission under the AAPG fair use policy.

Similar to the failure mechanism discussed in the previous chapter, DITFs occur when the minimum principal stress at the borehole wall exceeds the tensile strength of surrounding formation rocks. Unlike borehole breakouts and hydraulic fractures, DITFs propagate no more than a cm from the borehole wall (*Zoback*, 2007), as such, the only reliable way to detect the existence of DITFs is by using image logs. Image logs reveal two types of DITFs: (1) fractures occur in pairs and almost parallel to the borehole axis with an offset of 180°, which are so called axial DITFs (Fig. 3.4a); (2) fractures occur in pairs with an offset of 180° but inclined with respect to the borehole axis and sometimes interconnected (Fig. 3.4b). The second type of fractures is also called *en-echelon* DITFs, and their occurrences indicate the nonalignment between the directions of the *in-situ* stresses and the borehole axis. Drilling-induced tensile

fractures are also stress indicators since the strike of which can be referred to as the direction of the maximum horizontal stress.

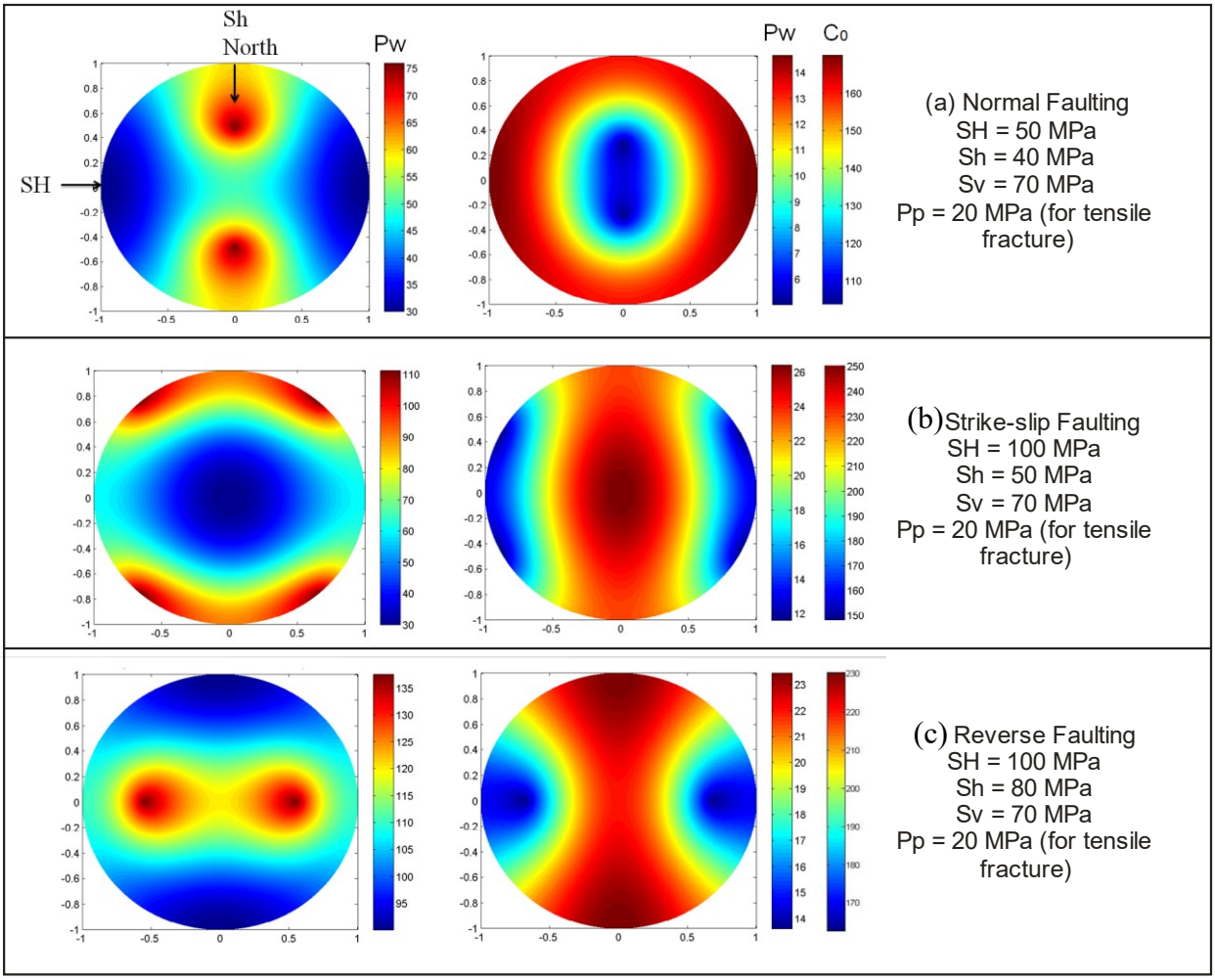

Figure 3.5 Lower hemisphere diagrams show the required well pressure and the rock strength to initiate drilling-induced tensile fractures (left column) and wellbore breakouts (middle column) for arbitrarily oriented wellbores in the normal faulting environment (top), the strike-slip faulting environment (middle) and the reverse faulting environment (bottom). The stress conditions are shown in the right column. For the tensile fracture case, the color indicates the highest borehole pressure to initiate DITFs for each borehole orientations. For the breakout case, the color indicates the lowest borehole pressure and rock strength to prevent borehole breakouts for each borehole orientations.

As mentioned in the overview, wellbore instability depends on the severity of fractures instead of the initiation of fractures. But without proper control of the mud weight (*i.e.*, the fluid pressure in the borehole), both DITFs and breakouts can threaten borehole stability. Therefore, based on the study conducted by *Peska and Zoback* (1995), a MATLAB^{TM} program was created to examine the borehole fracture initiations for all possible well orientations as illustrated in Fig. 3.5. Each point in the lower hemisphere diagram represents a well with a certain orientation, where the plunge and azimuth are indicated by the radial distance from the center and the azimuth angle, respectively.

The left panel shows the tendency for the initiation of the drilling-induced tensile fractures. The colors represent the upper limit of mud weight to generate DITFs. If the magnitude of mud weight is even higher than the minimum principal stress, hydraulic fractures can occur prior to reaching this high borehole pressure (*Zoback*, 2007). Noting that in the normal and reverse faulting environments, DITFs are expected to occur in approximately 60° deviated wells drilled at the azimuth of S_h and S_H, respectively. On the other hand, DITFs are more likely to exist in horizontal and sub-horizontal wells in the strike-slip faulting environment.

The right panel shows the tendency of borehole breakout initiation. The failure mechanism used here is the linearized Mohr-Coulomb failure criterion (*Peska and Zoback*, 1995). The colors in this case give the lower limits of both mud weight and rock strength required to avoid borehole breakout. Hence, we can consider that cold colors indicate more stable well orientations and *vice versa*. As shown in Fig. 3.5, in the strike-slip and reverse faulting regimes, breakouts are more likely to initiate in the vertical borehole or deviated well drilled in the direction of S_h; whereas, horizontal or sub-horizontal wellbores are more stable at the azimuth of S_H. Moreover, since higher compressions exist in those two stress regimes than that in the normal faulting regime, greater rock strengths and mud weights are required to prevent compressive failure so that wells are less stable. Conversely, in the normal faulting environment, vertical or slightly deviated wells in the direction of S_h are more desirable as the deviatoric stress will be less.

3.4 Examining the Mechanical Behavior of Tensile Fractures in the Laboratory

3.4.1 Introduction

Various lab measurements have been developed to estimate the mechanical properties and behavior of rocks, such as unconfined compressive strength (UCS) tests, and Brazilian tests. The stress and strain data or ultrasonic acoustic emissions recorded during these tests enable us to infer the moment the first crack is initiated. However, it is impossible to visualize the manner in which stresses change and cracks form resulted from external mechanical stresses particularly in opaque materials such as rock. On the contrary, a photoelasticity test allows for direct visualization of the stress state and the onset of cracking inside the tested sample during the test. This and similar techniques were utilized in several studies (*Galle*, 1959; *Galle and Wilhoit*, 1962; *Ito et al.*, 2004). The objective of this section is to simulate the initiations and propagations of drilling-induced tensile fractures on the borehole wall in the actual fields using glass cubes with holes drilled inside. In this article, we provide an overview of our laboratory measurement technique and the preliminary observations from three most representative test samples.

3.4.2 Experimental Methods

The basic components of glass is commonly SiO_2 or B_2O_3 (*Condon*, 1954). Upon cooling these two ingredients when they are melted, those atoms form a nonequilibrium arrangement with irregularly interconnected triangular or tetrahedral crystals (*Silver and Bray*, 1958). This is also known as the 'glassy state', which is usually owned by a supercooled liquid or an amorphous solid (*Silver and Bray*, 1958). Due to the random directions of crystalline symmetry axes, glass acts as a macro-isotropic material. Additionally, as glass has extremely low heat conductivity, the temperature is heterogeneous in the cooling process (*Condon*, 1954). Therefore, external layers cool faster than the inside. When the inner part finally cools down, it is in tension while pushing the outer parts into compression; hence, this process forms a parabolic stress profile throughout the glass (*Tomlinson et al.*, 2008). The residual stress inside the glass may also create uncertainty to our lab experiments.

Glass is similar to rocks in terms of the mechanical behavior, i.e., the tensile strength is much weaker than its compressive strength; the material is stable, perfectly elastic. That said, it does not differ significantly in many ways particularly except that it does not contain pores. Despite

this drawback, its transparency makes it an ideal material for photoelasticity tests. This was first revealed by physicist Seebeck (*Seebeck*, 1813; *Seebeck*, 1814) and Brewster (*Brewster*, 1814; 1816) in the early 19th century. Since then, glass has been widely utilized in the photoelasticity experiments, especially for the measurements of residual stress. Please refer to Appendix A for more details about what produces birefringence, how we observe it and how anisotropic stress states can produce it.

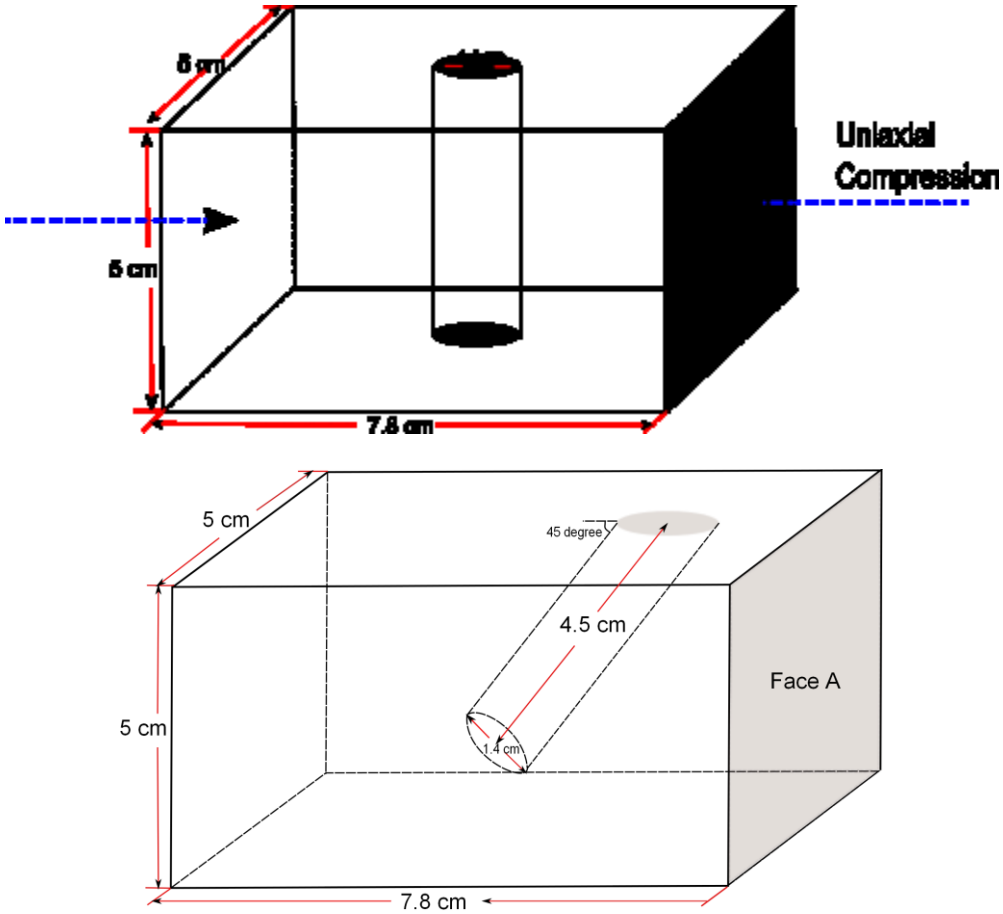

Figure 3.6 The schematic of the glass cubes. Top: Sample #1 with a hole drilled through vertically; bottom: Sample #2 and #3 with 45° inclined holes drilled more than half way through.

In our study, 'boreholes' with a 0.7 cm radius were drilled into such blocks with identical sizes of 7.8cm×5cm×5cm (Fig. 3.6). The boreholes were drilled either vertically (Sample #1) or deviated (Sample #2 and #3). Each pair of opposing faces on the blocks was parallel to within a tolerance of 25 μm, in order to ensure that the uniaxial compression could be applied uniformly.

The ratio of the diameter of the hole to the overall dimension of the glass cube should be small enough to avoid the influence of the borehole on the stresses at the outer face of the glass cube, and it also should be large enough, so that the disturbed birefringence could be seen easily (*Galle and Wilhoit*, 1962). Sample #3 was additionally mounted with strain gauges to capture the moment of the incipient cracking, which sometimes can be difficult to see visually.

After the drilling process, each block was placed centered on a load cell, and for some cases, the strain gauge was connected to a desktop computer for data display and recording. As indicated in Fig. 3.7, in addition to the load cell, the experimental setup consists of upper and lower platens, a hydraulic cylinder, two hand pumps, a computer monitor, a high quality SLR camera in 'movie' mode, and lower and upper risers. The load was applied continuously through the two hand pumps connected to the hydraulic cylinder until the expected tensile fractures initiated. Depending on the circumstances, the pressures were increased to further propagate these fractures. The monitor was filled with white placed behind the sample to provide a uniform source of polarized background light. The camera, placed on the opposite side of the glass block, had its lens covered by a polarizer filter. During the experiment, the polarized light is captured by a camera to reveal the birefringence, which shows areas of stress difference in the glass (*Hawkes*, 1968). We have not yet carried out quantitative analyses of the observed fringe patterns but they are extremely useful for qualitative assessment of the uniformity of stress within the sample and for detecting fracture initiation and growth in later analyses. Furthermore, the manner in which the borehole vicinity and fractures alter the stress pattern can also be observed during the tests. As indicated in Fig. 3.8, all those colors constitute 'stress contour lines', and the closer the contour lines are, the greater the stress concentration will be.

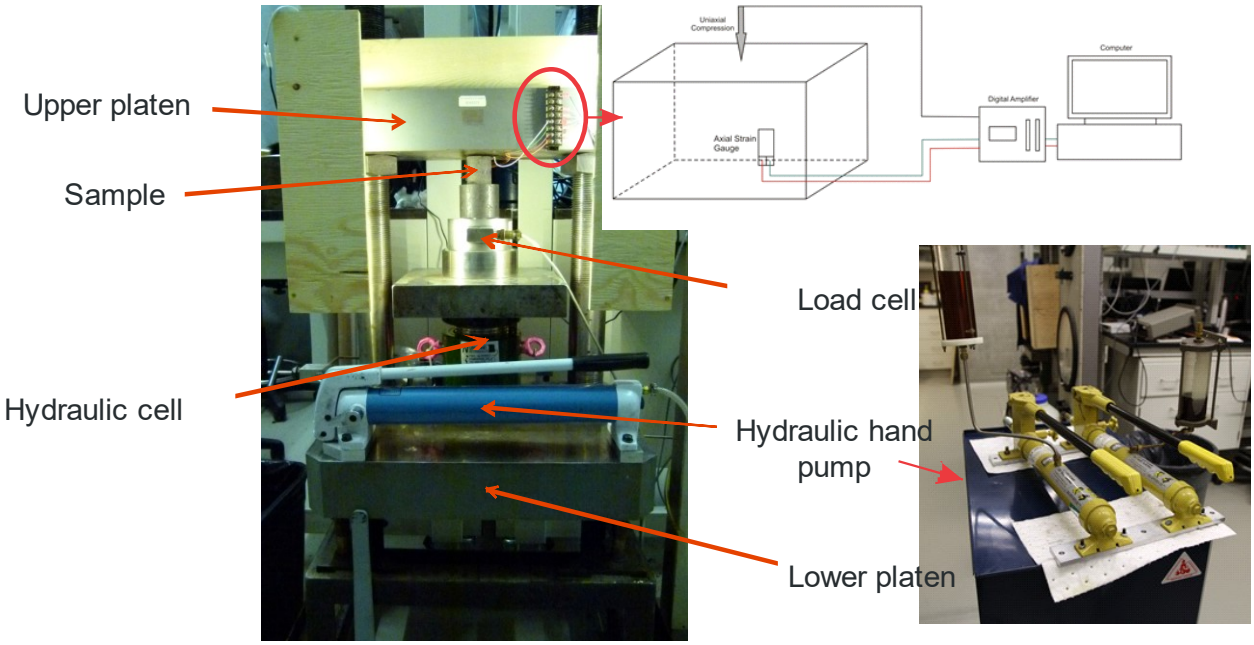

Figure 3.7 The experimental setup. The cartoon in the upper right shows the configuration of the data transmission and recording systems. The sample was placed in between the upper platen and the load cell. Pressures were applied on the double hydraulic hand pump and then transferred through the hydraulic system.

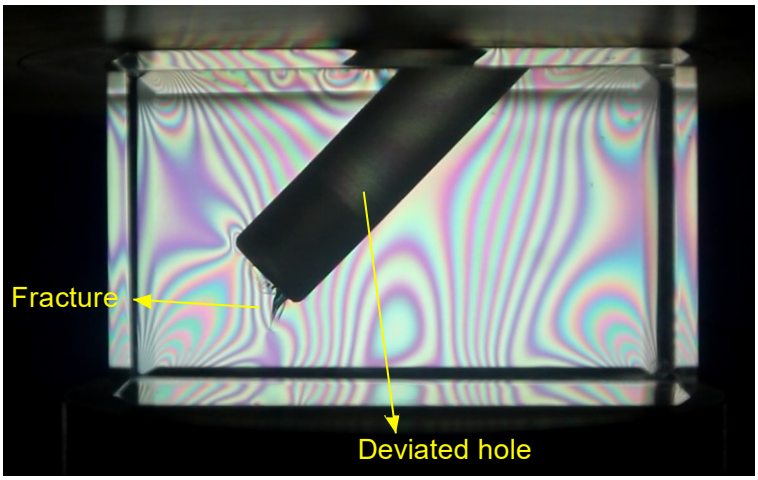

Figure 3.8 The birefringence revealed by the polarized light showing stress differences and disturbances caused by borehole vicinity and fractures. The detailed explanation can be found in the Appendix A.

3.4.3 Results

Sample # 1

As illustrated in Fig. 3.6, sample #1 contains a vertical through-going cylindrical borehole; the uniaxial load was applied perpendicular to the hole's axis. During the loading process, fractures #1 and #2 (Fig. 3.9) were generated simultaneously when the pressure of the fluid inside the hydraulic system reached 6.2 MPa. These two symmetrical fractures are representative of typical axial DITFs observed in the borehole and occurred essentially as expected.

The experiment did not cease at this point, and the levels of uniaxial compression continued to increase. This resulted in the production of new tensile fractures #3 at 8.27 MPa and #4 at 11.72MPa which propagated to intersect with fractures #1 and #2, respectively. They indicate that with continued stressing zones of tension shifted around the borehole and were sufficient to produce new fractures. Such phenomenon may have resulted from imperfect uniaxial stressing or from the interaction of edge effects in the finite sized samples.

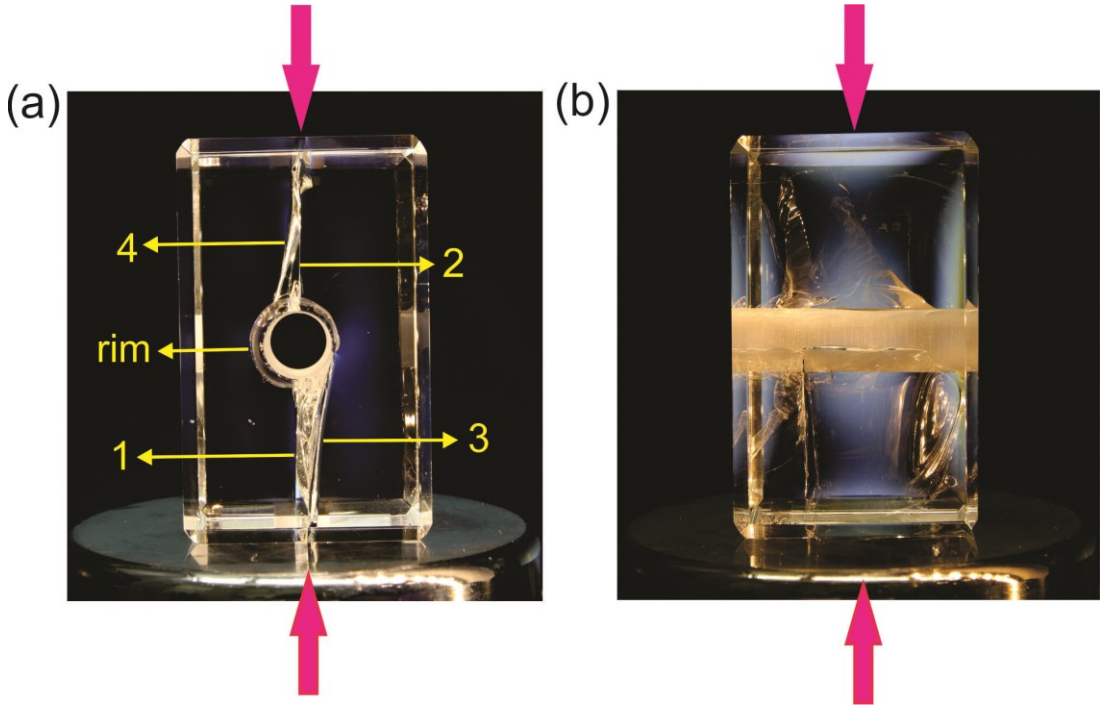

Figure 3.9 Sample #1and its fractures after the test. The left is in the front view, and the right one is in the side view showing axial fracture traces on the borehole wall. Magenta arrows indicate the direction of uniaxial compression. The number represent the time sequence those fractures form.

Sample #2

Sample #2 was drilled with a deviated hole (Fig. 3.6) that did not penetrate all the way through the block allowing stresses at the borehole bottom to also be studied. Sample #2 was uniaxially loaded applied perpendicular to Face A (Fig. 3.6), and three different fractures were created.

- Fracture #1 (Fig. 3.10b), which was twistedly occurred on the 'wall', was first initiated when the system reached 5.86 MPa, and then it propagated until it reached the bottom of the hole to form Fracture #2 at 7.58 MPa.
- A closer view of Fracture #2 was shown in Fig. 3.11. Fractures #1 and #2 were adjacent to each other, and Fracture #3 wasn't recorded in the video, which means that its initiation pressure cannot be determined. Both Fracture #2 and #3 were first grown in the direction parallel to the borehole axis forming petal fractures, and then Fracture #2 curved to be normal to the minimum principal stress forming a centerline fracture (*Davatzes and Hickman*, 2010; *Li and Schmitt*, 1998).
- Lastly, three *en echelon* tensile fractures (highlighted in red in Fig. 3.10c) were simultaneously generated near 9.65MPa on the upper side of the hole, and were eventually linked up together. It was clear that fractures grew from the hole into the medium.

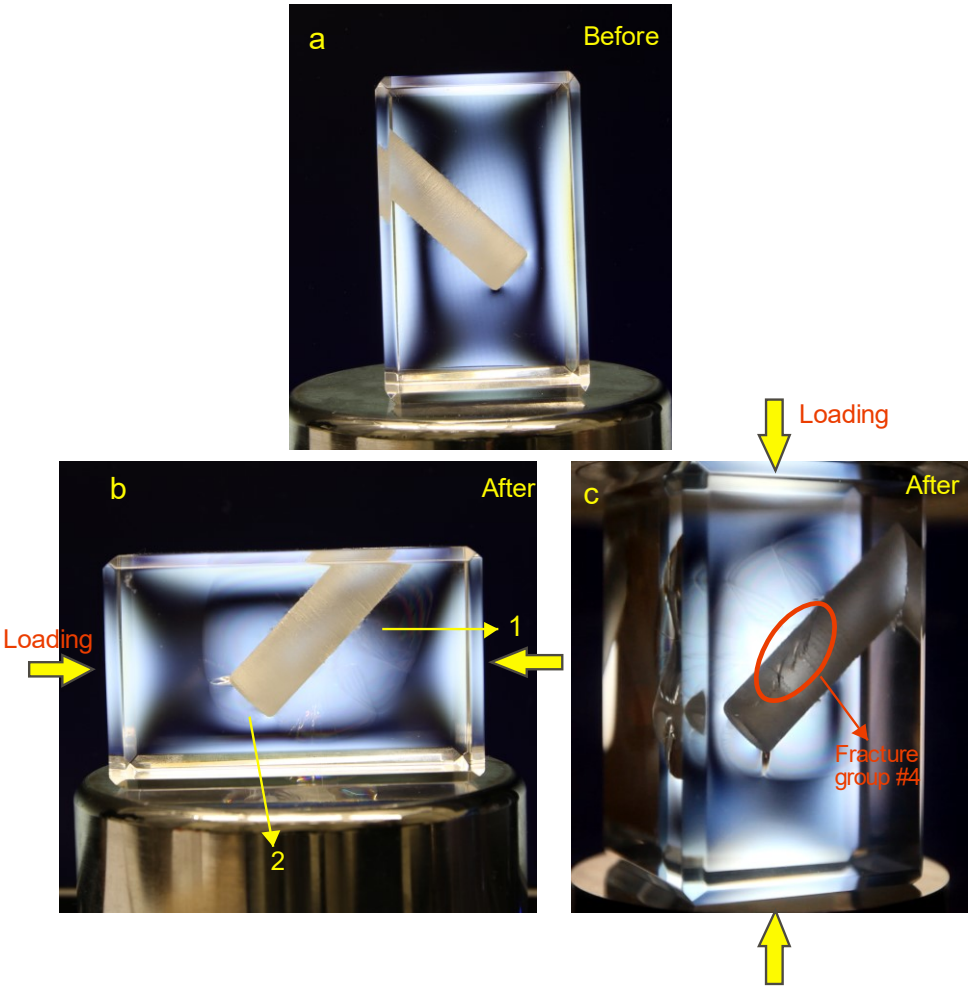

Figure 3.10 Sample #2 and its fractures before and after the test. Yellow arrows indicate the direction of uniaxial compression. The number represent the time sequence those fractures form.

(a)

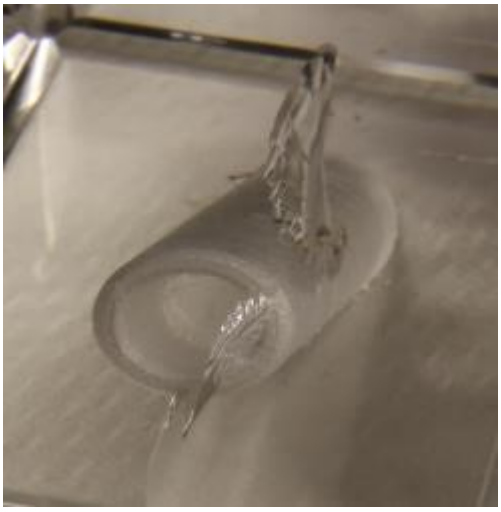

(b

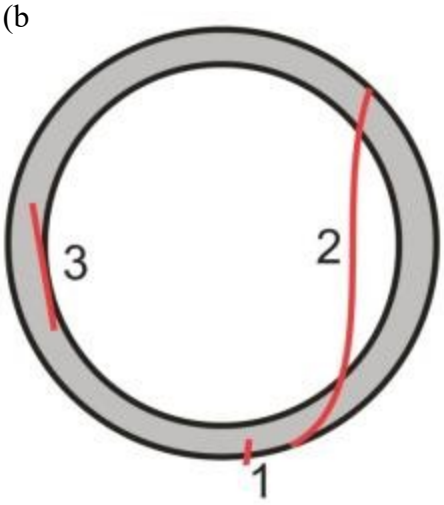

Figure 3.11 (a) The picture shows a closer view of bottom hole fractures for Sample #2. (b) A cartoon illustrates traces of the fractures intersecting on the bottom hole (red lines).

Sample #3

In this case, the sample was compressed perpendicular to Face B (Fig. 3.6 bottom). As the area of Face B is larger than that of Face A, it requires a higher load to produce fractures. During the experiment, no tensile fracture was initiated on the wall of the hole, but five bottom hole fractures were formed (Fig. 3.12, 3.13 & 3.14).

Fracture #1 was first initiated perpendicular to the bottom of the hole when the system was in 10.34 MPa. It continued to propagate while re-orienting its plane along the direction of loading until the load cell's limit was reached. The trajectory of Fracture #1 is illustrated in Fig. 3.14 (right).

The initiations of the remaining fractures were difficult to detect in the video and the stress at which they were produced is not well constrained. Strikes of these five fractures are orientated in different directions; however, since there is no confining pressure, all those directions are perpendicular to the least principal stress.

(a) (b

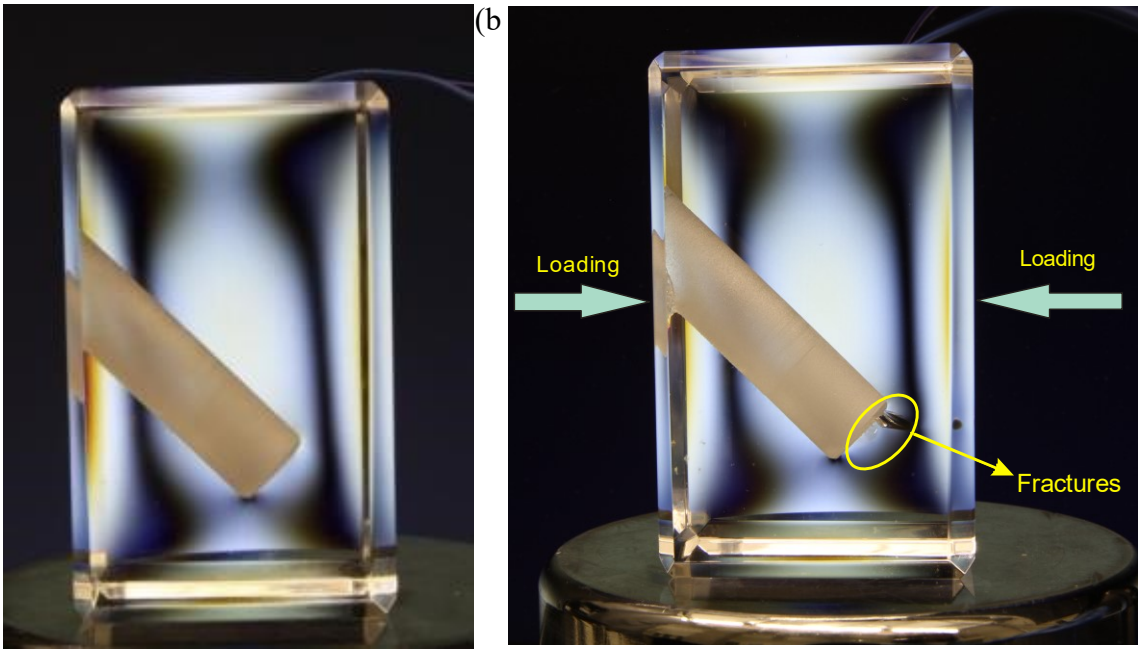

Figure 3.12 Sample #3 and its fractures before (a) and after the test (b).

Figure 3.13 A closer view of the bottom hole fractures for Sample #3.

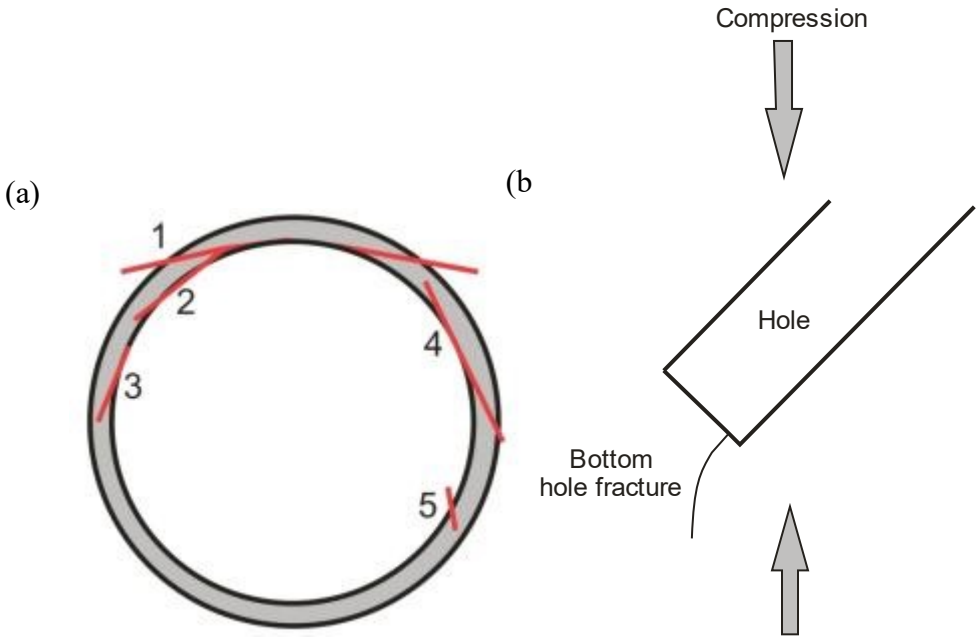

Figure 3.14 (a) Red lines show traces of the bottom hole fractures intersecting with the bottom hole (grey circle) for Sample #3. (b) The black curved line is shape of the bottom hole fracture #1 from the side view.

3.4.4 Discussion

Among all the photoelasticity tests we carried out, results for these three samples were the most representative for the three scenarios. Tensile fractures on the hole's wall in Sample #1 were mainly symmetrical axial tensile fractures and these were expected because the hole axis is aligned perpendicular with the uniaxial compression. The rim around the wall of the hole also exhibited some fracturing but this was generated during the process of strain recovery. Sample #2 and #3 had the same geometry with 45° deviated holes drilled more than half way through, but the directions of loading were different. Sample #2 clearly showed three *en echelon* tensile fractures, which were linked together, on the upper side of the hole caused by the nonalignment of the hole axis with respect to the uniaxial compression. On the other hand, tensile fractures on the lower side of the wall were created and propagated axially, and this phenomenon needed to be further investigated.

Additionally, fractures on the bottom of the hole in Sample #2 and #3 also reveal some interesting mechanical behavior. The first bottom hole fracture generated in Sample #2 was

initiated immediately after a wall fracture reached the bottom of the hole. However, for Sample #3, no wall fracture was created, and the initiation pressure for tensile fracture was higher than other two samples, which might due to a larger area contacted with the load. There was a similar pattern regarding to the propagation of bottom hole fractures: they tended to propagate along the direction of hole axis at first; then, due to a decreasing disturbance on the stress state by the bottom of the hole, they reoriented themselves to grow in the plane perpendicular to the least principal stress. As there was no confining stress, the strikes of bottom hole fractures became more distinct.

Although these three tests provide us a great insight on the mechanical behavior and characteristics of tensile fractures, there are still some drawbacks. First, the glass is not perfect. Flaws mainly originate in the two categories: induced cracks and pre-existing flaws in the glass, such as inclusions and severe cord (*Shand*, 1954). The induced cracks are formed due to the rotation speed of the drilling bit did not reach a desired speed to drill glasses. Based on Griffith's theory, the local stresses around the tip of a crack embedded in a brittle body can be several times higher than the external stress; therefore, with the existence of flaws, brittle bodies fail under the stresses lower than those necessary (*Griffith*, 1920; *Lawn and Wilshaw*, 1975; *Shand*, 1954). That said, those pre-existing or induced micro-cracks can weaken the strength of glasses. But in our preliminary experiments, our main focuses are on the azimuths of tensile fractures formed around the hole instead of the strength of specimens. So as long as we are cautious about the way of interpreting those strength data, we can still draw some reasonable conclusions. Second, our experimental setups are not as sophisticated as those for triaxial tests, so that limitations on adding confined pressure and having constantly increasing axial loading are inevitable, although it is difficult to see how such photoelasticity tests can be accomplished in triaxial conditions. Slightly improper lineup between the upper platen and lower platen can lead to unsymmetrical stress concentrations within the specimen. Moreover, since there is only one side that was recorded by the camera, some cracks could not even be detected in the video.

3.4.5 Conclusions

Three photoelasticity experiments were carried out by using glass cubes, and those enabled us to examine the failure mechanism of tensile fractures. The glass blocks had a uniform size of 5cm

× 5cm × 7.8 cm, and either a vertical or a 45° inclined hole was drilled into the glass. The specimens were subject to continuously increasing uniaxial compression until anticipated tensile fractures were created. The results of three preliminary tests were given in here. For tensile fractures on the hole's wall, Sample #1 has axial tensile fractures, on the other hand, Sample #2 contains three *en echelon* tensile fractures that eventually linked together away from the borehole. This proves that if one of the principal stresses is coincident with the hole trajectory, tensile fractures will grow axially; otherwise, *en echelon* tensile fractures will occur. Regarding to bottom hole tensile fractures, they strike in multiple directions due to a lack of any lateral confining stress in these initial tests. Moreover, they tend to propagate in the direction of hole axis first, and then curve to be perpendicular to the minimum principal stress. This study concentrates on the experimental method to mimic the situation in the real case, but there are still some limitations and assumptions. To improve future study, more advanced experimental setups are needed particularly ones in which at least one lateral stress can be applied. Moreover, a comparison between lab results and numerical models can offer us a more comprehensive view in the mechanical behaviors of tensile fracture.

3.5 References

Aadnoy (1990), In-situ stress directions from borehole fracture traces, *J Petrol Sci Eng*, *4*(2), 143-153.

Aadnoy, B. S., and J. S. Bell (1998), Classification of drilling-induced fractures and their relationship to in-situ atress directions, *The Log Analyst*, 27-42.

Al-Ajmi, A. M., and R. W. Zimmerman (2006), Stability analysis of vertical boreholes using the Mogi–Coulomb failure criterion, *International Journal of Rock Mechanics and Mining Sciences*, *43*(8), 1200-1211.

Amadei, B. (1983), *Rock anisotrpy and the theory of stress measurements*, Springer-Verlag, Berlin.

Barton, C., and D. Moos (2010), Geomechanical wellbore imaging: key to managing the asset life cycle., in *Dipmeter and borehole image log technology Memoir 92*, edited by M. Pöppelreiter, C. Garcia-Carballido and M. Kraaijveld, AAPG, Tulsa, p. 1-32.

Barton, C., M. D. Zoback, and K. L. Burns (1988), In-situ stress orientation and magnitude at the Fenton Geothermal Site, New Mexico, determined from wellbore breakouts, *Geophysical Research Letters*, *15*(5), 467-470.

Bell, J. S., and D. I. Gough (1982), The use of borehole breakouts in the study of crustal stress, *U.S. Geological Survey Special Report*, 539-557 pp.

Brewster, D. (1814), Results of some recent experiments on the properties impressed upon light by the action of glass raised to different temperatures, and cooled under different circumstances, *Phil. Trans. R. Soc. London*, *104*, 436-439.

Brewster, D. (1816), On new properties of heat, as exhibited in its propagation along plates of glass, *Phil. Trans. R. Soc. London*, *106*, 46-114.

Chan, J. (2013), Subsurface geophysical characterization of the crystalline canadian shield in Northeastern Alberta: Implications for geothermal development, M.Sc. Thesis, 259 pp, University of Alberta, Edmonton, Canada.

Condon, E. U. (1954), Physics of the glassy state. I. Constitution and structure, *American Journal of Physics*, *22*(2), 43-53.

Davatzes, N. C., and S. H. Hickman (2010), Stress, fracture, and fluid-flow analysis using acoustic and electrical image logs in hot fractured granites of the Coso Geothermal Field, California, U.S.A., in M. Poppelreiter, C. Garcia-Carballido, and M. Kraaijveld, eds., *Dipmeter and Borehole Image Log Technology: AAPG Memoir*, *92*, 34.

Fjaer, E., R. M. Holt, P. Horsrud, A. M. Raaen, and R. Risnes (2008), *Petroleum related rock mechanics*, Elsevier, Amsterdam, the Netherlands.

Galle, E. M. (1959), Photoelastic anlysis of the stresses near the bottom of a cylindrical cavity due to non-symmetrical loading, M.Sc. Thesis, Rice University.

Galle, E. M., and J. C. Wilhoit, Jr. (1962), Stresses around a wellbore due to internal pressure and unequal principal geostatic stresses, *Society of Petroleum Engineers Journal*, *2*(02).

Griffith, A. A. (1920), The phenomena of rupture and flow in solids, *Philosophical Transactions of the Royal Society (Lodon), Series A*, *221*, 163.

Hawkes, I. (1968), Photoelastic unidirectional (Pu) stress meter a borehole rock stress gage, The 10th U.S. Symposium on Rock Mechanics (USRMS), American Rock Mechanics Association, ARMA-68-0503, Austin, Texas, 20-22 May.

Hiramatsu, Y., and Y. Oka (1962), Stress around a shaft or level excavated in ground with a three-dimensional stress state., *Mem. Fac. Eng*, *24*(Kyoto Univ.), 56-76.

Ito, T., T. Abe, and K. Hayashi (2004), Utilization of ice as a rock-like material with transparency for physical experiment in laboratory, paper presented at Proceedings of the ISRM International Symposium 3rd ARMS, Millpress, Rotterdam.

Jia, Q., and D. R. Schmitt (2014), Effects of formation anisotropy on borehole stress concentrations: implications to drilling induced tensile fractures, 48th US Rock Mechanics / Geomechanics Symposium, American Rock Mechanics Association, Minneapolis, MN, USA, June 1-4.

Kirsch, E. G. (1898), The theory of elasticity and the need of the strength of materials (trans.), *Journal of the Association of German Engineers*, *42*, 797-807.

Lawn, B. R., and T. R. Wilshaw (1975), *Fracture of brittle solids*, Cambridge [Eng.] Cambridge University Press, 1975.

Li, Y., and D. R. Schmitt (1998), Drilling-induced core fractures and in situ stress, *Journal of Geophysical Research: Solid Earth*, *103*(B3), 5225-5239.

Peska, and Zoback (1995), Compressive and tensile failure of inclined well bores and determination of *in situ* stress and rock strength, *Journal of Geophysical Research-Solid Earth*, *100*(B7), 12791-12811.

Schmitt, D. R., C. A. Currie, and L. Zhang (2013), Crustal stress determination from boreholes and rock cores: Fundamental principles (vol 580, pg 1, 2012), *Tectonophysics*, *586*, 206-207.

Seebeck, T. J. (1813), Einige neue versuche und beobachtungen u¨ber spiegelung und brechung des Lichtes, *J. Chemie Physik*, *VII, Heft 3, 259–298, 382–384*.

Seebeck, T. J. (1814), Von den entoptischen farbenfiguren und den bedingungen ihrer bildung in glasern, *J. Chemie Physik*, *XII, 1–16i*.

Shand, E. B. (1954), Experimental study of fracture of glass: I, the fracture process, *Journal of the American Ceramic Society*, *37*(2), 52-60.

Shervais, J. W., D. R. Schmitt, D. Nielson, J. P. Evans, E. H. Christiansen, L. Morgan, W. C. P. Shanks, A. A. Propenenko, T. Lachmar, L. M. Liberty, D. D. Blackwell, J.M.Glenn, D. Champion, K. E. Potter, and J. A. Kessler (2013), First results from HOTSPOT: The Snake River Plain Scientific Drilling Project, Idaho *U.S.A.,Scientific Drilling*, 36-45.

Silver, A. H., and P. J. Bray (1958), Nuclear magnetic resonance absorption in glass. I. Nuclear quadrupole effects in boron oxide, Soda‐Boric Oxide, and Borosilicate glasses, *The Journal of Chemical Physics*, *29*(5), 984-990.

Tomlinson, R. A., G. C. Calvert, and A. R. Conway (2008), A photoelastic investigation into spontaneous glass fracture, paper presented at The XIth International Congress and Exposition, Society for Experimental Mechanics Inc., Orlando, Florida, 2-5, June.

Wang, Y., J. Don Scott, and M. B. Dusseault (1994), Borehole rupture from plastic yield to hydraulic fracture — A nonlinear model including elastoplasticity, *J Petrol Sci Eng*, *12*(2), 97-111.

Zheng, Z., J. Kemeny, and N. G. W. Cook (1989), Analysis of borehole breakouts, *Journal of Geophysical Research: Solid Earth*, *94*(B6), 7171-7182.

Zoback, M. D. (2007), *Reservoir geomechanics*, Cambridge University Press, Cambridge.

Chapter 4

The Closed-form Solution for Borehole Stress Calculations in an Anisotropic Homogeneous Formation

4.1 Introduction

Nowadays, highly deviated and horizontal wells are frequently drilling through anisotropic shale formations. Highly inclined boreholes are more vulnerable to failure (*Wilson and Willis*, 1986) and are more sensitive to the influence of such anisotropy (*Ong*, 1994; *Ong and Roegiers*, 1995). Traditionally, borehole stability analyses have assumed that the formations are elastically isotropic, an assumption that may be insufficient to deal with unconventional reservoirs (*Gazaniol et al.*, 1995). Part of the reason current practices are deficient is that the rock itself is more complicated. The formation is anisotropic by dint at all scales of its layering, its texture, and fracture sets. This existence of this anisotropy has long been known but its implications for wellbore failure have not been extensively investigated. Consequently, to provide further insight of the situation in actual fields, having a good knowledge of the wellbore failure mechanisms associated with anisotropic formations becomes critical for reducing the likelihood of borehole instabilities leading to failure.

Shales constitute of about 75% of the sections encountered by drilling. Normally, we expect shale to be transversely isotropic, abbreviated as TI, due to the symmetry of elastic and structural properties (*Aadnoy and Bernt*, 1988; *Cholach and Schmitt*, 2006; *Hornby*, 1995; *Johnston and Christensen*, 1992; *Kaarsberg*, 1959; *Wong et al.*, 2008). Shale anisotropy depends on porosity, kerogen content, fluid interaction and microcracks (*Dewhurst and Siggins*, 2006; *Vernik and Nur*, 1992; *Vernik and Liu*, 1997). The elastic constants of shale can be estimated using sonic logging tools (*Walsh et al.*, 2008) and laboratory ultrasonic wave speed measurements (*Melendez and Schmitt*, 2011; *Melendez and Schmitt*, 2013; *Sarout and Gueguen*, 2008; *Vernik and Nur*, 1992; *Vernik and Liu*, 1997). To quantify the degree of anisotropy, *Thomsen* (1986) developed the anisotropy factors ε, γ and δ, which are unitless and are as functions of elastic modules (Eq. 4.34). The values of those anisotropy factors decrease with decreasing degree of anisotropy.

Other than the borehole stresses in isotropic formations discussed in Chapter 3, the analytical solution of the near-wellbore stress calculation in anisotropic formations was developed by *Lekhnitskii* (1981) and *Amadei* (1983). Numerous later contributions (*Aadnoy*, 1987; *Gaede et al.*, 2012; *Ong*, 1994; *Ong and Roegiers*, 1995; *Vahid and Ahmad*, 2011) have been based on these pioneering developments. The Lekhnitskii-Amadei (L-A) anisotropic model necessitates the use of three coordinate systems that describe the orientations of i) the *in-situ* far-field stress, ii) the rock anisotropy, and iii) the borehole. The inputs to this model include the *in-situ* stress (e.g. magnitudes of three principal stresses and Eulerian angles providing their orientations), the well pressure, the rock stiffness matrix, the orientations of the anisotropy, and the borehole azimuth and inclination. This comprehensive L-A solution can also be reduced to the Hiramatsu and Oka solution to calculate stress distributions in isotropic formations (*Gaede et al.*, 2012).

The purpose of chapter 4 is to assess the impacts of rock anisotropy (mainly transversely isotropy, TI) on near-wellbore stress distribution using the L-A solution. First, earlier analytical work (*Amadei*, 1983; *Lekhnitskii*, 1981; *Ong*, 1994) is heavily referenced to revisit the solution for borehole stress estimations in an anisotropic medium. Then, sensitivity studies are carried out to provide us a further insight of the variations in stress distributions as a function of rock anisotropy utilizing a MATLAB^{TM} based program (provided to the reader in Appendix B), which is not restricted to any specific borehole orientations, in-situ stresses or rock anisotropies. This chapter and the following chapter are developed from one of my conference papers (*Jia and Schmitt*, 2014), and hopefully, they will be submitted for publication in the journal 'Computer & Geosciences' in the summer of 2015.

4.2 General Assumptions

The models discussed in this paper consider a circular borehole drilled in a linear elastic, homogeneous anisotropic formation without chemical, temperature or poro-elastic effects. Body forces are also neglected in this solution. Moreover, we assume the borehole is infinitely long and is subjected to both the far field stress and internal mud pressure both of which do not vary along the borehole axis. This can be referred to as the generalized plane strain assumption: a more generalized case comparing to the classical plane strain formulation.

The classical plane strain formulation is not applicable to anisotropic media except for some certain situations. This is because that as long as any of the planes of elastic symmetry does not coincide with the x-y plane, the out-of-plane displacement (*w*) is no longer zero (*Lekhnitskii*, 1981). Therefore, a generalized plain strain method is utilized in the anisotropic model allowing the orientation of the wellbore to be independent of the directions of the far field stresses and the symmetry axis of anisotropic medium (*Ong*, 1994). In that sense, in all planes normal to the x-y plane, all components of stress, strain, displacement and forces do not change (*Amadei*, 1983), which means,

$$\frac{\partial u_x}{\partial z} = \frac{\partial u_y}{\partial z} = \frac{\partial u_z}{\partial z} = 0 \tag{4.1}$$

where u_x, u_y and u_z are displacements along the x, y and z directions, respectively, and they are functions of x and y alone.

4.3 Model Geometry and Coordinate System Transformations

To better simulate situations in actual fields, as illustrated in Fig. 4.1, three Cartesian coordinate systems are defined by different plunges (β) and trends (α or α'= 90-α) with respect to the global coordinate system (X-Y-Z) (*Ong and Roegiers*, 1993), these are the:

- Borehole coordinate system X_1-Y_1-Z_1 with the inclination angle β_1 and the azimuthal angle α_1 (the Z_1-axis is aligned with the borehole axis and the X_1-axis points at the lowest side of the wellbore)
- In-situ stress coordinate system X_2-Y_2-Z_2 with a trend angle of α_2 and the plunge β_2=0
- Rock elastic property coordinate system X_3-Y_3-Z_3 with the plunge angle β_3 and the azimuthal angle α_3.

The principal *in-situ* stress tensor can be expressed in the following matrix form:

$$\sigma = \begin{bmatrix} S_H & 0 & 0 \\ 0 & S_h & 0 \\ 0 & 0 & S_v \end{bmatrix} \tag{4.2}$$

where S_H, S_h and S_v are the maximum horizontal stress, the minimum horizontal stress and the vertical stress, respectively. The stress coordinate system are attached to the directions of three principal stresses with S_H, S_h and S_v aligned with X_2, Y_2 and Z_2 axis, respectively. Note that in a

real problem, one must consider further the relationship between this co-ordinate system and the geographic co-ordinates but this is not necessary to the current discussion. To simplify our model, S_v is assumed to be always pointing at the opposite direction of the Z-axis. As the stability analysis focuses on the near-wellbore environment, both the stress tensor $\{\sigma\}_s$ and the compliances $[S]$ must be rotated into the borehole coordinate system. After some mathematical manipulations, these transformations can be written in the following form (*Amadei*, 1983; *Ong*, 1994; *Ong and Roegiers*, 1993):

$$\{\sigma\}_b = [O_\sigma][R_\epsilon]^t\{\sigma\}_s$$

$$[S]_b = [P_\epsilon][M'_\sigma]^t[S]_s[M'_\sigma][P_\epsilon]^t \tag{4.3}$$

Where subscripts s and b indicate *in-situ* stress and borehole coordinate systems, respectively; matrices with subscript σ are stress transformation matrices, whereas matrices with subscripts ∈ refer to strain transformation matrices, and t indicates the transpose operator. The transformation matrixes can be expressed as the following in a general form [T] (*Ong*, 1994):

$$[T_\sigma] = \begin{pmatrix} l_1^2 & m_1^2 & n_1^2 & 2m_1n_1 & 2n_1l_1 & 2l_1m_1 \\ l_2^2 & m_2^2 & n_2^2 & 2m_2n_2 & 2n_2l_2 & 2l_2m_2 \\ l_3^2 & m_3^2 & n_3^2 & 2m_3n_3 & 2n_3l_3 & 2l_3m_3 \\ l_2l_3 & m_2m_3 & n_2n_3 & m_2n_3+m_3n_2 & n_2l_3+n_3l_2 & l_2m_3+l_3m_2 \\ l_3l_1 & m_3m_1 & n_3n_1 & m_1n_3+m_3n_1 & n_1l_3+n_3l_1 & l_1m_3+l_3m_1 \\ l_1l_2 & m_1m_2 & n_1n_2 & m_1n_2+m_2n_1 & n_1l_2+n_2l_1 & l_1m_2+l_2m_1 \end{pmatrix} \tag{4.4}$$

$$[T_\epsilon] = \begin{pmatrix} l_1^2 & m_1^2 & n_1^2 & m_1n_1 & n_1l_1 & l_1m_1 \\ l_2^2 & m_2^2 & n_2^2 & m_2n_2 & n_2l_2 & l_2m_2 \\ l_3^2 & m_3^2 & n_3^2 & m_3n_3 & n_3l_3 & l_3m_3 \\ 2l_2l_3 & 2m_2m_3 & 2n_2n_3 & m_2n_3+m_3n_2 & n_2l_3+n_3l_2 & l_2m_3+l_3m_2 \\ 2l_3l_1 & 2m_3m_1 & 2n_3n_1 & m_1n_3+m_3n_1 & n_1l_3+n_3l_1 & l_1m_3+l_3m_1 \\ 2l_1l_2 & 2m_1m_2 & 2n_1n_2 & m_1n_2+m_2n_1 & n_1l_2+n_2l_1 & l_1m_2+l_2m_1 \end{pmatrix} \tag{4.5}$$

where l, m and n are direction cosines described in Eq. 3.2.

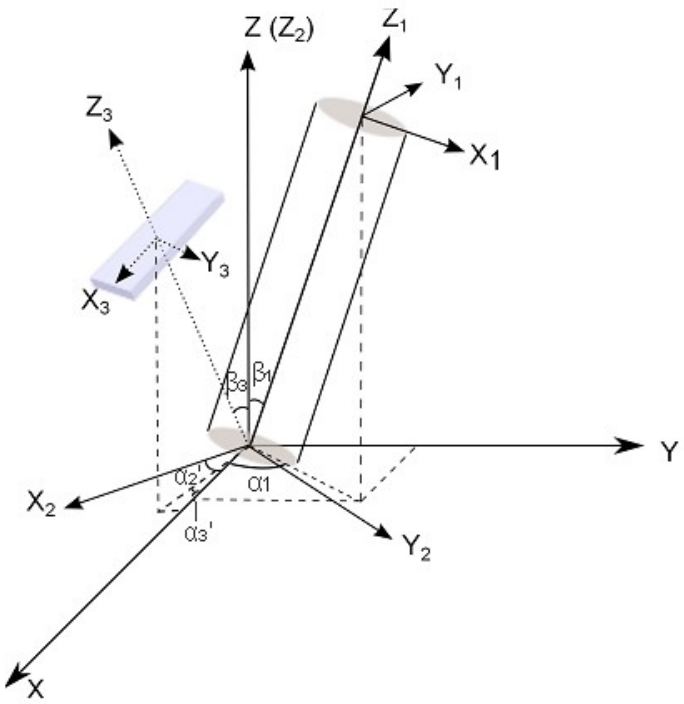

Figure 4.1 Schematic of coordinate reference frames for the anisotropic model.

In problems solving borehole stresses, the cylindrical coordinate system prevails; therefore, it is necessary to transfer stress from a Cartesian coordinate (*x, y, z*) into a cylindrical system (*r, θ, ξ*). Note that the new axis *r* and *θ* are corresponding to X_1 and Y_1, and *ξ* axis coincides with Z_1 meaning $\beta = 0$. Hence, the new direction cosines are (*Ong*, 1994):

$$\begin{gathered} l_1 = \cos\theta\,, \qquad l_2 = -\sin\theta\,, \qquad l_3 = 0 \\ m_1 = \sin\theta\,,\ m_2 = \cos\theta\,,\ m_3 = 0 \\ n_1 = 0, \qquad n_2 = 0, \qquad n_3 = 1 \end{gathered} \tag{4.7}$$

and the expression for the transformed stress is:

$$\begin{Bmatrix} \sigma_r \\ \sigma_\theta \\ \sigma_\xi \\ \tau_{\theta\xi} \\ \tau_{r\xi} \\ \tau_{r\theta} \end{Bmatrix} = \begin{bmatrix} \cos^2\theta & \sin^2\theta & 0 & 0 & 0 & \sin 2\theta \\ \sin^2\theta & \cos^2\theta & 0 & 0 & 0 & -\sin 2\theta \\ 0 & 0 & 1 & 0 & 0 & 0 \\ 0 & 0 & 0 & \cos\theta & -\sin\theta & 0 \\ 0 & 0 & 0 & \sin\theta & \cos\theta & 0 \\ -\frac{1}{2}\sin 2\theta & \frac{1}{2}\sin 2\theta & 0 & 0 & 0 & \cos 2\theta \end{bmatrix} \begin{Bmatrix} \sigma_x \\ \sigma_y \\ \sigma_z \\ \tau_{yz} \\ \tau_{xz} \\ \tau_{xy} \end{Bmatrix} \tag{4.8}$$

4.4 General Solution for Stress Components

For any elastic and static problems involving stress, strain and displacement, they must satisfy the following conditions (*Amadei*, 1983):

- Equations of equilibrium;
- Strain-displacement relations;
- Equations of compatibility for strains
- Constitutive relations; and,
- Boundary conditions.

The generalized plane strain Beltrami-Michell equations of compatibility, differential equations derived from the first four conditions in the above, indicates the stress state of an infinitesimal cube in an anisotropic medium, which can be expressed in the following form (*Ong*, 1994):

$$\sigma_x = \frac{\partial^2 F}{\partial y^2}, \qquad \sigma_y = \frac{\partial^2 F}{\partial x^2}, \qquad \tau_{xy} = -\frac{\partial^2 F}{\partial x \partial y}$$

$$\tau_{xz} = \frac{\partial \Psi}{\partial y}, \ \tau_{yz} = -\frac{\partial \Psi}{\partial x} \tag{4.9}$$

and the compact solutions are

$$\begin{aligned} L_4 F + L_3 \Psi &= 0 \\ L_3 F + L_2 \Psi &= 0 \end{aligned} \tag{4.10}$$

where F and Ψ are stress functions, L_2, L_3 and L_4 are the linear differential operators, which can be written as:

$$L_2 = \beta_{44} \frac{\partial^2}{\partial x^2} - 2\beta_{45} \frac{\partial^2}{\partial x \partial y} + \beta_{55} \frac{\partial^2}{\partial y^2}$$

$$L_3 = -\beta_{24} \frac{\partial^3}{\partial x^3} + (\beta_{25} + \beta_{46}) \frac{\partial^3}{\partial x^2 \partial y} - (\beta_{14} + \beta_{56}) \frac{\partial^3}{\partial x \partial y^2} + \beta_{15} \frac{\partial^3}{\partial y} \tag{4.11}$$

$$L_4 = \beta_{22} \frac{\partial^4}{\partial x^4} - 2\beta_{26} \frac{\partial^4}{\partial x^3 \partial y} - 2(\beta_{12} + \beta_{66}) \frac{\partial^4}{\partial x^2 \partial y^2} - 2\beta_{16} \frac{\partial^4}{\partial x \partial y^3} + \beta_{11} \frac{\partial^4}{\partial y^4}$$

and β_{ij} is the reduced strain coefficients (*Lekhnitskii*, 1981; *Ong*, 1994), and it is defined as a function of components of the compliance matrix, a_{ij}:

$$\beta_{ij} = a_{ij} - \frac{a_{i3}a_{j3}}{a_{33}} \quad (i,j = 1,2,4,5,6) \tag{4.12}$$

With Eq. 4.10, the following equations can be achieved:

$$(L_4L_2 - L_3L_3)F = 0$$
$$(L_3L_3 - L_4L_2)\Psi = 0 \tag{4.13}$$

The first equation of Eq. 4.13 can be written as:

$$f(\mu) = l_4(\mu)l_2(\mu) - l_3^2(\mu) = 0 \tag{4.14}$$

where

$$l_2(\mu) = \beta_{55}\mu^2 - 2\beta_{45}\mu + \beta_{44}$$
$$l_3(\mu) = \beta_{15}\mu^3 - (\beta_{14} + \beta_{56})\mu^2 + (\beta_{25} + \beta_{46})\mu - \beta_{24}$$
$$l_4(\mu) = \beta_{11}\mu^4 - 2\beta_{16}\mu^3 + (2\beta_{12} + \beta_{66})\mu^2 - 2\beta_{26}\mu + \beta_{22} \tag{4.15}$$

$f(\mu)$ is the characteristic equation having six roots μ_i (i = 1,…,6). The roots are always complex or purely imaginary, and half of them (μ_1, μ_2, μ_3) are always conjugates of the other half ($\bar{\mu}_1$, $\bar{\mu}_2$, $\bar{\mu}_3$) (*Lekhnitskii*, 1981). Therefore, the general expressions for *F* and ψ take the following form (*Ong*, 1994):

$$F = 2\Re[F_1(z_1) + F_2(z_2) + F_3(z_3)]$$
$$\Psi = 2\Re\left[\lambda_1F_1'(z_1) + \lambda_2F_2'(z_2) + \frac{1}{\lambda_3}F_3'(z_3)\right] \tag{4.16}$$

where

(i) $\Re$ is the operation of taking the real part of the expression in the brackets.

(ii) $F_i(z_i)$ (i=1,2,3) are analytical functions of $z_i = x + \mu_i y$, and the prime refers to a derivation to z_i.

(iii) λ_i (i=1,2,3) are the complex numbers, defined as

$$\lambda_1 = -\frac{l_3(\mu_1)}{l_2(\mu_1)},\ \lambda_2 = -\frac{l_3(\mu_2)}{l_2(\mu_2)},\ \lambda_3 = -\frac{l_3(\mu_3)}{l_4(\mu_3)} \tag{4.17}$$

Lekhnitskii (1981) introduced three analytic functions, $\Phi_i(z_i)$ (i=1,2,3), which are expressed as:

$$\Phi_1(z_1) = F_1'(z_1),\ \Phi_2(z_2) = F_2'(z_2),\ \Phi_3(z_3) = \frac{1}{\lambda_3}F_3'(z_3) \tag{4.18}$$

Combining Eq. 4.16 and 4.18, the first derivatives of F with respect to x and y are:

$$\frac{\partial F}{\partial x} = 2\Re[\Phi_1(z_1) + \Phi_2(z_2) + \lambda_3\Phi_3(z_3)]$$

$$\frac{\partial F}{\partial y} = 2\Re[\mu_1\Phi_1(z_1) + \mu_2\Phi_2(z_2) + \mu_3\lambda_3\Phi_3(z_3)] \tag{4.19}$$

And the expression for Ψ

$$\Psi = 2\Re[\lambda_1\Phi_1(z_1) + \lambda_2\Phi_2(z_2) + \Phi_3(z_3)] \tag{4.20}$$

Utilizing Eq. 4.9 and 4.20, the general expressions for the drilling-induced stress components are (*Ong*, 1994):

$$\sigma_{xb} = 2Re[\mu_1^2\Phi_1'(z_1) + \mu_2^2\Phi_2'(z_2) + \lambda_3\mu_3^2\Phi_3'(z_3)]$$

$$\sigma_{yb} = 2Re[\Phi_1'(z_1) + \Phi_2'(z_2) + \lambda_3\Phi_3'(z_3)]$$

$$\tau_{xyb} = -2Re[\mu_1\Phi_1'(z_1) + \mu_2\Phi_2'(z_2) + \lambda_3\mu_3\Phi_3'(z_3)]$$

$$\tau_{xzb} = 2Re[\lambda_1\mu_1\Phi_1'(z_1) + \lambda_2\mu_2\Phi_2'(z_2) + \mu_3\Phi_3'(z_3)]$$

$$\tau_{yzb} = -2Re[\lambda_1\Phi_1'(z_1) + \lambda_2\Phi_2'(z_2) + \Phi_3'(z_3)] \tag{4.21}$$

The general solution of the stress distribution which consists of the drilling-induced stress σ_b superimposed onto the boundary stresses, σ_0, and the expressions are:

$$\sigma_x = \sigma_{x0} + \sigma_{xb} = \sigma_{x0} + 2Re[\mu_1^2\Phi_1'(z_1) + \mu_2^2\Phi_2'(z_2) + \lambda_3\mu_3^2\Phi_3'(z_3)]$$

$$\sigma_y = \sigma_{y0} + \sigma_{yb} = \sigma_{y0} + 2Re[\Phi_1'(z_1) + \Phi_2'(z_2) + \lambda_3\Phi_3'(z_3)]$$

$$\tau_{xy} = \tau_{xy0} + \tau_{xyb} = \tau_{xy0} - 2Re[\mu_1\Phi_1'(z_1) + \mu_2\Phi_2'(z_2) + \lambda_3\mu_3\Phi_3'(z_3)]$$

$$\tau_{xz} = \tau_{xz0} + \tau_{xzb} = \tau_{xz0} + 2Re[\lambda_1\mu_1\Phi_1'(z_1) + \lambda_2\mu_2\Phi_2'(z_2) + \mu_3\Phi_3'(z_3)]$$

$$\tau_{yz} = \tau_{yz0} + \tau_{yzb} = \tau_{yz0} - 2Re[\lambda_1\Phi_1'(z_1) + \lambda_2\Phi_2'(z_2) + \Phi_3'(z_3)] \tag{4.22}$$

where the derivatives of $\Phi_i(z_i)$ will be provided in the next section. Based on the generalized plane strain formulation, the axial stress σ_z can be expressed in the following form:

$$\sigma_z = \sigma_{z0} - \frac{1}{a_{33}}\left(a_{31}\sigma_{xb} + a_{32}\sigma_{yb} + a_{34}\tau_{yzb} + a_{35}\tau_{xzb} + a_{36}\tau_{xyb}\right) \tag{4.23}$$

4.5 General Expressions for the Analytic Function $\Phi_i(z_i)$

The problem for borehole stress calculations is now reduced to the derivation of the three analytic functions $\Phi_i(z_i)$, which are functions of the complex variable $z_i = x + \mu_i y$ in a region with cross section S. As μ_i is always complex or imaginary, z_i becomes the following expression (*Amadei*, 1983):

$$z_i = x + \mu_i y = x + (\alpha_i + i\beta_i)y = x_i + iy_i \tag{4.24}$$

where

$$x_i = x + \alpha_i y, \qquad y_i = \beta_i y \quad (i = 1,2,3) \tag{4.25}$$

Hence, $\Phi_i(z_i)$ are determined in the regions with cross sections S_1, S_2, and S_3 (Fig. 4.2), which are mapped based on S through the affine transformations (*Lekhnitskii*, 1981). To express the cross sections into the cylindrical system, one can write the axis as:

$$x_i = a(\cos\theta + \alpha_i \sin\theta), \quad y_i = a\beta_i \sin\theta \tag{4.26}$$

Lekhnitskii (1981) proposed to conformably map S_i onto the ζ_i plane and the exterior of the unit circle to solve the problem, as such, the mapping functions become:

$$\frac{z_i}{a} = \frac{1-i\mu_i}{2}\zeta_i + \frac{1+i\mu_i}{2}\frac{1}{\zeta_i} \tag{4.27}$$

whose function inverse is:

$$\zeta_i = \frac{\frac{z_i}{a} + \sqrt{\left(\frac{z_i}{a}\right)^2 - 1 - \mu_i^2}}{1-i\mu_i} \tag{4.28}$$

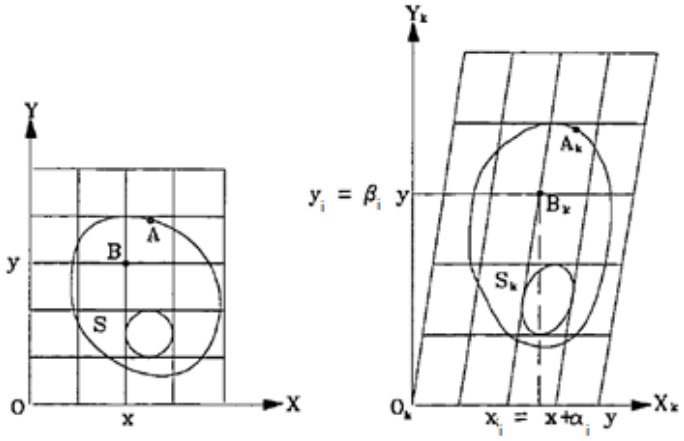

Figure 4.2 Geometric representation of an affine transformation (*Ong*, 1994).

After conformal mapping, the analytic functions $\Phi_i(z_i)$ were introduced by as the following (*Lekhnitskii*, 1981):

$$\Phi_i(z_i) = A_i ln\zeta_i + \sum_{m=1}^{\infty} A_{im}\zeta_i^{-m} \tag{4.29}$$

where A_i and A_{im} are coefficients related to boundary conditions, and their derivation processes will not be given in this thesis. After substituting the expressions of A_{im} into Eq. 4.29, the analytic functions are shown as the following formulae (*Ong*, 1994):

$$\Phi_1(z_1) = A_1 ln\zeta_1 + \frac{1}{\Delta}\sum_{m=1}^{\infty}\left\{\left[\bar{a}_m(\mu_2 - \lambda_2\lambda_3\mu_3) + \bar{b}_m(\lambda_2\lambda_3 - 1) + \bar{c}_m\lambda_3(\mu_3 - \mu_2)\right]\frac{1}{\zeta_1^m}\right\}$$

$$\Phi_2(z_2) = A_2 ln\zeta_2 + \frac{1}{\Delta}\sum_{m=1}^{\infty}\left\{\left[\bar{a}_m(\lambda_1\lambda_3\mu_3 - \mu_1) + \bar{b}_m(1 - \lambda_1\lambda_3) + \bar{c}_m\lambda_3(\mu_1 - \mu_3)\right]\frac{1}{\zeta_2^m}\right\}$$

$$\Phi_3(z_3) = A_3 ln\zeta_3 + \frac{1}{\Delta}\sum_{m=1}^{\infty}\left\{\left[\bar{a}_m(\mu_1\lambda_2 - \mu_2\lambda_1) + \bar{b}_m(\lambda_1 - \lambda_2) + \bar{c}_m(\mu_2 - \mu_1)\right]\frac{1}{\zeta_3^m}\right\} \tag{4.30}$$

where

$$\Delta = \mu_2 - \mu_1 + \lambda_3\lambda_2(\mu_1 - \mu_3) + \lambda_1\lambda_3(\mu_3 - \mu_2) \tag{4.31}$$

After applying boundary conditions, one can achieve the following:

$$\bar{a}_1 = \frac{a}{2}\left[i\tau_{xy0} - \left(\sigma_{y0} - P_w\right)\right]$$

$$\bar{b}_1 = \frac{a}{2}\left[\tau_{xy0} - i(\sigma_{x0} - P_w)\right]$$

$$\bar{c}_1 = \frac{a}{2}\left[\tau_{yz0} - i\tau_{xz0}\right] \tag{4.32}$$

and for $\bar{a}_m$, $\bar{b}_m$, and $\bar{c}_m$, if m ≥ 2, they are zero. A_i (i=1,2,3) are also zero.

Therefore, the final forms of the analytic functions $\Phi_i(z_i)$ are (*Ong*, 1994):

$$\Phi_1'(z_1) = -\frac{1}{2\Delta\zeta_1\sqrt{\left(\frac{z_1}{a}\right)^2 - 1 - \mu_1^2}}\left[\left(i\tau_{xy0} - \sigma_{y0} + P_w\right)(\mu_2 - \lambda_2\lambda_3\mu_3)\right.$$
$$\left. + \left(\tau_{xy0} - i\sigma_{x0} + iP_w\right)(\lambda_2\lambda_3 - 1) + \left(\tau_{yz0} - i\tau_{xz0}\right)\lambda_3(\mu_3 - \mu_2)\right]$$

$$\Phi_2'(z_2) = -\frac{1}{2\Delta\zeta_2\sqrt{\left(\frac{z_2}{a}\right)^2 - 1 - \mu_2^2}}\left[\left(i\tau_{xy0} - \sigma_{y0} + P_w\right)(\lambda_1\lambda_3\mu_3 - \mu_1)\right.$$
$$\left. + \left(\tau_{xy0} - i\sigma_{x0} + iP_w\right)(1 - \lambda_1\lambda_3) + \left(\tau_{yz0} - i\tau_{xz0}\right)\lambda_3(\mu_1 - \mu_3)\right]$$

$$\Phi_3'(z_3) = -\frac{1}{2\Delta\zeta_3\sqrt{\left(\frac{z_3}{a}\right)^2 - 1 - \mu_3^2}}\left[\left(i\tau_{xy0} - \sigma_{y0} + P_w\right)(\mu_1\lambda_2 - \mu_2\lambda_1)\right.$$
$$\left. + \left(\tau_{xy0} - i\sigma_{x0} + iP_w\right)(\lambda_1 - \lambda_2) + \left(\tau_{yz0} - i\tau_{xz0}\right)(\mu_2 - \mu_1)\right]$$

(4.33)

Inserting Eq. 4.33 into Eq. 4.22, one can get the solution for the stress distribution in the vicinity of borehole in a homogeneous anisotropic medium.

4.6 The Effects of Rock Anisotropy on Near-wellbore Stress Distributions

4.6.1 Boundary Conditions and Material Mechanical Properties

Based on the analytical solution introduced in the above, a MATLAB^{TM} based program was created to help us visualize the stress distribution around the borehole wall (the program code is provided in Appendix B). Utilizing this program, parametric studies are carried out to investigate the variation of near-wellbore stress concentrations as a function of the degree of intrinsic formation anisotropy.

Table 4.1 Boundary conditions as the input data for our model

	S_H, MPa	S_h, MPa	S_v, MPa
Normal faulting	20	10	50
Strike-slip faulting	50	10	20
Reverse faulting	50	20	10

Here, for purposes of illustration we mainly consider the stress and stability analysis for an arbitrarily orientated borehole with an inclination angle β_1 of 40° and an azimuth α_1 of 0° drilled in a vertical transversely isotropic (VTI) formation (*i.e.*, one in which the rotational axis of symmetry is vertical). The mud pressure is 10 MPa. α_2 and β_2 are assumed to be zero. These conditions do not belong to any of the four special cases of anisotropy mentioned by *Amadei* (1983), as such, the expressions cannot be reduced to any simpler form. To initiate the study, the boundary conditions and material properties were assumed and summarized in Tables 4.1 and 4.2, respectively, where R is the ratio between E_h and E_v indicating the degree of anisotropy. Thomsen parameters as introduced in Section 4.1 are defined as (*Thomsen, 1986*):

$$\varepsilon = \frac{C_{11} - C_{33}}{2C_{33}}$$

$$\gamma = \frac{C_{66} - C_{44}}{2C_{44}}$$

$$\delta = \frac{(C_{13}-C_{44})^2-(C_{33}-C_{44})^2}{2C_{33}(C_{33}-C_{44})} \tag{4.34}$$

Furthermore, the TI elastic constants assumed in our study strictly follow the constraints on elastic moduli (Chapter 2) stated by *Banik and Egan* (2012), *Sayers* (2013) and *Sone and Zoback* (2013), and the shear modulus, G_h is empirically defined as (*Batugin and Nirenburg*, 1972):

$$G_h = \frac{E_h E_v}{E_h + E_v + 2\nu_v E_v} \tag{4.35}$$

Table 4.2 Elastic properties for the five VTI formations

	Mechanical Properties	Thomsen Parameters	Stiffness Constants
$R_1=E_h/E_v=1$	$E_h=E_v=20$GPa $\nu_v=\nu_h=0.25$ $G_h=G_v=8$GPa	$\varepsilon = 0$ $\gamma = 0$ $\delta = 0$	$C_{11}=24$GPa $C_{44}=8$GPa
$R_2=1.25$	$E_h=25$GPa $E_v=20$GPa $\nu_v=0.25$ $\nu_h=0.27$ $G_v=8.96$GPa	$\varepsilon = 0.11$ $\gamma = 0.058$ $\delta = 0.14$	$C_{11}=32.0$GPa $C_{33}=26.4$GPa $C_{44}=8.96$GPa $C_{66}=10.0$GPa $C_{13}=11.9$GPa
$R_3=1.5$	$E_h=30$GPa $E_v=20$GPa $\nu_v=0.25$ $\nu_h=0.27$ $G_v=9.87$GPa	$\varepsilon = 0.21$ $\gamma = 0.11$ $\delta = 0.28$	$C_{11}=40.2$GPa $C_{33}=28.2$GPa $C_{44}=9.87$GPa $C_{66}=12.0$GPa $C_{13}=15.2$GPa
$R_4=2$	$E_h=40$GPa $E_v=20$GPa $\nu_v=0.25$ $\nu_h=0.27$ $G_v=11.3$GPa	$\varepsilon = 0.41$ $\gamma = 0.21$ $\delta = 0.54$	$C_{11}=59.6$GPa $C_{33}=32.7$GPa $C_{44}=11.3$GPa $C_{66}=16.0$GPa $C_{13}=23.6$GPa
$R_5=2.5$	$E_h=50$GPa $E_v=20$GPa $\nu_v=0.25$ $\nu_h=0.27$ $G_v=12.4$GPa	$\varepsilon = 0.59$ $\gamma = 0.30$ $\delta = 0.75$	$C_{11}=84.9$GPa $C_{33}=38.9$GPa $C_{44}=12.4$GPa $C_{66}=20.0$GPa $C_{13}=35.0$GPa

4.6.2 Results and Discussions

To better divide the stress distributions into different quadrants and visualize them, we assume the azimuth of the borehole is zero. This is actually not that important for a horizontally lying vertical transversely isotropic medium (again whose axis of symmetry is vertical) as the properties will not vary with azimuth. And we only consider the normal faulting environment in this model (Table 4.1). The stress magnitudes shown are normalized with respect to the vertical stress, S_v, in order to make the results independent of depth. Note that the color scaling is not the same among each panel. Figure 4.3 summarizes the stress concentrations around a circular

borehole in the isotropic formation. The minimum principal stress is directly related to the tensile failure, as explained earlier. To study the manner in which condition the shear failure will be initiated, we adopt the Tresca criterion. This criterion shows that the rock will yield when it reaches the maximum shear stress, τ_m, which can be written as (*Fjaer et al.*, 2008):

$$\tau_m = \frac{1}{2}(\sigma_1 - \sigma_3) \tag{4.36}$$

where σ_1 is the maximum principal stress, and σ_3 is the minimum principal stress. Although the Tresca criterion does not take the intermediate principal stress σ_2 into consideration, some criteria, such as the modified Lade criterion and the *von Mises criterion* do depend on the intermediate principal stress (*Fjaer et al.*, 2008; *Yi et al.*, 2005). On the other hand, based on the Mohr-Coulomb criteria, shear failure cannot be solely determined from the difference between the maximum principal stress and the minimum principal stress. As described in Chapter 2, knowing the magnitude of the minimum principal stress (for the position of the Mohr circle) and rock elastic properties (for the failure envelope) are also necessary in this case.

During the progress of building our models, one limitation of the L-A solution caused by the affine transformation was revealed. For some TI materials, the corresponding μ_i are not always purely imaginary leading to some unreasonable values in the derivatives of the analytic function $\phi_i'(z_i)$ after affine transformation. Hence, to eliminate these erroneous values, we shifted them back to the correct positions based on the symmetry of $\phi_i'(z_i)$.

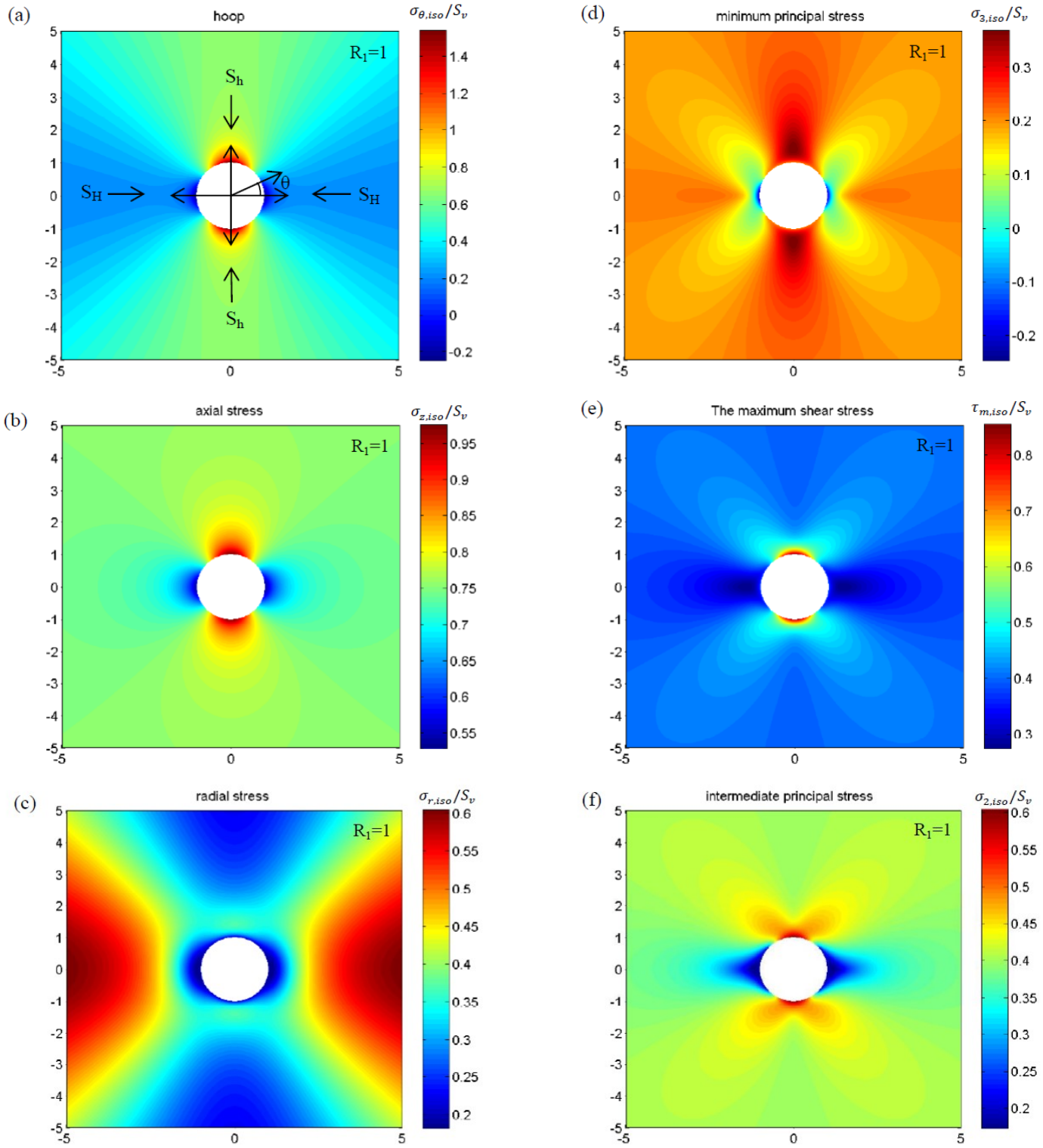

Figure 4.3 Illustration of the distributions of (a) the hoop stress, (b) the axial stress, (c) the radial stress (d) the minimum principal stress, (e) the maximum shear stress, and (f) the intermediate stress around a circular borehole wall (β=40°, α=0°) in the isotropic formation (R_1=1) in the normal faulting stress regime as indicated in Table 4.1. The directions of the far field stresses are indicated as arrows, and it will be the same case for Fig.4.4, 4.5 and 4.6. The stress magnitudes shown here are normalized by the magnitude of Sv. θ is the borehole azimuthal angle.

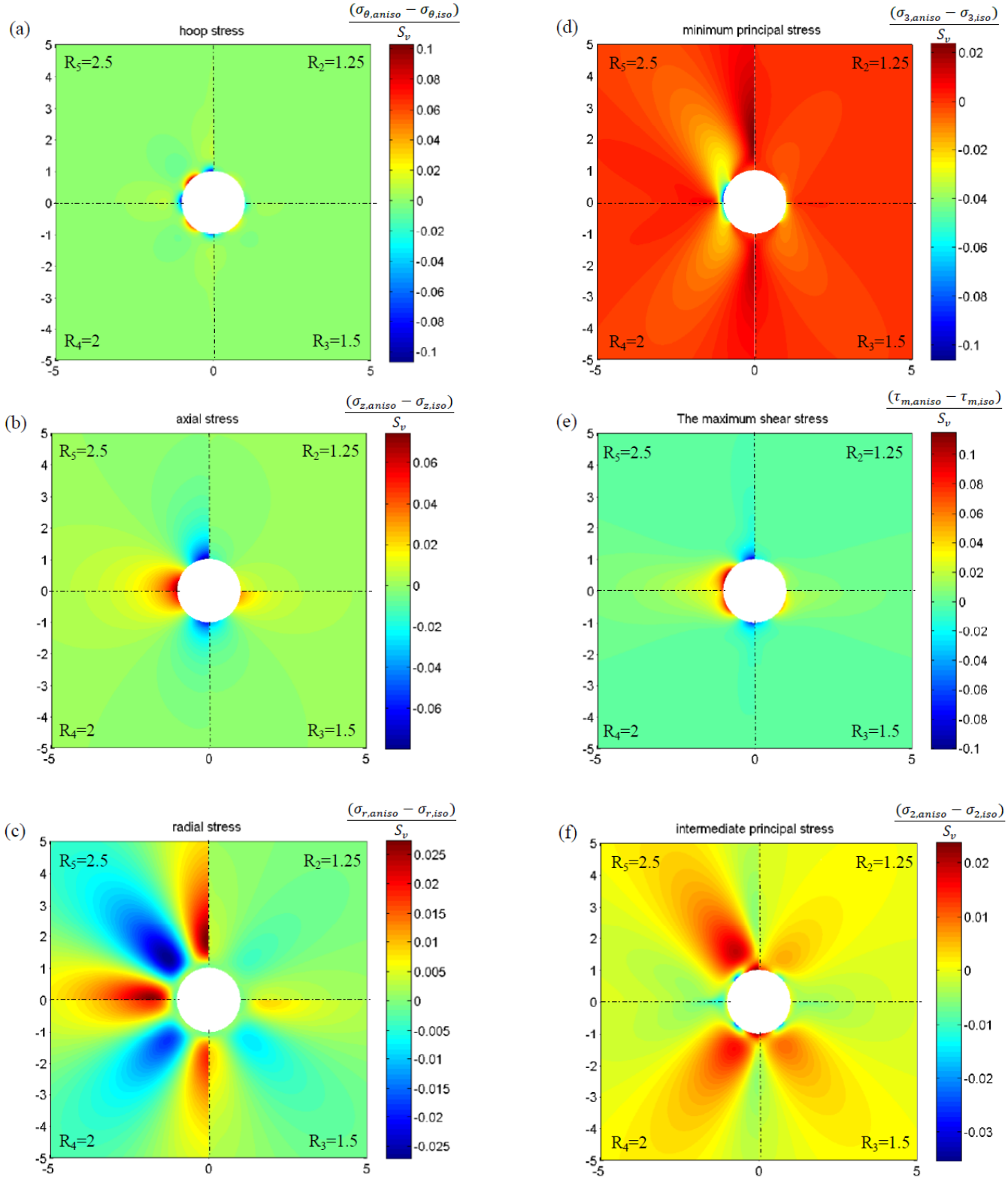

Figure 4.4 The differences of (a) the hoop stress, (b) the axial stress and (c) the radial stress (d) the minimum principal stress, (e) the maximum shear stress, and (f) the intermediate principal stress distributions around a circular borehole (β=40°, α=0°) in the normal faulting environment in anisotropic formations (upper right: R_2 = 1.25; lower right: R_3 = 1.5; lower left: R_4 = 2; upper left: R_5 = 2.5). The stress magnitudes shown are all subtracted by the magnitudes in the isotropic case and normalized with respect to the magnitude of Sv.

In Fig. 4.3, the "hot" colors (red and yellow) indicate regions under compression; whereas, the "cold" colors (blue) indicate less compressional or even pure tension if negative values. The stresses here are calculated based on the closed-form expressions derived by *Amadei* (1983), and the results are the same as those from *Hiramatsu and Oka* (1962) for the isotropic case, thus, it conforms *Amadei*'s (1983) anisotropic solution can reduces to the isotropic solution of *Hiramatsu and Oka* (1962). Moreover, the figure illustrates that the maximum compression is generated in the direction of S_H on the borehole wall and that is where the tensile failure tends to initiate. For the intermediate principal stress, the maximum value, $0.6S_v$, occurs in the direction of S_h, and the minimum value, $0.2S_v$, occurs in the direction of S_H.

Figure 4.4 show the variations in terms of stress magnitudes as for increasing degrees of anisotropy in the normal faulting stress regime. Fig. 4.3 is shown in terms of normalized absolute stresses. In Fig. 4.4, however, we wish to highlight the differences in stress concentrations using the isotropic case of Fig. 4.3 as a reference. In order to evaluate how much the anisotropy affects the stress concentrations, the colors scales in Fig. 4.4 instead indicate the difference in stress magnitudes calculated as:

$$\sigma_{diff} = \frac{(\sigma_{aniso} - \sigma_{iso})}{S_v} \tag{4.37}$$

where σ_{aniso} and σ_{iso} are the stress magnitudes in the anisotropic case and the isotropic case, respectively. Positive values ("hot" colors) indicate net compression, whereas negative values ("cold" colors) indicate net tensional stress relative to the corresponding isotropic case. Each panel is divided into four quadrants with different $R = E_h/E_v$ values. The upper right representing the case where R_2=1.25, the lower right representing the case where R_3=1.5, the lower left representing the case where R_4=2, and the upper left representing the case where R_5=2.5 (Table 4.2).

The results of sensitivity analysis in Fig. 4.4 (left panel) imply that the hoop stress is influenced the most by the rock anisotropy, with variations up to $\pm 0.1S_v$. If we look along a specific borehole azimuthal angle, θ (indicated in Fig. 4.3a), the changes in stress are not monotonic and the maximum change occurs at the borehole wall. On the other hand, the change of radial stress is the least, which reaches its maxima to $\pm 0.025S_v$ as the radius increases to about a quarter of the borehole diameter, and then the effects of anisotropy gradually fade out. For the axial stress, the variation is monotonic along the radius, and the stress tends to be averaged by up to $0.06S_v$.

All in all, the variations in the magnitude of stresses relative to the corresponding isotropic case increase with increasing degrees of anisotropy.

Fig. 4.4d illustrates that the tensile stress in the direction of S_H (θ=0° and 180°) increases by about half of its original tension for the case where R_5=2.5, whereas the points in compression (i.e., θ=90° and 270°) for the isotropic case become more compressive in the VTI formations. This implies that TI media enhances the possibility of tensile fracturing in a normal faulting stress regime. On the other hand, Fig. 4.4e shows that TI reduces the compressive stress at θ=90° and 270° at points of the largest compression, but enhances the compressional stress at θ=0° and 180°. Therefore, combining with the stress change in the minimum principal stress, we can conclude that in a normal faulting stress regime TI formations suppress the likelihood of shear failure on the borehole wall in the direction of S_h, but increase the chance of shear failure in the direction of S_H for certain borehole orientations. The variation in the intermediate principal stress (Fig. 4.4f) is more complex, but the general trends are the least compressive stress, which is in the direction of S_H, turns out to be more tensile, and the most compressive stress aligned with S_h becomes more compressive.

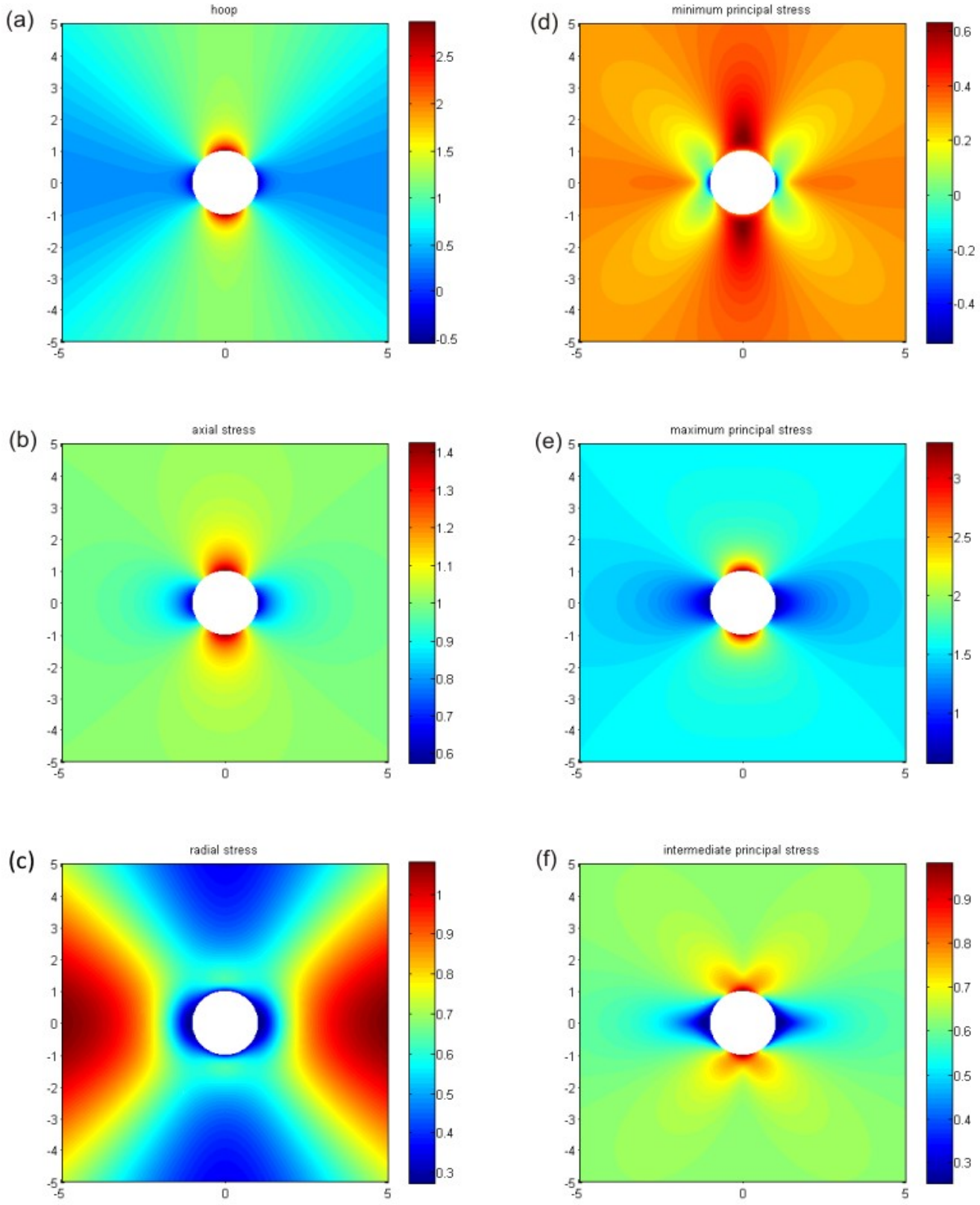

Fig. 4.5 Illustration of the distributions of (a) the hoop stress, (b) the axial stress, (c) the radial stress (e) the minimum principal stress, (f) the maximum shear stress, and (g) the intermediate stress around a circular borehole wall (β=40°, α=0°) in the isotropic formation (R_1=1) in the strike-slip faulting stress regime as indicated in Table 4.1. The stress magnitudes shown here are normalized by the magnitude of Sv.

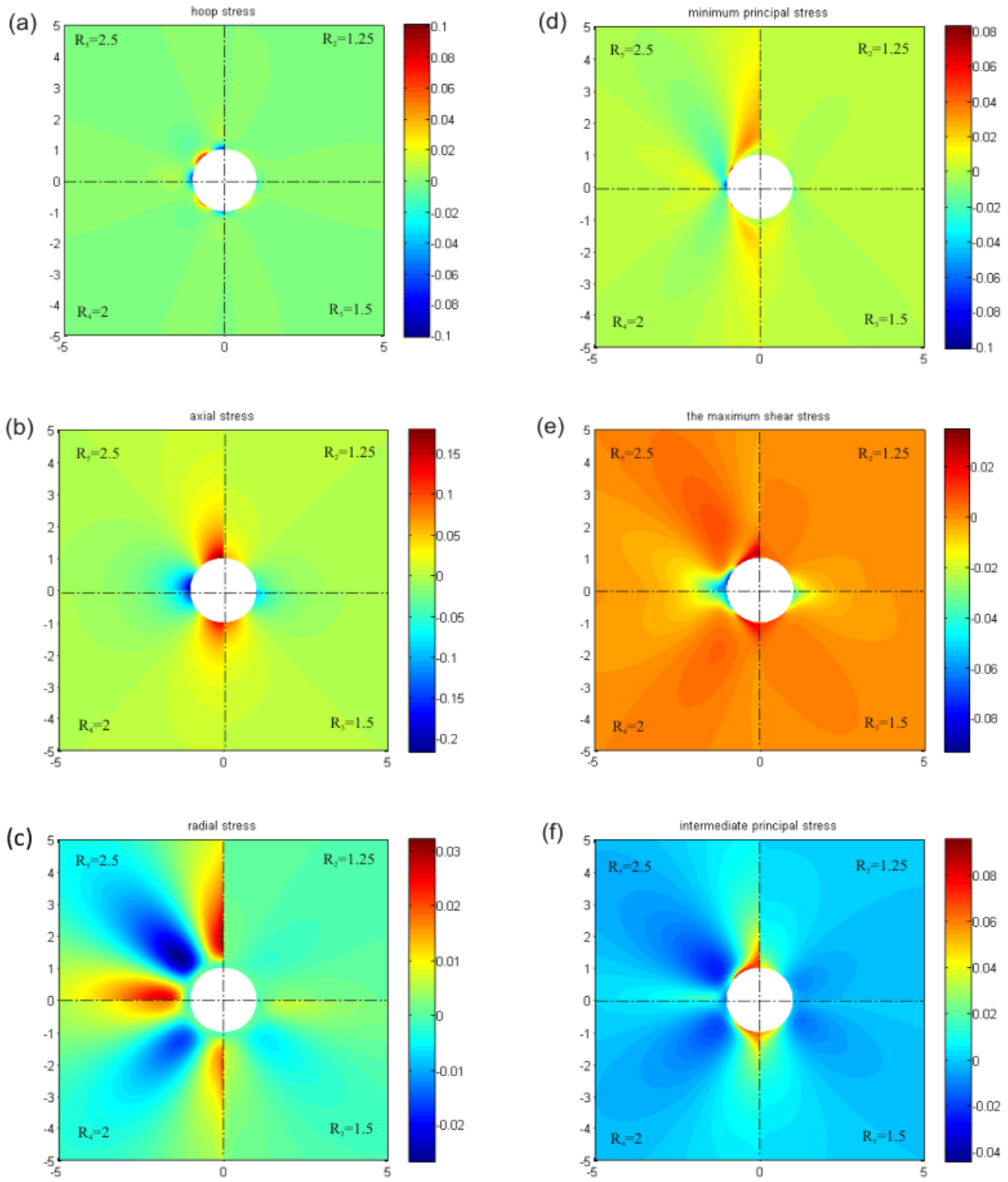

Fig. 4.6 The differences of (a) the hoop stress, (b) the axial stress and (c) the radial stress (d) the minimum principal stress, (e) the maximum shear stress, and (f) the intermediate principal stress distributions around a circular borehole (β=40°, α=0°) in the strike-slip faulting regime in anisotropic formations (upper right: R_2 = 1.25; lower right: R_3 = 1.5; lower left: R_4 = 2; upper left: R_5 = 2.5). The stress magnitudes shown are all subtracted by the magnitudes in the isotropic case and normalized with respect to the magnitude of Sv.

In the strike-slip faulting environment, borehole stresses are shown in Fig. 4.5. Comparing to those in the normal faulting environment, it seems that stress patterns is not changing that much, but stress gradients become larger due to a higher stress anisotropy in the horizontal direction. Based on Fig. 4.5d, the minimum magnitude of the minimum principal stress is smaller than that in the normal stress regime; hence, we can refer that tensile fractures are more likely to be generated in this case. However, the maximum shear stress, τ_m, is significantly larger than that in the normal faulting environment, so it is easier to initiate shear failure.

The results of parametric study in Fig. 4.6 illustrate the variation of borehole stress as a function of formation anisotropy. The changes in the hoop stress and the radial stress are not significant comparing to that in the normal stress regime. Axial stress is affected the most by formation anisotropy with its variations up to $\pm 0.2S_v$, and the change in terms of magnitudes is completely opposite compared to the case in the normal stress regime.

The impacts of formation anisotropy on three principal stresses become more complex. For the minimum principal stress, the tendency for tensile fractures initiation is increasing as the degree of anisotropy increases. On the contrary, the stress nearly does not change on the borehole wall at the azimuth of 0°. The TI formation increases the magnitude of maximum shear stress up to $0.02S_v$ at the θ=0° and 180°, and combining the change in minimum principal stress, we can conclude that the possibility of shear failure initiation is enhanced in the strike-slip environment.

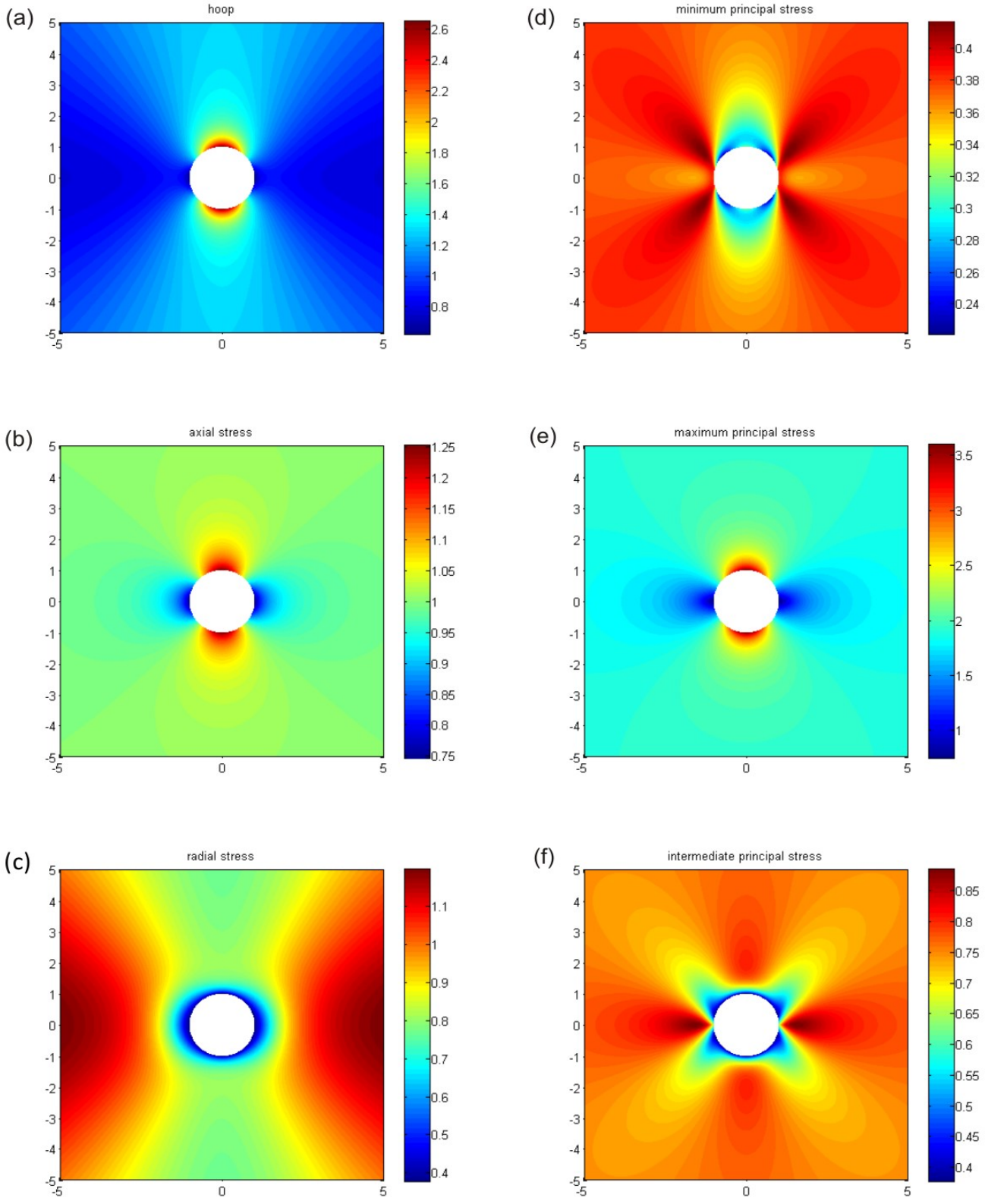

Fig. 4.7 Illustration of the distributions of (a) the hoop stress, (b) the axial stress, (c) the radial stress (e) the minimum principal stress, (f) the maximum shear stress, and (g) the intermediate stress around a circular borehole wall (β=40°, α=0°) in the isotropic formation (R_1=1) in the thrust faulting environment as indicated in Table 4.1. The stress magnitudes shown here are normalized by the magnitude of Sv.

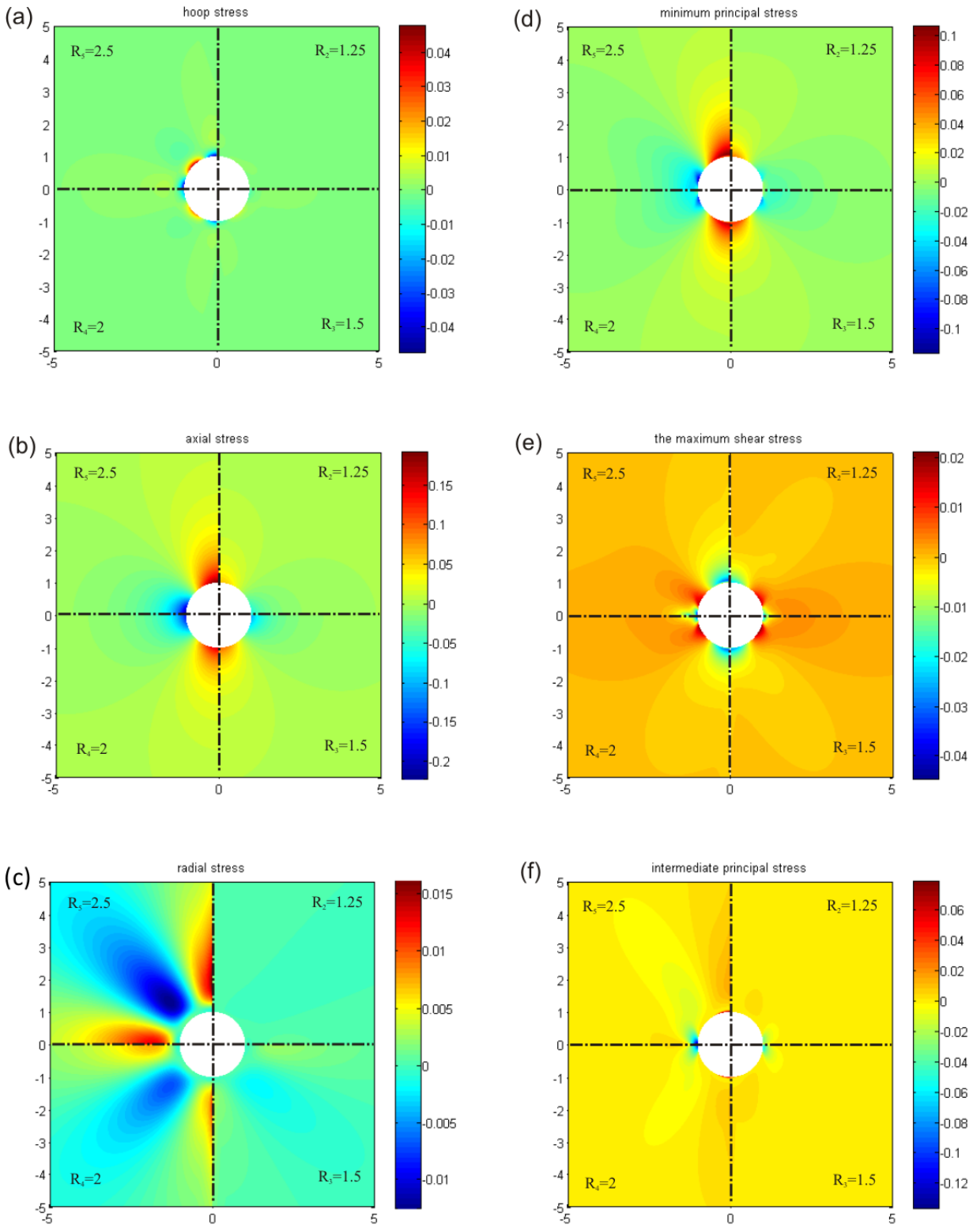

Fig. 4.8 The differences of (a) the hoop stress, (b) the axial stress and (c) the radial stress (d) the minimum principal stress, (e) the maximum shear stress, and (f) the intermediate principal stress distributions around a circular borehole (β=40°, α=0°) in the reverse faulting regime in anisotropic formations (upper right: R_2 = 1.25; lower right: R_3 = 1.5; lower left: R_4 = 2; upper left: R_5 = 2.5). The stress magnitudes shown are all subtracted by the magnitudes in the isotropic case and normalized with respect to the magnitude of Sv.

Figure 4.7 shows the stress concentrations around a borehole wall in a TI formation in the reverse faulting environment. With the higher stress anisotropy, the stress gradients in this case are still higher than those in the normal faulting environment, especially for the maximum shear stress. But the possibility for tensile fracture initiation is zero since the smallest magnitude of the minimum principal stress is larger than the rock tensile strength (Fig. 4.7d). An interesting phenomenon is the maximum tension is not at θ=90° and 270°, instead, it is at the angle of 0° and 180° with a short distance from the borehole wall.

In terms of the variations of stress magnitude as a function of formation anisotropy, as shown in Fig. 4.8, the patterns of changes are almost the same as those in the strike-slip environment for the hoop, axial and radial stresses. However, for the three principal stresses, the changes are quite complicated. For the shear failure, at θ=0° and 180°, the minimum principal stress increases and the maximum shear stress decreases as an effect of formation anisotropy, which means that the tendency for shear failure is smaller.

4.7 Summary

The purpose of this chapter aims to investigate the effects of formation anisotropy on the stress distributions in the borehole vicinity. Firstly, we revisited the L-A solution for borehole stress calculations in a homogeneous anisotropic medium, and achieved the final expressions. Second, by utilizing this solution, a theoretical model has been successfully implemented in conducting sensitivity studies. The results indicate that:

- The L-A solution reduces to the Hiramatsu and Oka isotropic case.
- In the normal faulting environment, VTI formations enhance the likelihood of tensile failure, but reduce the possibility of shear failure in the direction of S_h in the case discussed in this chapter.
- In the strike-slip faulting environment, the tendencies for both tensile fracture initiation and breakout initiation increase in VTI formations.
- In the reverse faulting environment, VTI formations increase the possibility for tensile fracture initiations and reduce the possibility for shear failure.

- Tensile fractures are more likely to occur in the strike-slip stress regime and less likely to occur in the reverse stress regime.

This chapter provides a building block for the work in next chapter, which focuses more on the consequential creation of drilling-induced tensile fractures.

4.8 References

Aadnoy, B. (1987), Continuum mehcnaics analysis of the stability of inclined boreholes in anisotropic rock formations, PhD Thesis, University of Trondheim, Norway.

Aadnoy, B., and S. Bernt (1988), Modeling of the stability of highly inclined boreholes in anisotropic rock formations (includes associated papers 19213 and 19886), *SPE Drill Engineering*, *3*(03), 259-268.

Amadei, B. (1983), *Rock anisotrpy and the theory of stress measurements*, Springer-Verlag, Berlin.

Banik, N. C., and M. S. Egan (2012), Effects of VTI anisotropy on shale reservoir characterization, SPE Middle East Unconventional Gas Conference and Exhibition, Society of Petroleum Engineers, Abu Dhabi, UAE, 23-25 Janurary.

Batugin, S. A., and R. K. Nirenburg (1972), Approximate relation between the elastic constants of anisotropic rocks and the anisotropy parameters, *Soviet Mining Science*, *8*(1), 5-9.

Cholach, P. Y., and D. R. Schmitt (2006), Intrinsic elasticity of a textured transversely isotropic muscovite aggregate: Comparisons to the seismic anisotropy of schists and shales, *Journal of Geophysical Research: Solid Earth*, *111*(B9), B09410.

Dewhurst, D. N., and A. F. Siggins (2006), Impact of fabric, microcracks and stress field on shale anisotropy, *Geophys J Int*, *165*(1), 135-148.

Fjaer, E., R. M. Holt, P. Horsrud, A. M. Raaen, and R. Risnes (2008), *Petroleum related rock mechanics*, Elsevier, Amsterdam, the Netherlands.

Gaede, O., F. Karpfinger, J. Jocker, and R. Prioul (2012), Comparison between analytical and 3D finite element solutions for borehole stresses in anisotropic elastic rock, *International Journal of Rock Mechanics and Mining Sciences*, *51*(0), 53-63.

Gazaniol, D., T. Forsans, M. J. F. Boisson, and J. M. Piau (1995), Wellbore Failure Mechanisms in Shales: Prediction and Prevention, *J. Pet. Eng.*, 589-595.

Hiramatsu, Y., and Y. Oka (1962), Stress around a shaft or level excavated in ground with a three-dimensional stress state., *Mem. Fac. Eng*, *24*(Kyoto Univ.), 56-76.

Hornby, B. (1995), The Elastic Properties of Shales, PhD Thesis Thesis, University of Cambridge.

Jia, Q., and D. R. Schmitt (2014), Effects of formation anisotropy on borehole stress concentrations: implications to drilling induced tensile fractures, 48th US Rock Mechanics / Geomechanics Symposium, American Rock Mechanics Association, Minneapolis, MN, USA, June 1-4.

Johnston, J. E., and N. I. Christensen (1992), Shear wave reflectivity, anisotropies, Poisson's ratios, and densities of a southern Appalachian Paleozoic sedimentary sequence, *Tectonophysics*, *210*(1–2), 1-20.

Kaarsberg, E. A. (1959), Introductory studies of natural and artificial argillaceous aggregates by sound-propagation and X-ray diffraction methods, *The Journal of Geology*, *67*(4), 447-472.

Lekhnitskii, S. G. (1981), *Theory of elasticity of an anisotropic body*, Mir Publications, Moscow.

Melendez, J., and D. R. Schmitt (2011), Investigating anisotropy in rocks by using pulse transmission method, *CSEG Recorder*, *36*(10), 38-42.

Melendez, J., and D. R. Schmitt (2013), Anisotropic elastic moduli of carbonates and evaporites from the Weyburn-Midale reservoir and seal rocks, *Geophys Prospect*, *61*(2), 363-379.

Ong (1994), Borehole stability, 344 pp, U. of Oklahoma, Norman, Oklahoma.

Ong, and J. C. Roegiers (1993), Influence of anisotropies in borehole stability, *Int J Rock Mech Min*, *30*(7), 1069-1075.

Ong, and J. C. Roegiers (1995), Fracture initiation from inclined wellbores in anisotropic formations, Society of Petroleum Engineers, SPE-29993-MS, Beijing, China, 14-17 November.

Sarout, J., and Y. Gueguen (2008), Anisotropy of elastic wave velocities in deformed shales: Part 1-Experimental results, *Geophysics*, *73*(5), D75-D89.

Sayers, C. M. (2013), The effect of anisotropy on the Young's moduli and Poisson's ratios of shales, *Geophys Prospect*, *61*(2), 416-426.

Sone, H., and M. D. Zoback (2013), Mechanical properties of shale-gas reservoir rocks - Part 1: Static and dynamic elastic properties and anisotropy, *Geophysics*, *78*(5), D378-D389.

Thomsen, L. (1986), Weak elastic anisotropy, *Geophysics*, *51*(10), 1954-1966.

Vahid, S., and G. Ahmad (2011), Hydraulic fracture initiation from a wellbore in transversely isotropic rock, 45th US Rock Mechanics/Geomechanics Symposim, American Rock Mechanics Association, 2011/1/1/.

Vernik, L., and A. Nur (1992), Ultrasonic Velocity and Anisotropy of Hydrocarbon Source Rocks, *Geophysics*, *57*(5), 727-735.

Vernik, L., and X. Z. Liu (1997), Velocity anisotropy in shales: A petrophysical study, *Geophysics*, *62*(2), 521-532.

Walsh, J. J., B. K. Sinha, T. J. Plona, D. E. Miller, and M. Ammerman (2008), Derivation of anisotropy parameters in a shale using borehole sonic data, SEG Technical Program Expanded Abstracts, American Rock Mechanics Association, 26, 1.

Wilson, R. C., and D. N. Willis (1986), Successful high angle drilling in the Statfjord Field, SPE Annual Technical Conference and Exhibition, Society of Petroleum Engineers, SPE-15465-MS, New Orleans, Louisiana, 5-8 October.

Wong, R. C. K., D. R. Schmitt, D. Collis, and R. Gautam (2008), Inherent transversely isotropic elastic parameters of over-consolidated shale measured by ultrasonic waves and their comparison with static and acoustic in situ log measurements, *Journal of Geophysics and Engineering*, *5*(1), 103-117.

Yi, X., S. H. Ong, and J. E. Russell (2005), Improving borehole stability analysis by quantifying the effects of intermediate principal stress using polyaxial rock strength test data, Alaska Rocks 2005, The 40th U.S. Symposium on Rock Mechanics (USRMS), American Rock Mechanics Association, Anchorage, Alaska, 25-29 June.

Chapter 5

Borehole Tensile Fracture Tracing

5.1 Introduction

As mentioned in Chapter 3, the stresses can damage the formation in the borehole vicinity by either compressive failure caused by compression or tensile failure caused by tension, and consequently, generating borehole breakouts and drilling-induced tensile fractures (DITF) in a predictable manner. The onset of compressive failure can be defined by various kinds of criteria, among which the most prevalent and the simplest one is the Mohr-Coulomb criterion, as thoroughly stated and utilized (*Fjaer et al.*, 2008; *Peska and Zoback*, 1995). Moreover, conditions required to initiate tensile fractures have been investigated by (*Ong and Roegiers*, 1995; *Peska and Zoback*, 1995; *Prioul et al.*, 2011), and tensile fracture propagation has been probed both analytically (*Aadnoy*, 1990; *Brudy and Zoback*, 1993; *Ong*, 1994; *Ong and Roegiers*, 1995) and numerically (*Paluszny and Zimmerman*, 2011; *Wang et al.*, 2012). Additionally, based on the relationship between the orientations of tensile fractures and *in-situ* stresses, a number of researchers (*Aadnoy and Bell*, 1998; *Barton et al.*, 1997; *Brudy and Zoback*, 1999; *Davatzes and Hickman*, 2010; *Peska and Zoback*, 1995; *Schmitt et al.*, 2012) have studied methods of constraining the orientation of maximum horizontal principal stresses using tensile fractures observed in image logs.

In this chapter, we first derive the solution for stress components at the borehole wall, which is coded into the tracing program, and the MATLAB^{TM} program itself is provided in Appendix C. Then, Ong's borehole stability design code (*Ong*, 1994; *Ong and Roegiers*, 1995) is adopted to visualize tensile fracture trajectories on the unwrapped borehole wall in a homogeneous transversely isotropic medium. A variety of sensitivity studies are carried out in order to investigate the influence of rock anisotropy and *in-situ* stresses on DITF trajectories.

5.2 Stresses at the Borehole Wall

Drilling-induced tensile fractures are less likely to propagate into the formations during drilling processes; therefore, to simplify the problem, only stresses at the borehole wall will be analyzed. To change the system into the polar coordinate, z_i can be written as (*Ong*, 1994):

$$z_i = a(\cos\theta + \mu_i \sin\theta) \tag{5.1}$$

where a is the radius of the borehole. Based on Eq. 5.1, we can get:

$$\sqrt{\left(\frac{z_i}{a}\right)^2 - 1 - \mu_i^2} = i(sin\theta - \mu_i cos\theta) \tag{5.2}$$

And the function inverse is:

$$\zeta_i = e^{i\theta} \tag{5.3}$$

Then the derivatives of the analytic functions at the borehole wall becomes (*Ong*, 1994):

$$\Phi_1'(z_1) = \frac{1}{2\Delta(\mu_1\cos\theta - \sin\theta)}[D'(\lambda_2\lambda_3 - 1) + E'(\mu_2 - \lambda_2\lambda_3\mu_3) + F'\lambda_3(\mu_3 - \mu_2)]$$

$$\Phi_2'(z_2) = \frac{1}{2\Delta(\mu_2\cos\theta - \sin\theta)}[D'(1 - \lambda_1\lambda_3) + E'(\lambda_1\lambda_3\mu_3 - \mu_1) + F'\lambda_3(\mu_1 - \mu_3)]$$

$$\Phi_3'(z_3) = \frac{1}{2\Delta(\mu_3\cos\theta - \sin\theta)}[D'(\lambda_1 - \lambda_2) + E'(\mu_1\lambda_2 - \mu_2\lambda_1) + F'(\mu_2 - \mu_1)] \tag{5.4}$$

where,

$$D' = (P_w - \sigma_{x0})cos\theta - \tau_{xy0}sin\theta - i\left[(P_w - \sigma_{x0})sin\theta + \tau_{xy0}cos\theta\right]$$

$$E' = -\left(P_w - \sigma_{y0}\right)sin\theta + \tau_{xy0}cos\theta - i\left[\left(P_w - \sigma_{y0}\right)cos\theta + \tau_{xy0}sin\theta\right]$$

$$F' = -\tau_{xz0}cos\theta - \tau_{yz0}sin\theta - i\left(\tau_{yz0}cos\theta - \tau_{xz0}sin\theta\right) \tag{5.5}$$

Inserting Eq. 5.5 into Eq. 4.22, the analytical solution for borehole wall stresses is derived. This solution will be utilized in the later tracing design code.

5.3 Tensile Fracture Tracing Code Development

Recalling the borehole failure mechanism in Chapter 3, tensile failure is assumed to occur when the least effective principal stress σ_3' exceeds the tensile strength of the formation, which can be written in the following mathematical form (*Fjaer et al.*, 2008; *Ong*, 1994):

$$\sigma_3' = -T_0 \tag{5.6}$$

where the prime indicates the effective stress, and

$$\sigma_3' = \frac{\sigma_\theta' + \sigma_z'}{2} - \frac{1}{2}\sqrt{\left(\sigma_\theta' - \sigma_z'\right)^2 + 4\tau_{\theta z}^2} \tag{5.7}$$

where σ_θ', σ_z' and $\tau_{\theta z}$ are the effective hoop stress, the effective axial stress and the shear stress, respectively. Since DITF tends to grow normal to the orientation of σ_3', when the borehole axis is aligned with the principal stresses, the axial tensile fractures appear to be in pairs, 180° apart from each other on the unwrapped borehole walls, and parallel to the wellbore axis. Conversely, when the borehole is inclined with respect to the principal stresses, DITF are oblique, also called *en echelon* fractures, and its orientation is defined by an angle, ω, calculated as:

$$\omega = \frac{1}{2} arctan \frac{2\tau_{\theta z}}{\sigma_{\theta\theta} - \sigma_{zz}} \tag{5.8}$$

As *Ong* (1994) mentioned, in order to specify the quadrant for the angle, it is critical to know the signs of the numerator and denominator when dealing with the arc-tangent of the quotient. Therefore, the MATLAB™ build-in function atan2(a_1,a_2) is used in our fracture tracing model. A 0° or 180° of γ means that fractures are in planes perpendicular to the axis, and a 90° means that fractures are in planes parallel to the borehole axis.

In this model, the algorithm for tensile fracture tracing is built based on the approach developed by (*Li and Schmitt*, 1998; *Zhang*, 2011). Fig. 5.1 summarizes the overall process for tensile fracture tracing in the MATLAB™ code. The mesh is designed with 200×200 nodes distributed regularly on the unwrapped borehole wall. The spacings between nodes in both x and y direction have a dimension of about 0.016 of the borehole diameter. Since the stress does not change along certain azimuth θ, each column can be treated as a "straw" (line 1 to 6 in Fig. 5.1). After the formation properties defined and the boundary conditions applied, the program determines whether the stress condition meets the requirement of tensile fracturing (Eq. 5.6), and the next

step is to search for the least minimum principal stress within the mesh where the tensile fracture is assumed to initiate (node A). In this case, the material is assumed to have no tensile strength.

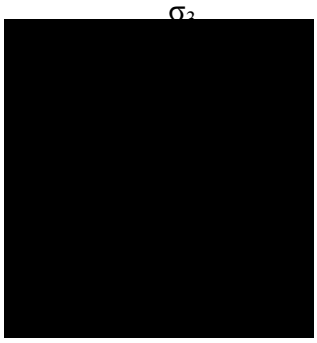

Figure 5.1 Illustration of tensile fracture tracing method.

For simplicity, each straw is only allowed to have maximum one tensile fracture initiated, but in the realistic case, a series of *en echelon* tensile fractures can be produced. The fracture propagates outward from node A perpendicular to the direction of σ_3 until it intersects straw 4. At the point of intersection (B), the stress tensor is recalculated and the fracture extends if the condition is suitable. The above procedures repeat to continuously propagate the fracture over a span of the borehole wall, θ_t, until σ_3 becomes compressive. The length of the fracture in the vertical direction is denoted as l_t.

As mentioned by *Zhang* (2011),there are some drawbacks of this model. First, this is a static model without any consideration of the kinetic energy generated by the creations of tensile crack. Second, this model ignores the disturbance on the stress distribution by the creations of tensile fractures. Although these flaws set up the goal for our future study, this model still obeys the essential physics and provides a valid approach for tensile fracture tracing.

5.4 The Effects of the Far-field Stress and the Degree of Formation Anisotropy on Tensile Fracture Trajectory

Parametric studies are carried out to investigate the effects of the far-field stresses and VTI formations on the tensile fracture creation, as summarized in Fig. 5.2. In this case, the orientation of the borehole is fixed (β_1=40°, α_1=45°). The reason that a 40 degree borehole inclination angle is chosen is because, for a vertical or a horizontal borehole in a common *in-situ* stress condition, DITFs are always in planes parallel to the borehole axis, so that the stress regime cannot be

distinguished based on the DITF trajectory (*Aadnoy*, 1990). Note that the borehole azimuth α_1 in this case does not equal to 0°, and this is to avoid having fractures plotted on the right or left edge of the figure for better illustrations. Three stress regimes are considered as indicated in Table 4.1, and for the material properties, two cases: R_1 and R_3, are taken into account (Table 4.2). The green lines show the trajectories of the tensile fracture and the arrows represent the directions of propagation. The background colors illustrate the magnitudes of minimum principal stress which are normalized with respect to S_v. The locations corresponding to the bottom and top of the borehole are also shown.

As shown in Fig. 5.2, tensile fractures appeared to be curved and asymmetrical; this is because ω varies asymmetrically over the wellbore circumference. The fracture starts nearly vertically but extends away from the borehole axis on one side, and in this case, if ω varies slowly, l_t will be larger. However, on the other side, the fracture starts tilted but approaches the vertical direction as it extends; in this case, l_t will be larger with a rapidly changing ω. Furthermore, the spans θ_t for the two fractures in a pair are not the same. *Zoback* (2007), for example, has also mentioned the similar appearance of tensile fracture called *fish-hook* or *J-fractures*.

For the isotropic case, l_t are the longest especially for the one on the left side in the strike-slip faulting environment, whereas it is the opposite case in the reverse faulting environment. In the normal faulting environment and the strike-slip faulting environment, tensile fractures are more likely to occur in the VTI formation compared to the isotropic cases. On the other hand, in the reverse faulting stress regime, the influence of the VTI formation on the initiations of tensile fractures is the reversed. Regarding to the effects of the VTI formation on the length of tensile fractures, l_t tends to be lengthened under normal faulting conditions and to be shortened under strike-slip faulting and reverse faulting conditions.

Other than conducting sensitivity studies, this theoretical model can also help us constrain the *in-situ* stress condition incorporating with the drilling-induced fractures observed in borehole images (*Schmitt et al.*, 2012; *Zoback*, 2007). The observations provide the locations where fractures initiate, the spans of fractures (θ_t) and the deviations of fractures from borehole axis (ω), thus constraining the modeling.

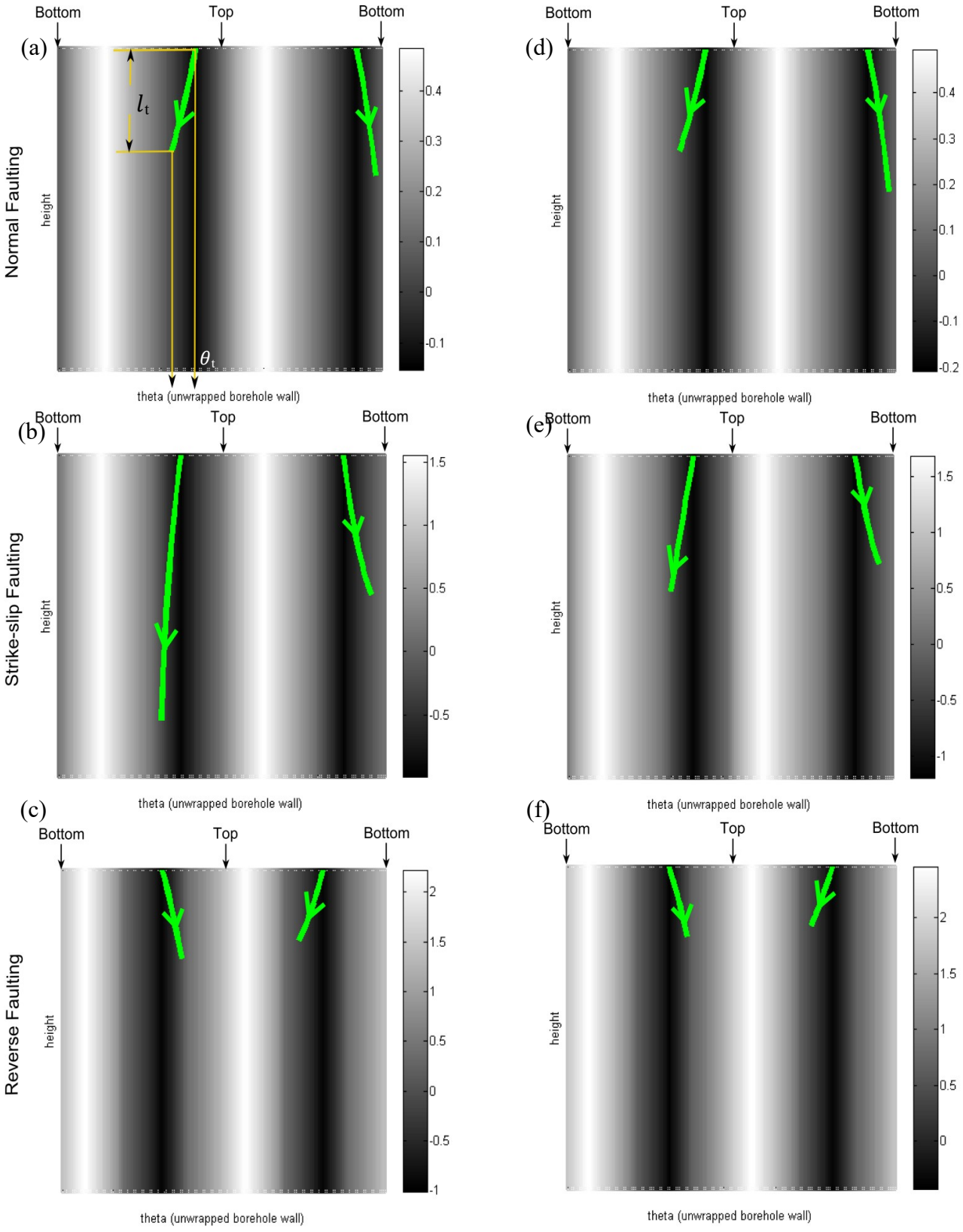
(a)
Bottom
Top
Bottom
Normal Faulting
height
l_t
θ_t
theta (unwrapped borehole wall)
0.4
0.3
0.2
0.1
0
-0.1
(d)
Bottom
Top
Bottom
height
theta (unwrapped borehole wall)
0.4
0.3
0.2
0.1
0
-0.1
-0.2
(b)
Bottom
Top
Bottom
Strike-slip Faulting
height
theta (unwrapped borehole wall)
1.5
1
0.5
0
-0.5
(e)
Bottom
Top
Bottom
height
theta (unwrapped borehole wall)
1.5
1
0.5
0
-0.5
-1
(c)
Bottom
Top
Bottom
Reverse Faulting
height
theta (unwrapped borehole wall)
2
1.5
1
0.5
0
-0.5
-1
(f)
Bottom
Top
Bottom
height
theta (unwrapped borehole wall)
2
1.5
1
0.5
0

Figure 5.2 Theoretical model of the tensile fracture trajectories in normal faulting environments (a and d), strike-slip faulting environments (b and e), and reverse faulting environments (c and f); the panels in the left column corresponds to the isotropic case (R_1) and the panels in the right column corresponds to the anisotropic case (R_3) as indicated in Table 4.2. Green lines represent the tensile fracture trajectories and arrows indicate the directions of propagation. The background colors represent the magnitudes of the minimum principal stress. The bottom and top of the wellbore are also indicated. Y-axis (height) is in the same scale as that of the x-axis (θ). The borehole orientation is not chosen to be as the same as the previous model (Chapter 4) for illustration purposes (avoid to have fractures being plotted on the edge of the figure).

5.5 Summary

A tensile fracture tracing program has been coded based on the L-A model coupled with Ong's wellbore-stability design code. Parametric studies lead to the following interesting findings:

i) *En echelon* tensile fractures appear to be in asymmetrical pairs.

ii) Fracture trajectories are influenced by the formation anisotropy in terms of the spans of fractures and the fracture tracing angles.

Utilizing this model can help us constrain the state of stress incorporating with the DITF observed in image logs.

5.6 References

Aadnoy, B. (1990), In-situ stress directions from borehole fracture traces, *J Petrol Sci Eng*, *4*(2), 143-153.

Aadnoy, B. S., and J. S. Bell (1998), Classification of drilling-induced fractures and their relationship to in-situ atress directions, *The Log Analyst*, 27-42.

Barton, C. A., D. Moos, P. Peska, and M. D. Zoback (1997), Utilizing wellbore image data to determine the complete stress tensor: Application to permeability anisotropy and wellbore stability, *The Log Analyst*, *38*(06), 21-33.

Brudy, M., and M. D. Zoback (1993), Compressive and tensile failure of boreholes arbitrarily-inclined to principal stress axes: Application to the KTB boreholes, Germany, *Int J Rock Mech Min*, *30*(7), 1035-1038.

Brudy, M., and M. D. Zoback (1999), Drilling-induced tensile well-fractures: implications for determination of in-situ stress orientation and magnitude, *International Journal of Rock Mechanics and Mining Sciences*, *36*, 24.

Davatzes, N. C., and S. H. Hickman (2010), Stress, fracture, and fluid-flow analysis using acoustic and electrical image logs in hot fractured granites of the Coso Geothermal Field, California, U.S.A., in M. Poppelreiter, C. Garcia-Carballido, and M. Kraaijveld, eds., *Dipmeter and Borehole Image Log Technology: AAPG Memoir*, *92*, 34.

Fjaer, E., R. M. Holt, P. Horsrud, A. M. Raaen, and R. Risnes (2008), *Petroleum related rock mechanics*, Elsevier, Amsterdam, the Netherlands.

Li, Y., and D. R. Schmitt (1998), Drilling-induced core fractures and in situ stress, *Journal of Geophysical Research: Solid Earth*, *103*(B3), 5225-5239.

Ong (1994), Borehole stability, 344 pp, U. of Oklahoma, Norman, Oklahoma.

Ong, and J. C. Roegiers (1995), Fracture initiation from inclined wellbores in anisotropic formations, Society of Petroleum Engineers, SPE-29993-MS, Beijing, China, 14-17 November.

Paluszny, A., and R. W. Zimmerman (2011), Numerical simulation of multiple 3D fracture propagation using arbitrary meshes, *Computer Methods in Applied Mechanics and Engineering*, *200*(9–12), 953-966.

Peska, and Zoback (1995), Compressive and tensile failure of inclined well bores and determination of *in situ* stress and rock strength, *Journal of Geophysical Research-Solid Earth*, *100*(B7), 12791-12811.

Peska, P. H. S. W., and M. D. Zoback (1995), Observations of borehole breakouts and tensile wall-fractures in deviated boreholes: A technique to constrain in situ stress and rock strength, The 35th U.S. Symposium on Rock Mechanics (USRMS), American Rock Mechanics Association, ARMA-95-0319, Reno, Nevada, 5-7 June.

Prioul, R., F. Karpfinger, C. Deenadayalu, and R. Suarez-Rivera (2011), Improving fracture initiation predictions on arbitrarily oriented wells in anisotropic shales, Canadian Society for Unconventional Gas, Society of Petroleum Engineers, SPE-147462-MS, Calgary, Canada, 15-17 November.

Schmitt, D., C. Currie, and L. Zhang (2012), Crustal stress determination from boreholes and rock cores: Fundamental principles, *Tectonophysics*, *580*, 1-26.

Wang, S. Y., S. W. Sloan, C. A. Tang, and W. C. Zhu (2012), Numerical simulation of the failure mechanism of circular tunnels in transversely isotropic rock masses, *Tunnelling and Underground Space Technology*, *32*(0), 231-244.

Zhang, L. (2011), Three-dimensional numerical models of drilling induced core fractures, 276 pp, University of Alberta, Edmonton, Canada.

Zoback, M. D. (2007), *Reservoir geomechanics*, Cambridge University Press, Cambridge.

Chapter 6

Numerical Modeling for Displaying Borehole Stress Concentrations

6.1 Overview

The objectives of this part of the study are: (1) creating a 3-D static numerical model to calculate the stress concentration around a circular borehole using the commercial finite element solver named ANSYS^{TM}; and (2) developing the previous static model into a 3-D dynamic model to simulate the fracture behavior in the photoelasiticity tests. However, as this section is only in the preliminary stage, only the first step will be described in this chapter.

The analytical solutions for borehole stress calculations were introduced in Chapters 3 and 4, and they work well in terms of dealing with real problems. However, analytical solutions are usually restricted to various assumptions, such as simplified boundary conditions, regular geometries, infinitely long boreholes, and homogeneous materials. In the lab experiments, tensile fracture initiations and propagations are very complex processes so that the development of a corresponding analytical model can be significantly time-consuming or perhaps impossible. The practical way out is to generate numerical models to mimic these processes.

In this chapter, we will first describe the 3-D model in details including its basic theories, model geometry, types of element used, mesh generations, and boundary conditions (BCs). The second part is the model validation using the L-A solutions. The last part contains some suggestions for future study.

6.2 Details and Descriptions of the 3D Finite Element Model

6.2.1 Basic Theory

Finite element method (FEM) is widely used to simulate physical systems by solving partial differential equations numerically. This is a model-based process; hence, model idealization and discretization are necessary steps for the generation of a discrete model accompanying with simulation errors. Model idealization is a process that builds an idealized mathematical model in

order to abstract and predict behaviors of the corresponding actual physical system. This process needs to be accomplished by a human. Model discretization results in a more practical discrete numerical model by reducing the degrees of freedom (DOF) represented as the unknown functions of a set of nodal points. To determine simulation errors and adjust the model, the finite element (FE) model should be validated against the experimental database. Basically, the FEM calculates each part of the model separately, which is referred to as element in the following content, and then the results are obtained by building a global matrix through assembling all elements (*Chatterjee and Mukhopadhyay*, 2003).

Finite element programs of ANSYS^{TM} consist of three parts (*Zienkiewicz et al.*, 2013):

1. Pre-processor
2. Solution module
3. Post-processor

In the pre-processer module, the model geometry needs to be set followed by the mesh generation and material parameter assignation. The scale of the FEM model is restricted to the computational and manpower resources; moreover, the complexity of the model (i.e., mesh density) is determined by the requirements on the resolution and quality of the solution (*Liu and Quek*, 2003). After the mesh creation, the model area is constructed by a number of finite elements which are connected by nodal points (*Liu and Quek*, 2003). Each element has its own unique number, and is required to be positioned by the coordinate locations of its associated nodal points which are also numbered (*Liu and Quek*, 2003). The type of elements is selected based on the similarity of the element characterizations with respect to the mechanical behaviors of the original physical system and the expectations regarding to the accuracy of the results. The rules of element selections are to always pick the simplest elements that can fulfill the requirements and to try to avoid special elements unless necessary. The system of interest may contain more than one material. Each element needs to be assigned with a corresponding set of material properties. For structural solid system, the required material properties are Young's modulus and Poisson's ratio; whereas, for the thermal analysis, the thermal conductivity coefficient is a key input (*Moaveni*, 2008). In this study, the whole model domain only consists of one material which is required to be linear elastic, homogeneous and continuous.

The solution module allows the program to solve linear or nonlinear equations in order to achieve nodal results (*Moaveni*, 2008). One of the most important processes in this portion of FE programs is applying appropriate boundary conditions (BCs). For a structural problem, boundary conditions mainly include setting displacements, forces, loads, temperatures (if thermodynamic is considered) and gravity (*Moaveni*, 2008). Those can directly affect DOFs, called essential BCs, such as displacements, otherwise natural BCs, for instance external forces acting on the system. Additionally, many physical systems exhibit some conditions of symmetry. By taking advantage of such symmetries we can significantly simplify the FE model allowing only a portion of the model to be processed (*Liu and Quek*, 2003). Recognition of symmetry can reduce the DOFs, the BCs, and thus the data storage space and computational time. The determination of a system to be structurally symmetrical is based on the symmetry in geometry, support conditions, material properties and loading patterns (*Liu and Quek*, 2003). A system can also be anti-symmetrical if the loading condition is anti-symmetric.

In the post-processor module, the FEM program can record data as a text file or visualize the results graphically. The main features of visualizations include the display of the mesh, BCs, contours of the stress and displacement distribution.

As mentioned above, the FEM is a process to solve a series of partial differential equations. The governing equations for a 3-D solid FEM model include the strain-displacement relationships (Chapter 2), the constitutive equations (Chapter 2), the dynamic equilibrium equation, and the boundary conditions; and their mathematical equations are defined as (*Liu and Quek*, 2003)

Strain-displacement relationships: $\boldsymbol{\varepsilon} = \boldsymbol{L}\boldsymbol{U}$ (6.1)

The constitutive equations: $\boldsymbol{\sigma} = \boldsymbol{C}\boldsymbol{\varepsilon}$ (6.2)

The dynamic equilibrium equation: $\boldsymbol{L}^T\sigma + \boldsymbol{f}_b = \rho\ddot{\boldsymbol{U}}$ (6.3)

The displacement (essential) boundary conditions:

$$u = \overline{u} \text{ and/or } v = \overline{v} \text{ and/or } w = \overline{w} \tag{6.4}$$

The force (natural) boundary condition:

$$\boldsymbol{n\sigma} = \bar{\boldsymbol{t}} \tag{6.5}$$

where $\boldsymbol{U}$ is the displacement vector, $\boldsymbol{L}$ is a matrix consists of partial differential operators, $\boldsymbol{C}$ is stiffness as discussed in chapter 2, $\boldsymbol{f}_b$ is the vector of external body forces in the x, y, z directions, $\rho\ddot{\boldsymbol{U}}$ is the inertial force term only existing in the dynamic system. For the displacement boundary conditions, u, v, and w are displacement components, and the bar indicates the prescribed displacement value, which is zero in our case. For the force boundary condition, $\boldsymbol{n}$ is a matrix consists of cosines of the outwards normal on the boundary and the bar means the prescribed value of forces (*Liu and Quek*, 2003).

6.2.2 Model Geometry

The FE model created here aimed to calculate the stress concentration around the borehole wall in a homogeneous, continuous and linear elastic formation. The geometry of the 3-D model is illustrated in Fig. 6.1a, which considers a cylindrical borehole drilled in a rock volume with dimensions of 10 units×10 units×5 units. Units of dimension are not specified in this case, so that the model geometry can be scaled based on the real problem. The ratio of the length of rectangular edges with respect to the borehole diameter is 10:1 in order to avoid model edge effects being superimposed onto the near-wellbore stresses (*Zhang*, 2011). A global Cartesian coordinate system is defined with its origin located at the bottom of the borehole center and its z-direction aligned with the borehole axis.

When the system is only subjected to three principal *in-situ* stresses along with the alignment between the wellbore axis and one of the principal *in-situ* stresses, the model can be reduced to one quadrant in a 2-D plane as the model has symmetrical loading patterns and follows the generalized plane strain assumption (Fig. 6.1b). However, in our experiments as discussed in chapter 3, holes were not always drilled along the direction of the principal stresses. In order to avoid re-generating meshes and keep the same geometry for all borehole orientations of interest, the stress components applied on the faces of the model should come from a rotated stress tensor transformed from the original *in-situ* stress based on the specific borehole deviation and azimuth. Hence, in that case, the resulted stress boundary conditions of the system contain not only the normal stress components, but also the shear stress components. With the existence of shear

stresses, the loading pattern is no longer symmetrical and as such the geometry of the 3-D model cannot be simplified. *Y Y Li* (1997) discussed this issue in detail and provided some preliminary ideas on the way to overcome these problems.

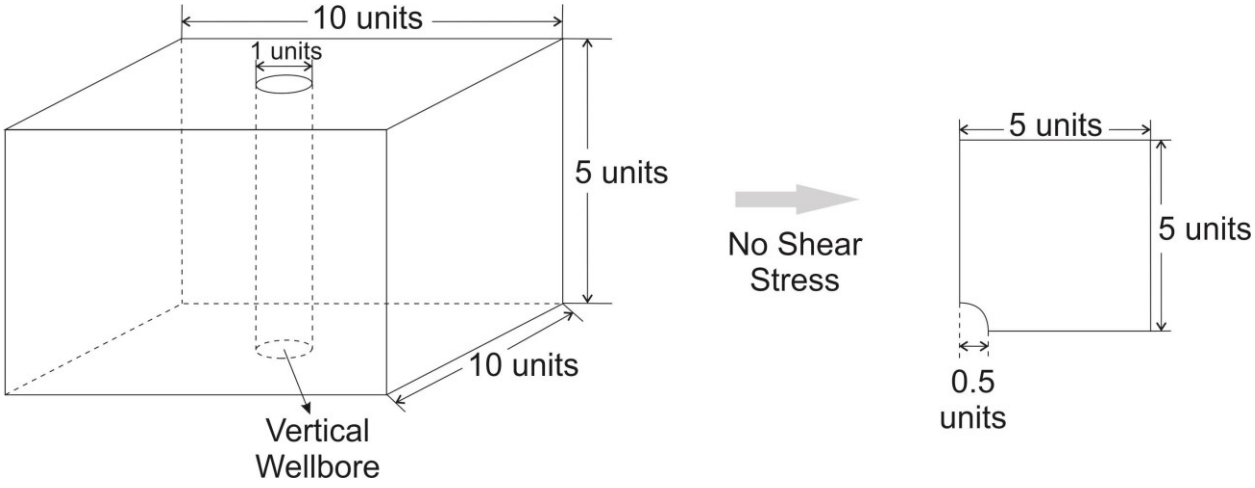

Figure 6.1 The geometry of the 3-D model and its simplified version when there is no shear stress generated.

6.2.3 Element Attributes

All mechanical elements are assigned with their own intrinsic dimensionality, which can be one, two or three dimensions, except for special elements with zero dimension. In a one dimensional case, elements are usually either straight or curved lines. In two dimensions, elements are either in the shape of triangles or quadrilaterals. And in three dimensions, they are volumes of tetrahedral, wedge or bricks shape. Element geometries are defined by nodes. Nodes are usually located at the vertices of elements, and for more complicated elements, nodes can be placed in the middle of edges, faces or even within the central spaces. Triangles and tetrahedral are quite flexible for modeling irregular geometries, therefore, they are commonly utilized in most automatic mesh generations (*Liu and Quek*, 2003). But they may generate less accurate results than those obtained from quadrilateral and brick-like shapes (*Liu and Quek*, 2003). Moreover, during the model discretization, it is very possible to create distorted elements with high aspect ratios in geometrically complicated regions. Such elements are not reliable, and the accuracy of the results produced from them varies with different conditions in the model.

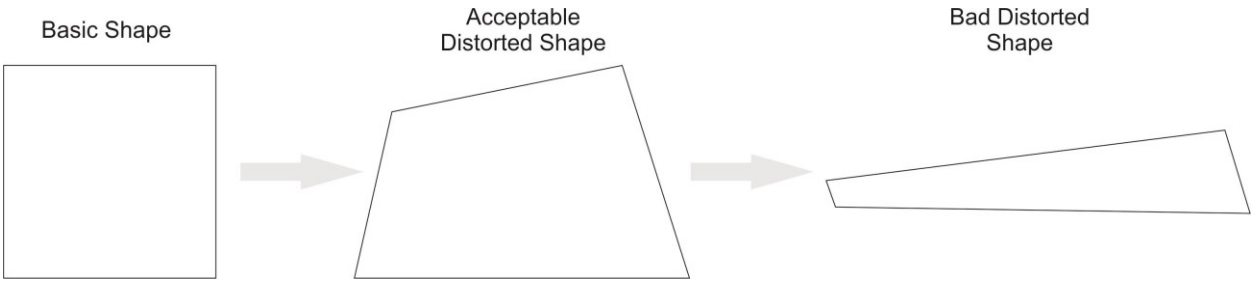

Figure 6.2 From the left to the right: an element with no distortion, an element with acceptable distortion and an element with problematic distorted shape.

In this 3-D FE model, two types of 3-D structural elements are employed: SOLID45 for the main body and SURF154 overlaid onto the entire outer surface to accommodate the structural surface effects, which are shear stresses. Each of these two elements has at least two geometrical options (Fig. 6.3). In this case, the SOLID45 element contains eight nodes with three DOFs at each node as shown on the left side of Fig. 6.3a. All properties of SOLID45 are set to be default. On the other hand, the geometry of the element SURF154 is set to be constructed by only four nodes (Fig. 6.3b right), and the element can be applied by shear stresses on the full area.

6.2.4 Meshing

There are two types of meshing strategies employed in ANSYS^{TM}, free mesh and mapped mesh. There is no restrictions in terms of the element shapes being employed in a free mesh, but triangular and tetrahedral element are preferred in 2-D and 3-D systems, respectively due to their high flexibilities to accommodate irregular geometries (*Moaveni*, 2008). On the other hand, a mapped mesh contains consistent element shapes and patterns defined by the user. Therefore, in order to avoid lower order elements for better accuracy, the model domain is discretized into a mapped mesh which consists of 26224 nodes and 22600 elements with a more refined mesh near the borehole wall (Fig. 6.4). The element size chosen leads to a good balance between calculation time and result accuracy. The aspect ratios of all elements are in a reasonable range as routinely checked by ANSYS^{TM}.

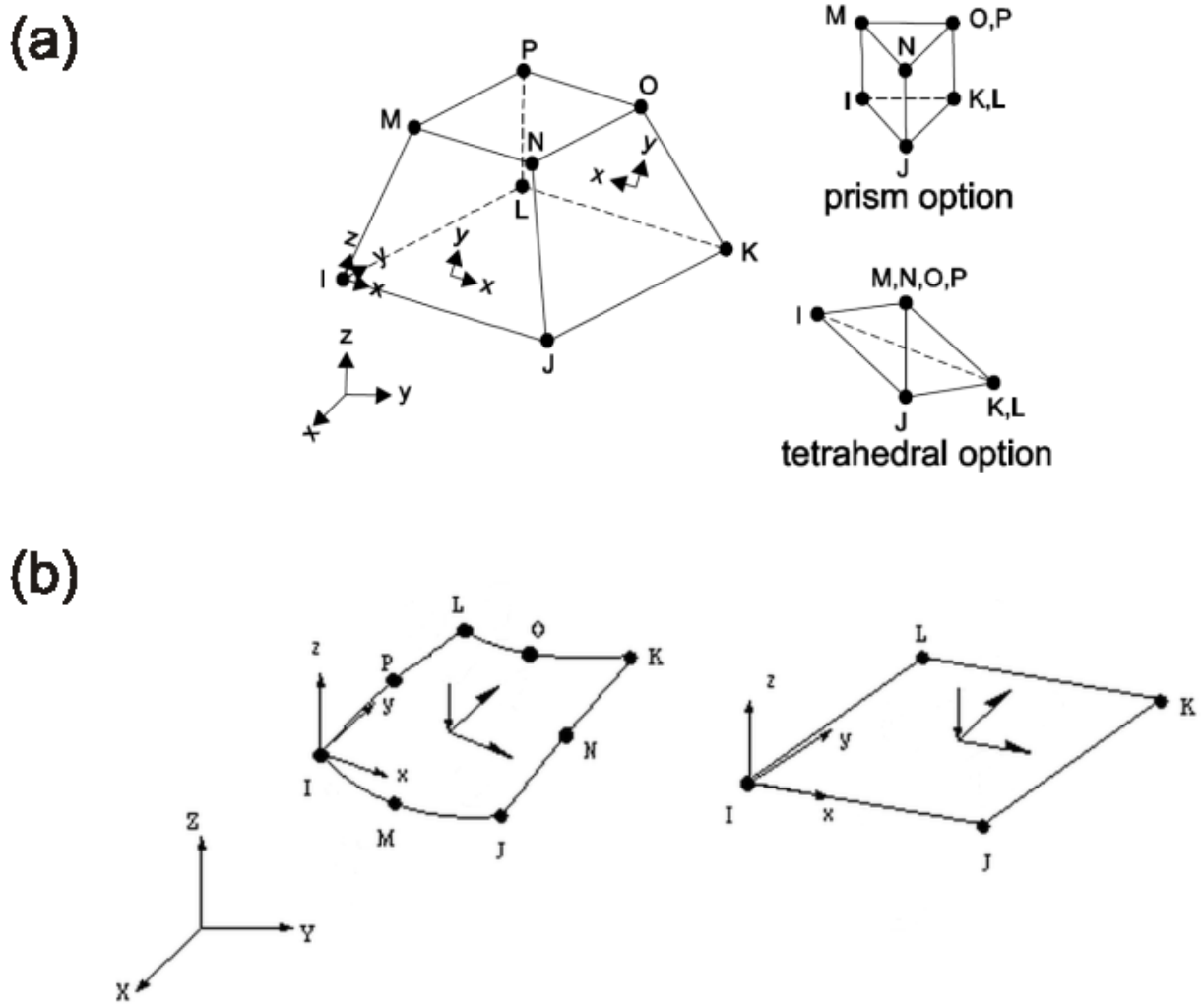

Figure 6.3 (a) SOLID45 3-D structural solid geometry in ANSYS^{TM}. (b) SURF154 3-D structural surface effect element geometry in ANSYS^{TM}.

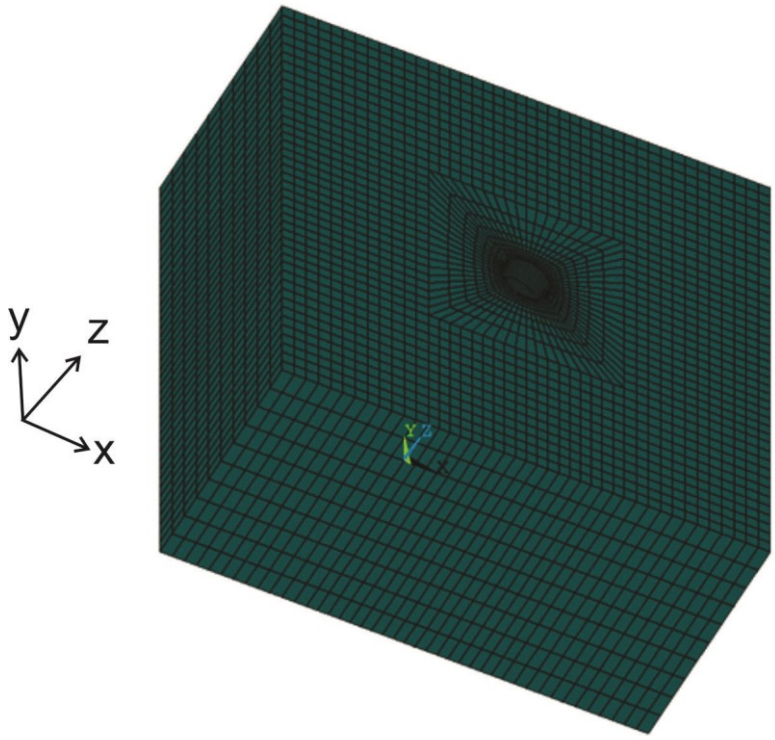

Figure 6.4 The finite element mesh of the 3-D numerical model.

6.2.5 Boundary Conditions

The key difference between essential and natural boundary conditions was discussed previously. The natural boundary conditions in this model are the normal and shear stresses applied on the faces of the model, which vary with different situations. In this section, we mainly discuss the essential boundary conditions defining constraints on displacements (Table 6.1). Without symmetries and connections, the BCs only contain structural support constraints. Since the model is simulating rocks deeply buried within the earth, nodes on all surfaces of the model are assumed to be restricted to move along the vertical direction. Additionally, to suppress unwanted rigid body motions, two more BCs are applied: (1) all DOFs at nodes in line A are fixed to avoid translational motion; (2) the displacement in the x direction on the front surface colored in grey is deleted to better accommodate deformations resulted from shear stresses.

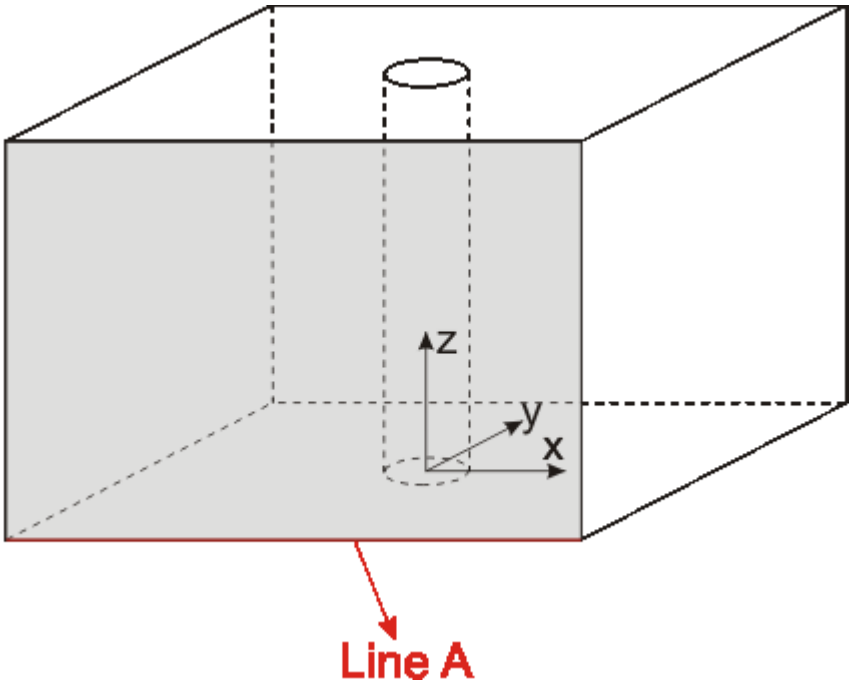

Figure 6.5 Illustration purpose for the rigid body motion suppressions.

Table 6.1 Essential boundary conditions in the FE model.

Location	Description	Constraints
x=-5 x=5 y=-5 y=5 z=0 z=5	All Faces	UZ=0*
x=-5 and y=-5	Line A	All DOFs are fixed
x=-5	The Front Face in Grey	UX=0

* UZ=0 indicates the displacement along the z direction is constrained.

6.3 Model Development and Validations

The development of the 3-D model was initially built from a 2-D base model as shown in Fig. 6.6. The restriction of the simplified 2-D model is that it can only support normal stresses due to its requirement on the double symmetry in terms of the geometry and loading patterns. The 2-D mesh consists of 1911 nodes and 600 quadrilateral elements. The mesh is refined near the borehole where the stresses change rapidly. The element used in this model is a higher order 2-D, 8-node, having two DOFs at each node, quadrilateral structural element, called PLANE183, which is also suitable for irregular meshes (*Yazdizadeh*, 2010). Boundary conditions are also shown in this figure, where arrows represent the direction of compression. Based on the symmetry properties, nodes along the lines of symmetries are constrained, and they can only slide along the symmetry lines (indicated by rollers).

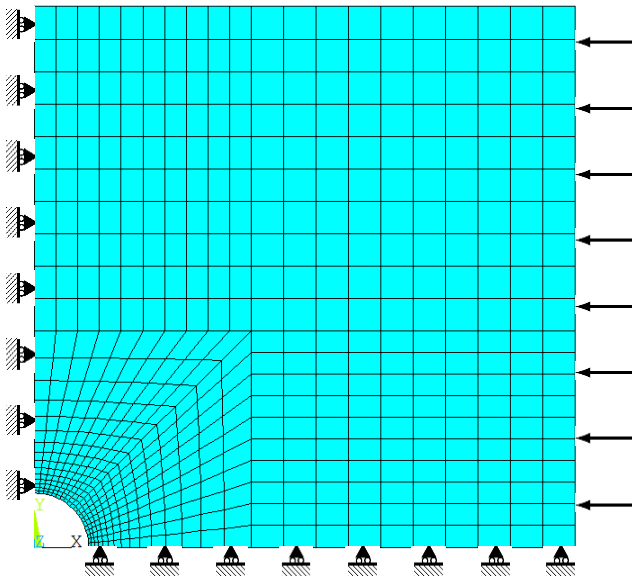

Figure 6.6 View of the mesh and boundary conditions of the 2-D finite element model.

Figure 6.7 illustrates the stress in the x direction (σ_x) calculated from the L-A solution (left) and the FEM (right). In this case, the formation is assumed to be isotropic with a Young's modulus of 29GPa and a Poisson's ratio of 0.3. To simplify our model, only the maximum horizontal stress exists, which is 1MPa, and the direction is indicated in Fig. 6.7. The actual value is not that important as we can always scale the results in terms of Young's modulus. The same cannot be

said about Poisson's ratio, however, as it is key for controlling the distributions of the stresses (*Y Li and Schmitt*, 1997). In ANSYS^{TM}, the color bar shows a reverse value compared to the MATLAB^{TM} results. It is important to note here a key change in the rules for positive and negative stresses in this chapter; here a positive stress value indicates tension, whereas the negative value is compression. This is because commercial finite element codes were designed more by physicists and mechanical engineers who employ this convention.

Note that the original ANSYS data set has a relatively coarse coverage than that of the analytical solution. Moreover, Fig. 6.7b is plotted based upon the linear interpolations of the original numerical data in order to fit a similar surface plot like Fig. 6.7a. The result range of the analytical solution is from -2.9858 to 0.0616 MPa, and the range for the numerical model is from -3.3484 to 0.0867MPa. The difference may come from the limitations of gridding of the numerical model and the linear interpolation process.

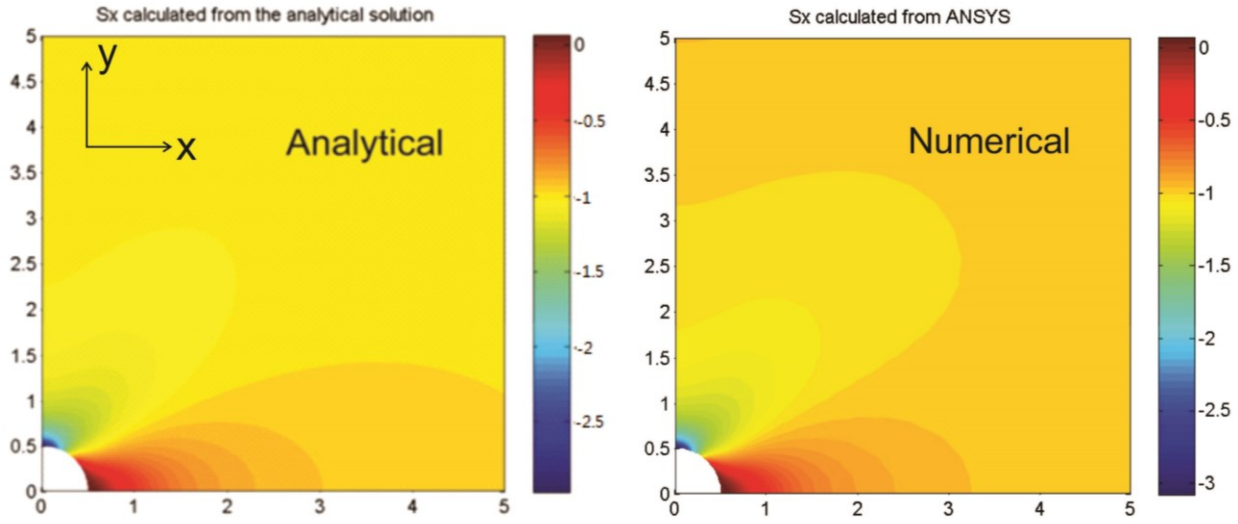

Figure 6.7 The stress in the x direction (σ_x) around a vertical borehole wall in an isotropic formation calculated from the L-A solution (left) and the numerical simulation (right). In this case, σ_x = 1MPa; other stresses are all zero. The borehole axis co-incides with the vertical principal in-situ stress. The results between these two solutions agree well.

The next step for the validation processes is to test if the model can correctly calculate the shear stresses correctly. The material properties are the same as those in the previous case. The boundary conditions in terms of stresses here are as follows:

$$\sigma_x^0 = 1\text{MPa}, \tau_{xy}^0 = \tau_{yx}^0 = 1\text{MPa}, P_p = 0\text{MPa}, P_w = 0\text{MPa}$$

Since there are shear stresses acting within the x-y plane, the model has to be upgraded to a full-size 2-D model. Its boundary conditions are illustrated in Fig. 6.8 (top). Point A has been fixed in motion to provide translational restraint, whereas, Point B has been restricted to move along the y direction, since the integration of both Support A and support B can stop the rigid body from rotational movements. The result obtained from the 2-D numerical model is shown in Fig. 6.8 (bottom). Applying with the same stress conditions on the analytical model (Fig. 6.9), we observe a good agreement between those two results. The 3-D model was developed based upon the 2-D model. By comparing the results obtained from the 3-D model under the same loading condition (Fig. 6.10) with the other two results, they basically match among one another. Therefore, we can conclude that the 3-D numerical model has been validated.

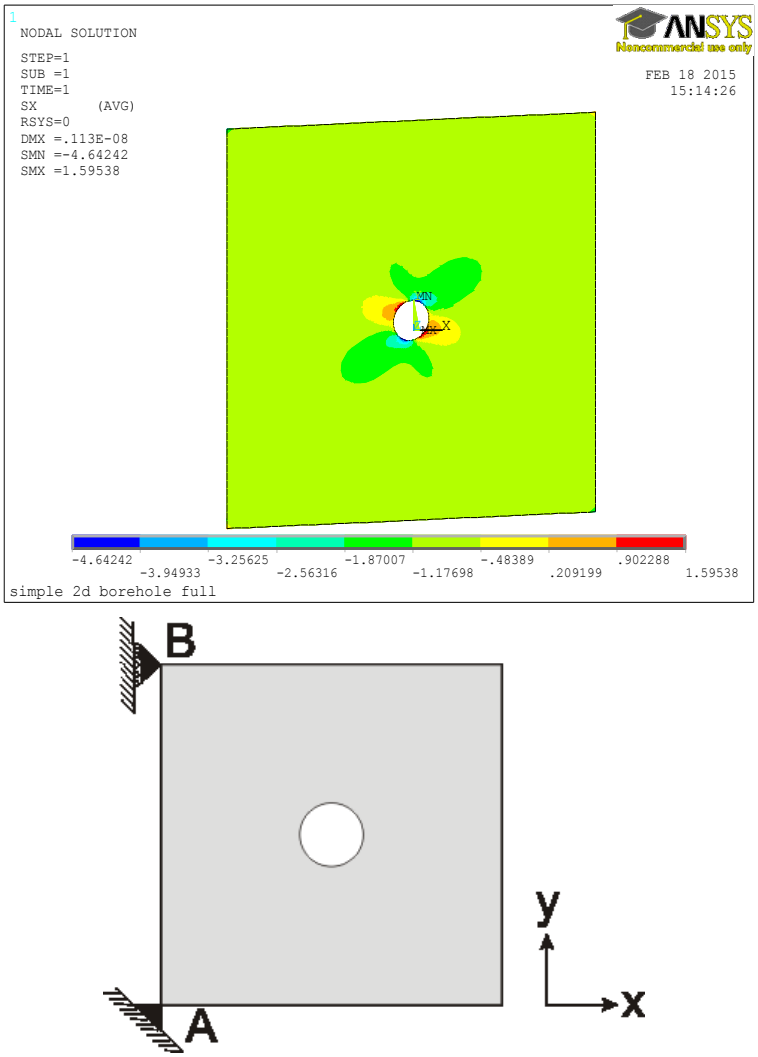

Figure 6.8 The stress concentration in the x direction calculated from the 2-D numerical model (top) and its boundary conditions on nodal point displacements (bottom). In this case, σ_x = 1MPa and $\tau_{xy} = \tau_{yx}$ = 1MPa; other stresses are all zero.

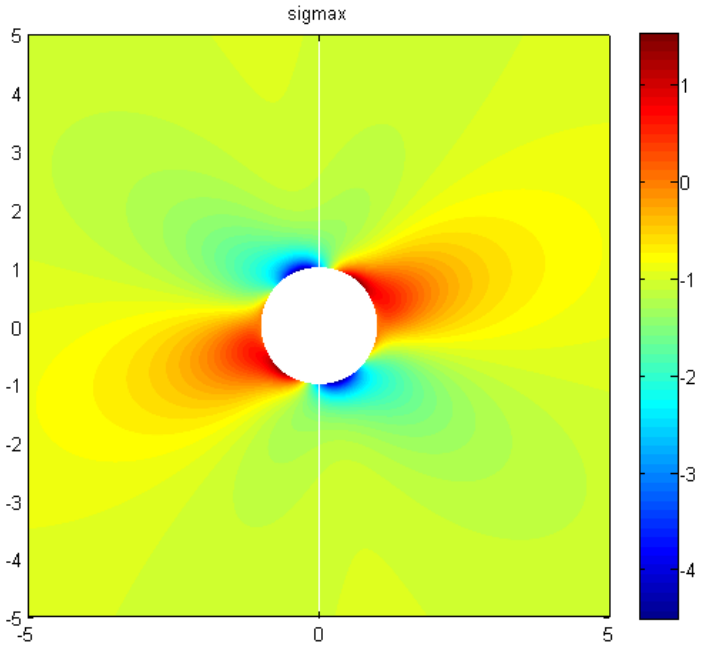

Figure 6.9 The stress in the x direction (σ_x) around a vertical borehole wall in an isotropic formation calculated from the L-A solution. This is a comparison with the numerical results.). In this case, σ_x = 1MPa and $\tau_{xy} = \tau_{yx}$ = 1MPa; other stresses are all zero.

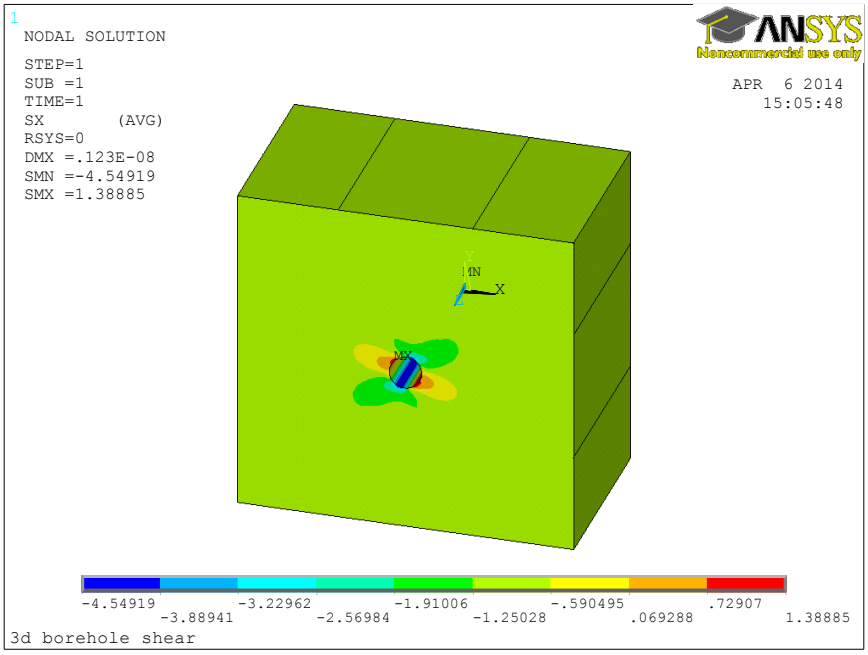

Figure 6.10 The stress concentration in the x direction calculated from the 3D numerical model. In this case, σ_x = 1MPa and $\tau_{xy} = \tau_{yx}$ = 1MPa; other stresses are all zero.

6.4 A Roadmap for Future Study

This part of research including the photoelasticity experiments is still in the preliminary phase. After completing the development of the 3-D static numerical model, we hope to utilize this model to compare it with the experimental results. Once we acquire the stress data from the strain gauge mounted on the glass cube, the data can be rotated into the borehole coordinate system and then input into the 3-D numerical model. The static model can provide us the stress concentration inside the glass cube any time before the crack initiations.

However, in order to simulate the fracture growth in real-time, a 3-D dynamic model is required and a multi-step load should be applied on the system. The deformations resulted from loading vary with time as well. Furthermore, after the moment of the initial fracture generated, stresses will be re-distributed as fractures propagate and force changes in each step, and the fracture propagation path will be determined simultaneously. Eventually, the model can provide simulation results on time-varying stress concentrations, deformations and fracture paths.

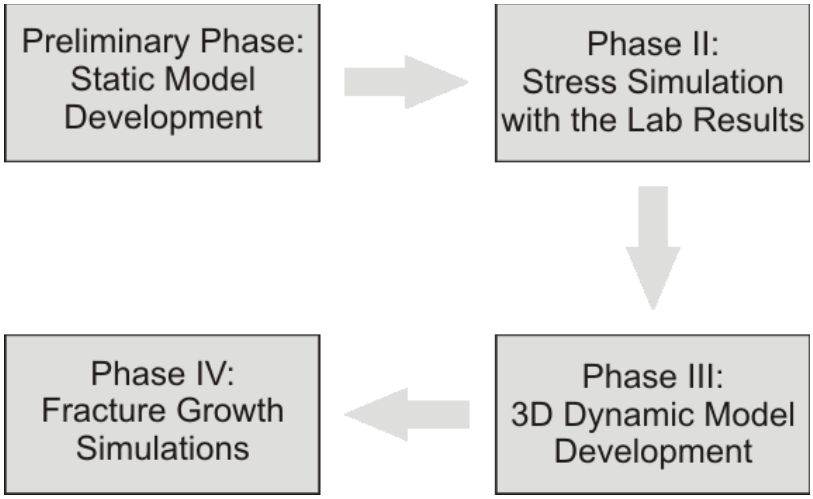

Figure 6.11 The flowchart showing the plan for the numerical model development.

6.5 Summary

This chapter presents a 3-D numerical model created from a finite element solver, ANSYS^{TM}. The aim of developing such a model is to simulate the experimental process and compare its

results with those obtained from the photoelasticity tests in terms of stress concentrations and fracture propagations. First, some main concepts of the finite element method were reviewed followed by the detailed descriptions of the 3-D FE model including the model geometry, element attributes, meshing and boundary conditions. Second, we introduced two simplified 2-D models upon which the 3-D model was built and the validations of those numerical models against the L-A analytical solutions discussed in Chapter 4. Last, as this study is only in its preliminary stage, some suggestions are presented for the future work. The final goal is to build a real-time 3-D dynamic model which will be used to mimic the whole experimental process.

6.6 References

Chatterjee, R., and M. Mukhopadhyay (2003), Numerical modelling of stress around a wellbore, SPE Asia Pacific Oil and Gas Conference and Exhibitio, Society of Petroleum Engineers, SPE-80489-MS, Jakarta, Indonesia, 9-11 September.

Li, Y., and D. R. Schmitt (1997), Effects of poisson's ratio and core stub length on bottomhole stress concentrations, *International Journal of Rock Mechanics and Mining Sciences*, *34*(5), 761-773.

Li, Y. Y. (1997), Drilling induced core damage and its relationship to crustal in situ stress states and rock properties, Ph.D. Thesis, 231 pp, University of Alberta, Edmonton, Alberta.

Liu, G. R., and S. S. Quek (2003), *Finite element method [electronic resource] : a practical course / G.R. Liu, S. Quek*, Oxford : Butterworth-Heinemann, 2003.

Moaveni, S. (2008), *Finite element analysis : theory and application with ANSYS / Saeed Moaveni*, 3rd ed., Upper Saddle River, N.J. : Pearson Prentice Hall, c2008.

Yazdizadeh, B. (2010), Comparison of different PLANE models in finite element software in structural mechancis, *Proceeding of Yerevan State University*, *3*(6), 7.

Zhang, L. (2011), Three-dimensional numberical models of drilling induced core fractures, MSc Thesis, University of Alberta, Edmonton, Alberta.

Zienkiewicz, O. C., R. L. Taylor, and J. Z. Zhu (2013), *Finite element method: its basis and fundamentals*, 7th ed., Amsterdam ; Boston : Butterworth-Heinemann, 2013.

Chapter 7

Conclusions

This thesis is part of the study for the development of engineered geothermal systems (EGS) funded by the Helmholtz-Alberta Initiative. Developing the geothermal energy technology in Alberta can decrease the emission of greenhouse gases and offer us alternative green energy resources for oil sands explorations (*Chan*, 2013). Stress is an important input for geothermal system simulations as it makes significant contributions for well stimulation and further controls the path of fluid migration. Knowledge of the *in-situ* stress and rock failure mechanisms enables us to better predict the consequential fracture growth in the formation of interest and enhance the geothermal energy production. This motivates us to improve the systematic analysis for stress estimations and provide a better insight for the mechanical behavior of tensile fractures around the borehole wall. This study, which integrates analytical models, numerical models and laboratory experiments, aims to provide a more comprehensive workflow from the geomechanical perspective and implement it into the geothermal system design.

7.1 Contributions of This Thesis

A feasible method to build a complete *in-situ* stress tensor is by utilizing the relationship between the failure mechanism of the borehole fractures and stresses, and a direct way to achieve the fracture information around a borehole is through the interpretation of borehole images (*e.g.*, formation ultrasonic image logs). This approach has been developed and implemented extensively in numerous studies. Chapter 3 of this study reviewed some of the principals including the analytical solutions of borehole stress calculations, the introduction of borehole fractures and the usage of image logs. Moreover, to simulate the behavior of tensile fractures around the borehole wall, several photoelasticity tests have been carried out which is also discussed in Chapter 3.

These lab experiments reveal the following observations:

- For borehole wall fractures, axial tensile fractures tend to occur around the borehole when one of the principal stresses is aligned with the hole's trajectory; otherwise, *en echelon* tensile fractures occur.
- For bottom hole fractures, their strike in multiple directions as there is no lateral confining pressure, but they propagate along the hole axis initially, and then reoriented to open normal to the minimum principal stress.

With the increasing need of unconventional reservoir explorations and developments, more and more formations with intrinsic anisotropic properties are becoming the targets of deviated drilling. The second part of this study is to investigate the manner in which the anisotropy affects the borehole stresses and DITF growths. The closed-form solutions based on those pioneer works were coded generating direct visualizations of the stresses around a borehole wall and DITF traces on an unwrapped borehole wall. As such, the factor of formation anisotropy can be integrated into the systematic borehole stability analysis and far-filed stress estimations. The results of this section include:

- The L-A solution for borehole stress calculations in the anisotropic formation can also be reduced to the isotropic case.
- The MATLAB^{TM} code developed for borehole stress visualizations provides us direct visualizations on stress concentrations around any arbitrarily oriented borehole in any arbitrarily oriented anisotropic formation.
- An example of the utilization of the MATLAB^{TM} program is presented showing us for this specific borehole orientation (β=40°, α=0°), vertical transversely isotropic formations can change the tendency of fracture initiations in different ways depending on the faulting regime.
- The other MATLAB^{TM} based program can show us DITF traces on the unwrapped arbitrarily oriented borehole wall under different stress conditions in either isotropic or anisotropic formations. This program can be used to compare with the fractures observed from image logs.
- *En echelon* tensile fractures appear to be in asymmetrical pairs.

The last section of this study concentrated on presenting the static 3-D numerical model created in a finite element software, called ANSYS^{TM}. The goal of numerical model development is to simulate the photoelastity tests dynamically in three dimensions and then make improvements based upon it for predictions in more complex cases. As this part of work is in its preliminary stage, we only introduced details of the finite element model (*e.g.*, geometry, elements, BCs, etc.) and its validations. A roadmap for the future study was also provided.

7.2 Suggestions for Future Work

To better predict fracture behavior, future work should focus on two aspects: improving photoelasticity tests and building a more advanced finite element model. Regarding to the lab experiments, more sophisticated experimental setups are needed especially if we want to apply lateral confining pressure on the specimen. A higher rotation speed of the drilling bit is necessary to drill glasses as a speed lower than the requirement can lead to micro-cracks and flaws on the surface of the hole. Those flaws and cracks can promote the generations of tensile fractures resulting in an underestimated fracture initiation pressure, and they can even change the tensile fracture path. Furthermore, to further study the impacts of formation anisotropy, we can try to find an anisotropic transparent material to substitute glasses, but this kind of material is very difficult to achieve. Last, more than one camera should be placed in front of the specimen in different positions during the tests in order to avoid any blind spot for crack detection.

The advanced version of the finite element model should be in dynamic mode as it could simulate the lab process in real-time. Therefore, with the time-varying load being applied on the system, stresses inside the specimen can be re-calculated and re-distributed. The change of stress is significantly especially after the moment of fracture initiation. Eventually, this model can provide the final fracture path and the specimen deformation.

Reference:

Chan, J. (2013), Subsurface geophysical characterization of the crystalline canadian shield in Northeastern Alberta: Implications for geothermal development, M.Sc. thesis, 259 pp, University of Alberta, Edmonton, Canada.

Appendix A

Principles of Birefringence and Photoelasticity

The purpose of this Appendix is to provide the necessary background information to be able to understand the origin of the photoelastic fringes observed in the stressed glass blocks mentioned in Chapter 3. In order to fully understand the phenomenon of birefringence, we briefly review the nature of light and its polarization. Visible light propagates as an electromagnetic wave with wavelengths range from ~400 nm (violet) to ~700 nm (red). Wavelengths shorter and longer than this are in the ultraviolet and infrared portions of the electromagnetic spectrum, respectively. An electromagnetic wave consists of oscillating transverse magnetic (**H**) and electric (**E**) field components. In a linearly polarized wave (Fig. A.1), the field vectors of these are perpendicular to one another. The wave polarization is described by the plane of the **E** field vector as illustrated in Fig. A.1.

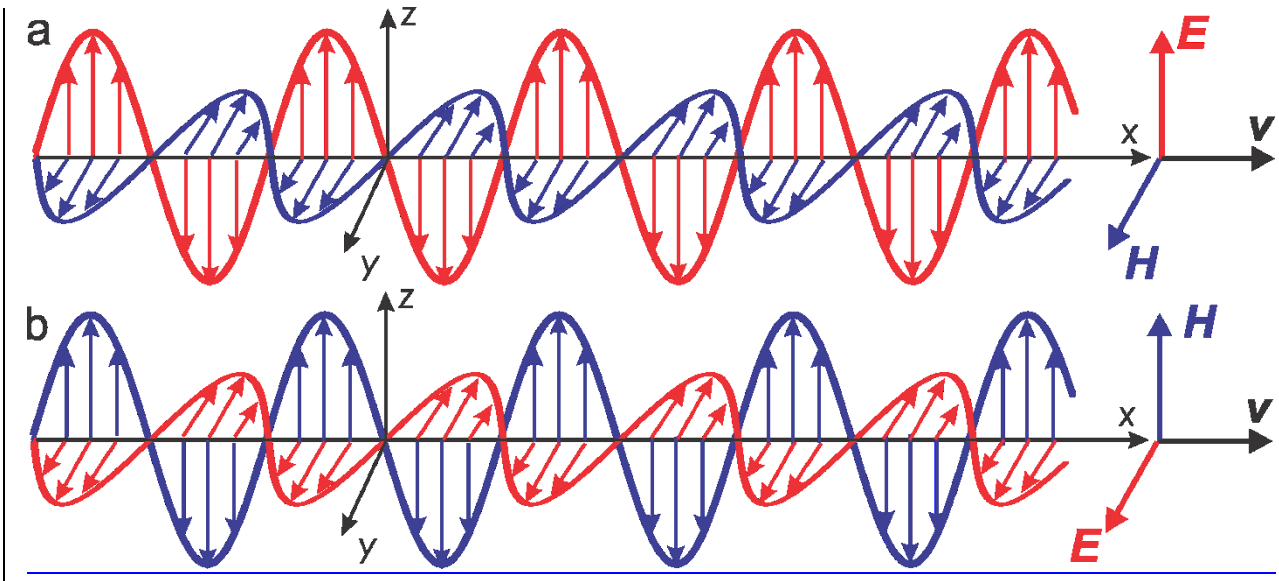

Figure A.1 Linearly polarized electromagnetic (EM) waves, consisting of alternating electric **E** field and magnetic **H** fields, propagating to the right along the x-axis with speed *v*. a) $\mathbf{E_z}$ with **E** lying in the vertical x-z plane. b) $\mathbf{E_y}$ with **E** lying in the horizontal x-y plane. Figure courtesy of D. R Schmitt from Rock Physics Class Notes.

In Fig. A.1, we see the two waves both of which are drawn propagating at the same speed *v*. This situation occurs in vacuum and optically isotropic material. If the material is optically isotropic then the originally polarization of the light does not change upon refraction into the second medium. Generally, cubic and transparent minerals such as halite and sylvite are optically isotropic and will not change the transmitted polarization of the incident light. Glass, too, in the absence of residual stresses should also be optically isotropic. This will not be the case in other minerals, however.

Before proceeding, it is useful to discuss the speed of light in materials. The refractive index of a material demonstrates the way that light or other electromagnetic waves travel inside this material, and its mathematical form is the simple ratio

$$n = \frac{c}{v} \tag{A.1}$$

where *c* is the speed of light in vacuum, currently defined to be 299,792,458m/s (according to the NIST reference on Constants, Units, and Uncertainty), and *v* is the speed in that material. Based on Snell's law, we can also determine how the light path is changed after passing an interface of two different (but optically isotropic) materials (Fig. A.2) where Snell's law is defined as

$$n_1 sin\theta_1 = n_2 sin\theta_2 \tag{A.2}$$

where n_1 and n_2 are the refractive indices of these two materials, respectively, and $\theta_1$and $\theta_2$are the respective angles of incidence and refraction.

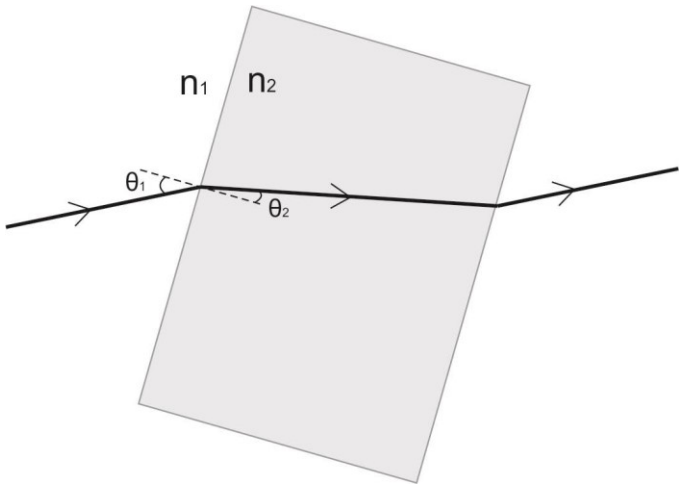

Figure A.2 Illustration of light refraction when a beam of light traveling from a material (no color) with an index of refraction of n_1 into a block (in grey) with an index of refraction of n_2. This process obeys Snell's law of refraction. Arrows indicate directions of the light propagation.

However, when one of the two materials is optically anisotropic, the incident light beam is separated upon refraction into two perpendicularly polarized beams each traveling in the same material with different speeds v_1 and v_2, and this phenomenon is called double refraction or birefringence. In order to illustrate this, consider the somewhat simplified case in Fig. A.3 that shows a green and a red components of white light propagating in the x direction within, say, air at a speed v and wavelength λ. Note that this wave has already been polarized at an arbitrary angle rotated within the y-z plane, that is the original randomly polarized white light passed through a polaroid filter, for example. This polarized wave is incident to an optically anisotropic crystal (in yellow) with thickness t.

The crystal structure is a principal factor for the polarization directions and consequently the energy of the incoming wave is partitioned into two components polarized in the, here conveniently chosen, fast z and slow y directions. The polarizations of those two beams are orthogonal to each other, and their directions correlate with the principal elliptical axes of the material. The principal axes are defined as the coordinate axes of a system of reference for which the dielectric permittivity tensor is diagonalized (*Chartier*, 2005).

Within the material these two polarizations will respectively propagate at speeds v_1 and v_2 with corresponding wavelengths λ_1 and λ_2. Fig. A.3 shows green (a) and red (b) components with

shorter and longer wavelengths in air denoted by the colored λ's. The corresponding wavelengths of the 'split' polarizations within the material will necessarily be shorter because lower speeds there and because $v_1 > v_2$ then $\lambda_1 > \lambda_2$. The split waves transit the material and exit it again into isotropic air at the right side of the crystal without disruption to their polarization whereupon both polarizations again travel at the same speed v and wavelength λ as the original incident wave. However, the phase of these two polarizations are now shifted by a length δ which depends on v_1 and v_2, the thickness t, and the frequency $f = v/\lambda$. The phase δ is shown as a shift in space in Fig. A.3 but it could just as easily be described as a retardation angle Δ by:

$$\Delta = 2\pi\left(\frac{1}{\lambda_2} - \frac{1}{\lambda_1}\right)t \tag{A.3}$$

If $\Delta = 2n\pi$ where $n = 0, \pm1, \pm2 \ldots$ then the two waves are in phase with one another. In contrast if $\Delta = n\pi$ where $n = 0, \pm1, \pm2 \ldots$ then the waves are completely out of phase.

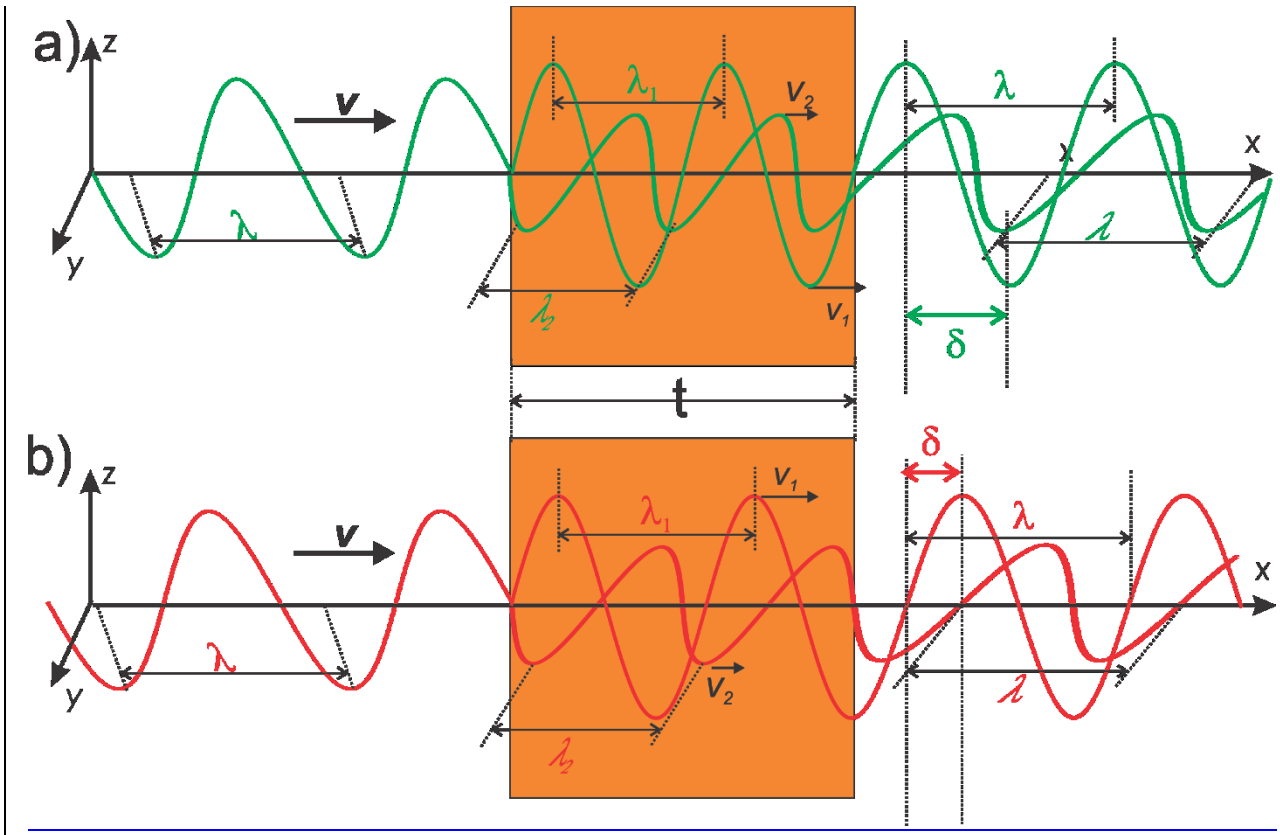

Figure A.3 Illustration of the development of phase retardation for a shorter (green) and longer (red) wavelength portions of a beam of polarized white light. The light propagates from left to right in the figure. The speed of light in the air is v, while the material polarizes the light into a vertically (a) and horizontally (b) polarized beams that propagate with speeds v_1 and v_2, respectively. These two polarizations persist upon exiting the crystal with different phase retardations δ shown in green and red to indicate they will differ for the different colours (i.e. wavelengths or frequencies).

In Fig. A.3 the different polarizations propagate independently once they leave the material. Suppose one now places a second polarizing filter to the right of the material. The analyzer may be rotated in order to change the orientation of the polarization that it passes; if oriented vertically or horizontally it will pass only the z- or the y-polarized waves, respectively. If oriented at some other angle, however, it will partially pass both the z- and y-polarized waves to produce a new wave with a single polarization direction that was controlled by the rotation of the analyzer. If the two split waves were in phase (case 1: $\Delta = 2n\pi$) then these components perfectly add together for strong constructive interference and the light can be observed. In contrast, if they are perfectly out of phase (case 2: $\Delta = n\pi$) then they will interfere destructively; effectively this frequency (colour) cannot be observed. At other values of Δ, portions of the light will still have some degree of constructive interference and their frequency is still passed. The observer sees the original spectrum of the white light *less* those frequencies that experience destructive interference; and this is then perceived by the human eye as having color. Conversely, the color seen tells us what the phase retardation is.

Birefringence can be either natural or induced. For natural birefringence, the orientations of the principal axes or intrinsic optical anisotropies are resulted from the layout of the crystalline lattice (*Chartier*, 2005). Many materials exhibit inherent birefringence, such as quartz (SiO_2) and calcite ($CaOCO_2$), and they are utilized in various optical instruments (*Cloud*, 2008). Another class of birefringence is induced by the unsymmetrical external environment, for instance, mechanical stresses or a magnetic field, and one of the coordinate axes is aligned with the principal direction of the external field (*Chartier*, 2005).

The stress induced birefringence is also called photoelasticity. This gives rise to the stress-optic law. For a slab with thickness d, being immersed in a fluid with refractive index n_0, under an unsymmetrical mechanical stress field, its absolute retardations can be expressed in terms of the principal stresses, σ_1 and σ_2, its absolute photoelastic coefficients, C_1 and C_2, and its principal refractive indexes n_1 and n_2. The mathematical form is as follows (*Cloud*, 2008)

$$R_1 = (C_1\sigma_1 + C_2\sigma_2)d$$

$$R_2 = (C_2\sigma_1 + C_1\sigma_2)d \tag{A.4}$$

or

$$R = R_1 - R_2 = (C_1 - C_2)(\sigma_1 - \sigma_2)d \tag{A.5}$$

where R is the relative retardation, and it can be expressed as

$$R = \left(\frac{n_1 - n_2}{n_0}\right)d \tag{A.6}$$

Moreover, the stress-optic coefficient, C_σ, is defined as

$$C_\sigma = C_1 - C_2 \tag{A.7}$$

At last, we can get (*Cloud*, 2008)

$$R = C_\sigma(\sigma_1 - \sigma_2) \tag{A.8}$$

That said, the birefringence is directly proportional to the principal stress difference and the refraction indices difference.

The typical configuration for a photoelasticity test as illustrated in Fig. A.4 usually consists of two polarizing filters and an optical sample having stress birefringent effects. A beam of natural light first passes through a polarizing filter, called ‘polarizer’, generating a polarized light. Then two beams of polarized light with different speeds are generated within the optical sample due to the photoelastic effect. Their polarization directions are orthogonal to each other and are determined by the external principal stresses, σ_1 and σ_2. Last, when those two beams travel through the second polarizing filter, called ‘analyzer’, their interference between each other lead

to a certain visible spectrum as described above. By rotating the analyzer, the characteristic of color spectrum can be changed.

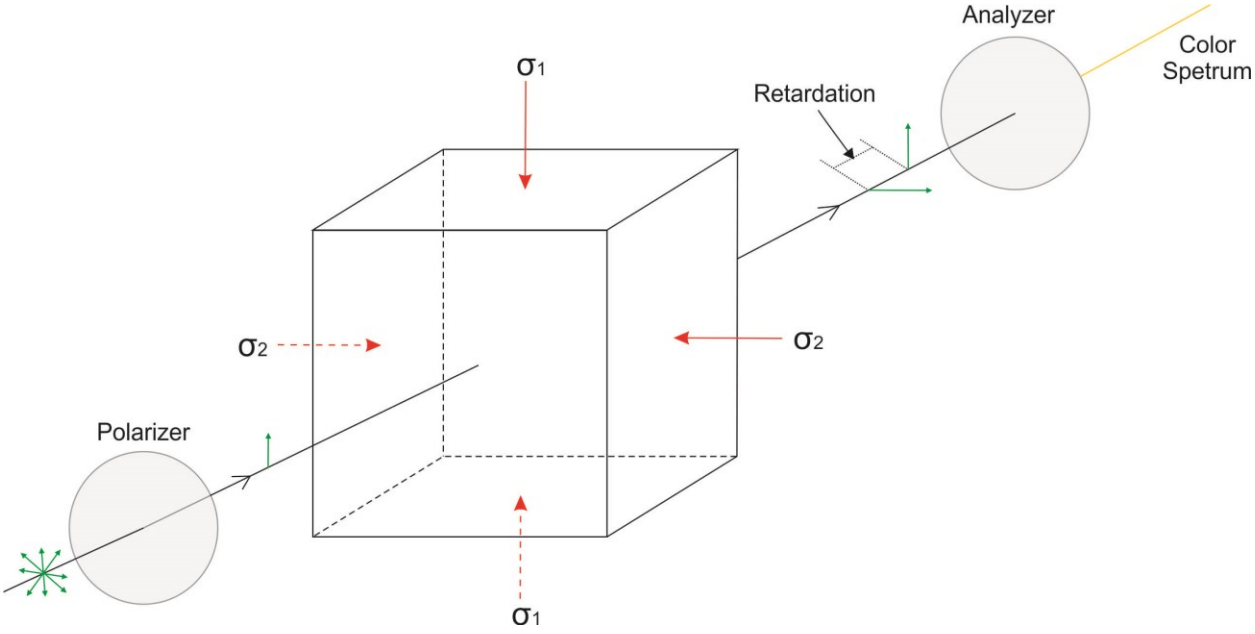

Figure A.4 Transmission of a beam of natural light in the photoelasticity experimental setup. Green arrows indicate polarization directions of light. Polarizer is the first polarizing filter that the light encounters forming in a beam of polarized light. The cube represents an optical sample with stress birefringent effects. After traveling through the sample, the light is separated into two beams of polarized light with different speeds. Upon rotating the second polarizing filter, also known as the analyzer, we can control the appearance of the color spectrum.

In our study, we discovered that a LED desktop monitor set with a 'white' background emits polarized light directly obviating the need for an initial polarizer; however, the orientation of the light polarization is not known. The analyzer is mounted on the lens of the camera. During the experiments, the direction of the analyzer is rotated to be perpendicular to the direction of the polarizer in order to achieve the desired color spectrum. Glass cubes are selected as our optical sample.

References

Chartier, G. (2005), *Introduction to optics*, Springer, c2005., New York.
Cloud, G. (2008), Optical methods in experimental mechanics: Part 30: Photoelasticity II - Birefringence in materials, *Experimental Techniques*, *32*(1), 13-16.

Appendix B

MATLAB Code for Borehole Stress Calculation in Anisotropic Materials

Stress_anisotropic_plain.m

```
% This script calculates the stress concentration around the borehole
% wall in anisotropic or isotropic formations.
clf;
clear;
close all;

a=1;
taoxy0=0;
taoxz0=0;
taoyz0=0;
c11=33.20;
c13=4.98;
c33=22.184;
c44=10.906;
c66=14.60;
sigmax0=1;
sigmay0=0;
sigmaz0=0;

pw=0;
%% stress transformation
stress=stress_transformation(sigmax0,sigmay0,sigmaz0,taoyz0,taoxz0,taoxy0,60,
0,0,0);
% ATTENTION: the borehole angle in this part should be the same as the later
one when you transform the compliance matrix.

sigmax0=stress(1);
sigmay0=stress(2);
sigmaz0=stress(3);
taoxy0=stress(6);
taoxz0=stress(5);
taoyz0=stress(4);

%% elastic constants
c12=c11-2*c66;
c22=c11;
c23=c13;

S=[c11,c12,c13,0,0,0;
    c12,c22,c23,0,0,0;
    c13,c23,c33,0,0,0;
    0,0,0,c44,0,0;
    0,0,0,0,c44,0;
    0,0,0,0,0,c66];
```

```
A1=S^(-1);
A=compliance_transformation(0,0,60,0,A1); %rectilinear anisotropy symmetry
plane is horizontal and the borehole is horizontal as well.
a11=A(1,1);
a12=A(1,2);
a13=A(1,3);
a21=A(2,1);
a22=A(2,2);
a23=A(2,3);
a33=A(3,3);
a34=A(3,4);
a35=A(3,5);
a36=A(3,6);
a44=A(4,4);
a66=A(6,6);

%% beta
beta55=A(5,5)-(A(5,3)*A(5,3))/a33;
beta45=A(4,5)-(A(4,3)*A(5,3))/a33;
beta44=A(4,4)-(A(4,3)*A(4,3))/a33;
beta11=A(1,1)-(A(1,3)*A(1,3))/a33;
beta16=A(1,6)-(A(1,3)*A(6,3))/a33;
beta12=A(1,2)-(A(1,3)*A(2,3))/a33;
beta66=A(6,6)-(A(6,3)*A(6,3))/a33;
beta26=A(2,6)-(A(2,3)*A(6,3))/a33;
beta22=A(2,2)-(A(2,3)*A(2,3))/a33;
beta15=A(1,5)-(A(1,3)*A(5,3))/a33;
beta14=A(1,4)-(A(1,3)*A(4,3))/a33;
beta56=A(5,6)-(A(5,3)*A(6,3))/a33;
beta25=A(2,5)-(A(2,3)*A(5,3))/a33;
beta46=A(4,6)-(A(4,3)*A(6,3))/a33;
beta24=A(2,4)-(A(2,3)*A(4,3))/a33;
%% miu1&miu2
p1=[beta55,-2*beta45,beta44];
p2=[beta11,-2*beta16,(2*beta12+beta66),-2*beta26,beta22];

miu11=roots(p1);
miu22=roots(p2);

miu3=miu11(1);
miu1=miu22(1);
miu2=miu22(3);

%% lamda1 2 3
l2_miu1=beta55*miu1^2-2*beta45*miu1+beta44;
l2_miu2=beta55*miu2^2-2*beta45*miu2+beta44;
l2_miu3=beta55*miu3^2-2*beta45*miu3+beta44;

l3_miu1=beta15*miu1^3-(beta14+beta56)*miu1^2+(beta25+beta46)*miu1-beta24;
l3_miu2=beta15*miu2^3-(beta14+beta56)*miu2^2+(beta25+beta46)*miu2-beta24;
l3_miu3=beta15*miu3^3-(beta14+beta56)*miu3^2+(beta25+beta46)*miu3-beta24;

if l2_miu1==0
    lamda1=0;
else
lamda1=-l3_miu1/l2_miu1;
```

```
end

if l2_miu2==0
    lamda2=0;
else
lamda2=-l3_miu2/l2_miu2;
end

if l2_miu3==0
    lamda3=0;
else
lamda3=-l3_miu3/l2_miu3;
end

%% triangle
triangle=miu2-miu1+lamda2*lamda3*(miu1-miu3)+lamda1*lamda3*(miu3-miu2);

%%

%t=0:(2*pi/1000):2*pi;
X1=linspace(0,5,1001);
Y1=linspace(-5,5,2002);
[x,y]=meshgrid(X1,Y1);

for jj=1:2002
    for vv=1:1001
        r=((x(jj,vv))^2+(y(jj,vv))^2);
        if r<a
            x(jj,vv)=NaN;
            y(jj,vv)=NaN;
        end
        if x(jj,vv)==0      % when x=0 or y=0, it is not stable, so I get rid
of this kind of value.
            x(jj,vv)=NaN;
        end
        if y(jj,vv)==0
            y(jj,vv)=NaN;
        end
    end
end
sigmax=zeros(2002,2002);
sigmay=zeros(2002,2002);
sigmaz=zeros(2002,2002);
taoxy=zeros(2002,2002);
taoxz=zeros(2002,2002);
taoyz=zeros(2002,2002);

hoop=zeros(2002,2002);
radial=zeros(2002,2002);

z1=x+miu1.*y;
z2=x+miu2.*y;
z3=x+miu3.*y;

eta1=(z1./a+((z1./a).^2-1-miu1^2).^0.5)./(1-1i*miu1);
```

```
eta2=(z2./a+((z2./a).^2-1-miu2^2).^0.5)./(1-1i*miu2);
eta3=(z3./a+((z3./a).^2-1-miu3^2).^0.5)./(1-1i*miu3);

phi1=-(1./(2*triangle.*eta1.*((z1./a).^2-1-miu1^2).^0.5)).*((1i*taoxy0-
sigmay0+pw).*(miu2-lamda2*lamda3*miu3)+(taoxy0-
1i*sigmax0+1i*pw).*(lamda2*lamda3-1)+(taoyz0-1i*taoxz0)*lamda3*(miu3-miu2));
phi2=-(1./(2*triangle.*eta2.*((z2./a).^2-1-miu2^2).^0.5)).*((1i*taoxy0-
sigmay0+pw).*(lamda1*lamda3*miu3-miu1)+(taoxy0-1i*sigmax0+1i*pw).*(1-
lamda1*lamda3)+(taoyz0-1i*taoxz0)*lamda3*(miu1-miu3));
phi3=-(1./(2*triangle.*eta3.*((z3./a).^2-1-miu3^2).^0.5)).*((1i*taoxy0-
sigmay0+pw).*(lamda2*miu1-lamda1*miu2)+(taoxy0-1i*sigmax0+1i*pw).*(lamda1-
lamda2)+(taoyz0-1i*taoxz0)*(miu2-miu1));

sigmax(1:2002,1002:2002)=sigmax0+2.*real(miu1^2.*phi1+miu2^2.*phi2+lamda3*miu
3^2.*phi3);
sigmay(1:2002,1002:2002)=sigmay0+2.*real(phi1+phi2+lamda3.*phi3);
taoxy(1:2002,1002:2002)=taoxy0-
2.*real(miu1.*phi1+miu2.*phi2+lamda3*miu3.*phi3);
taoxz(1:2002,1002:2002)=taoxz0+2.*real(lamda1*miu1.*phi1+lamda2*miu2.*phi2+mi
u3.*phi3);
taoyz(1:2002,1002:2002)=taoyz0-2.*real(lamda1.*phi1+lamda2.*phi2+phi3);
sigmaz(1:2002,1002:2002)=sigmaz0-
(a13*2.*real((miu1^2).*phi1+(miu2^2).*phi2+lamda3*miu3^2.*phi3)+a23*(2.*real(
phi1+phi2+lamda3.*phi3))+a34.*(-
2.*real(lamda1.*phi1+lamda2.*phi2+phi3))+a35.*(2.*real(lamda1*miu1.*phi1+lamd
a2*miu2.*phi2+miu3.*phi3))+a36.*(-
2.*real(miu1.*phi1+miu2.*phi2+lamda3*miu3.*phi3))./a33;

theta=atan2(y,x);

hoop(1:2002,1002:2002)=(sin(theta)).^2.*sigmax(1:2002,1002:2002)+(cos(theta))
.^2.*sigmay(1:2002,1002:2002)-sin(2.*theta).*taoxy(1:2002,1002:2002);
radial(1:2002,1002:2002)=sigmax(1:2002,1002:2002).*(cos(theta)).^2+(sin(theta
)).^2.*sigmay(1:2002,1002:2002)+sin(2.*theta).*taoxy(1:2002,1002:2002);

%% the other half
X2=linspace(-5,0,1001);
Y2=linspace(-5,5,2002);
[x,y]=meshgrid(X2,Y2);

for jj=1:2002
    for vv=1:1001
        r=((x(jj,vv))^2+(y(jj,vv))^2);
        if r<a
            x(jj,vv)=NaN;
            y(jj,vv)=NaN;
        end
        if x(jj,vv)==0
            x(jj,vv)=NaN;
        end
        if y(jj,vv)==0
            y(jj,vv)=NaN;
        end
    end
end
```

```
z1=x+miu1.*y;
z2=x+miu2.*y;
z3=x+miu3.*y;

eta1=(-z1./a+((z1./a).^2-1-miu1^2).^0.5)./(1-1i*miu1);
eta2=(-z2./a+((z2./a).^2-1-miu2^2).^0.5)./(1-1i*miu2);
eta3=(-z3./a+((z3./a).^2-1-miu3^2).^0.5)./(1-1i*miu3);

phi1=-(1./(2*triangle.*eta1.*((z1./a).^2-1-miu1^2).^0.5)).*((1i*taoxy0-
sigmay0+pw).*(miu2-lamda2*lamda3*miu3)+(taoxy0-
1i*sigmax0+1i*pw).*(lamda2*lamda3-1)+(taoyz0-1i*taoxz0)*lamda3*(miu3-miu2));
phi2=-(1./(2*triangle.*eta2.*((z2./a).^2-1-miu2^2).^0.5)).*((1i*taoxy0-
sigmay0+pw).*(lamda1*lamda3*miu3-miu1)+(taoxy0-1i*sigmax0+1i*pw).*(1-
lamda1*lamda3)+(taoyz0-1i*taoxz0)*lamda3*(miu1-miu3));
phi3=-(1./(2*triangle.*eta3.*((z3./a).^2-1-miu3^2).^0.5)).*((1i*taoxy0-
sigmay0+pw).*(lamda2*miu1-lamda1*miu2)+(taoxy0-1i*sigmax0+1i*pw).*(lamda1-
lamda2)+(taoyz0-1i*taoxz0)*(miu2-miu1));

sigmax(1:2002,1:1001)=sigmax0+2.*real(miu1^2.*phi1+miu2^2.*phi2+lamda3*miu3^2
.*phi3);
sigmay(1:2002,1:1001)=sigmay0+2.*real(phi1+phi2+lamda3.*phi3);
taoxy(1:2002,1:1001)=taoxy0-2.*real(miu1.*phi1+miu2.*phi2+lamda3*miu3.*phi3);
taoxz(1:2002,1:1001)=taoxz0+2.*real(lamda1*miu1.*phi1+lamda2*miu2.*phi2+miu3.
*phi3);
taoyz(1:2002,1:1001)=taoyz0-2.*real(lamda1.*phi1+lamda2.*phi2+phi3);
sigmaz(1:2002,1:1001)=sigmaz0-
(a13*2.*real((miu1^2).*phi1+(miu2^2).*phi2+lamda3*miu3^2.*phi3)+a23.*(2.*real
(phi1+phi2+lamda3.*phi3))+a34.*(-
2.*real(lamda1.*phi1+lamda2.*phi2+phi3))+a35.*(2.*real(lamda1*miu1.*phi1+lamd
a2*miu2.*phi2+miu3.*phi3))+a36.*(-
2.*real(miu1.*phi1+miu2.*phi2+lamda3*miu3.*phi3))./a33;

theta=atan2(y,x);

hoop(1:2002,1:1001)=(sin(theta)).^2.*sigmax(1:2002,1:1001)+(cos(theta)).^2.*s
igmay(1:2002,1:1001)-sin(2.*theta).*taoxy(1:2002,1:1001);
radial(1:2002,1:1001)=sigmax(1:2002,1:1001).*(cos(theta)).^2+(sin(theta)).^2.
*sigmay(1:2002,1:1001)+sin(2.*theta).*taoxy(1:2002,1:1001);

X(1:1001)=X2;
X(1002:2002)=X1;

[x,y]=meshgrid(X,Y2);

figure(1);
pcolor(x,y,sigmax);
title('sigmax');
shading interp;
colorbar;
axis square;

figure(2);
pcolor(x,y,sigmay);
title('sigmay');
```

```
 shading interp;
 colorbar;
 axis square;

figure(3);
pcolor(x,y,sigmaz);
title('sigmaz & axial stress');
shading interp;
 colorbar;
 axis square;

figure(4);
pcolor(x,y,taoxy);
title('taoxy');
shading interp;
 colorbar;
 axis square;

figure(5);
pcolor(x,y,taoxz);
title('taoxz');
 shading interp;
 colorbar;
 axis square;

 figure(6);
pcolor(x,y,taoyz);
title('taoyz');
 shading interp;
 colorbar;
 axis square;

figure(7);
 pcolor(x,y,hoop);
title('hoop');
 shading interp;
colorbar;
axis square;

figure(8);
 pcolor(x,y,radial);
 title('radial stress');
 shading interp;
colorbar;
axis square;
```

Stress_transformation.m

```
function
[sigma_borehole]=stress_transformation(xx,yy,zz,taoyz,taozx,taoxy,beta1,alpha
1,beta2,alpha2)
% This function calculates the stress transformation from stress coordinate
% to borehole coordinate. (Maria's thesis)
% beta1, alpha1 are angle for borehole system with respect to the global
```

```
% coordinate system
% beta2, alpha2 are angle for global system with respect to the global one.
% beta is inclination, alpha is azimuth counterclockwise from x axis.

sigma=[xx;yy;zz;taoyz;taozx;taoxy];

beta1=beta1*pi/180;
alpha1=alpha1*pi/180;
beta2=beta2*pi/180;
alpha2=alpha2*pi/180;

% sigma_borehole=O*R'*sigma

lxa=cos(beta1)*cos(alpha1);
mxa=cos(beta1)*sin(alpha1);
nxa=-sin(beta1);
lya=-sin(alpha1);
mya=cos(alpha1);
nya=0;
lza=sin(beta1)*cos(alpha1);
mza=sin(beta1)*sin(alpha1);
nza=cos(beta1);

O=[lxa^2,mxa^2,nxa^2,2*mxa*nxa,2*nxa*lxa,2*lxa*mxa;
    lya^2,mya^2,nya^2,2*mya*nya,2*nya*lya,2*lya*mya;
    lza^2,mza^2,nza^2,2*mza*nza,2*nza*lza,2*lza*mza;
    lya*lza,mya*mza,nya*nza,mya*nza+mza*nya,nya*lza+nza*lya,lya*mza+lza*mya;
    lza*lxa,mza*mxa,nza*nxa,mxa*nza+mza*nxa,nxa*lza+nza*lxa,lxa*mza+lza*mxa;
    lxa*lya,mxa*mya,nxa*nya,mxa*nya+mya*nxa,nxa*lya+nya*lxa,lxa*mya+lya*mxa];

lx=cos(beta2)*cos(alpha2);
mx=cos(beta2)*sin(alpha2);
nx=-sin(beta2);
ly=-sin(alpha2);
my=cos(alpha2);
ny=0;
lz=sin(beta2)*cos(alpha2);
mz=sin(beta2)*sin(alpha2);
nz=cos(beta2);

R=[lx^2,mx^2,nx^2,mx*nx,nx*lx,lx*mx;
    ly^2,my^2,ny^2,my*ny,ny*ly,ly*my;
    lz^2,mz^2,nz^2,mz*nz,nz*lz,lz*mz;
    2*ly*lz,2*my*mz,2*ny*nz,my*nz+mz*ny,ny*lz+nz*ly,ly*mz+lz*my;
    2*lz*lx,2*mz*mx,2*nz*nx,mx*nz+mz*nx,nx*lz+nz*lx,lx*mz+lz*mx;
    2*lx*ly,2*mx*my,2*nx*ny,mx*ny+my*nx,nx*ly+ny*lx,lx*my+ly*mx];

O(abs(O)<power(10,-10))=0;
R(abs(R)<power(10,-10))=0;

sigma_borehole=O*(R.')*sigma;
```

compliance_transformation.m

```
function [A]=compliance_transformation(beta1,alpha1,beta2,alpha2,Compliance)
% This function calculates the compliance transformation
% A=T2*T1t*H*T1*T2t (Maria, 2010)
% t1=tilt angle of the anisotropy with respect to the global coordinate
% a1=azimuth of the anisotropy with respect to the global coordinate
% t2=tilt angle of the borehole with respect to the global coordinate
% a2=azimuth of the borehole with respect to the global coordinate.
beta1=beta1*pi/180;
alpha1=alpha1*pi/180;
beta2=beta2*pi/180;
alpha2=alpha2*pi/180;
%% direction cosines of the unit vector in the rectilinear anisotropy
directions

lxa=cos(beta1)*cos(alpha1);
mxa=cos(beta1)*sin(alpha1);
nxa=-sin(beta1);
lya=-sin(alpha1);
mya=cos(alpha1);
nya=0;
lza=sin(beta1)*cos(alpha1);
mza=sin(beta1)*sin(alpha1);
nza=cos(beta1);

T1=[lxa^2,mxa^2,nxa^2,2*mxa*nxa,2*nxa*lxa,2*lxa*mxa;
    lya^2,mya^2,nya^2,2*mya*nya,2*nya*lya,2*lya*mya;
    lza^2,mza^2,nza^2,2*mza*nza,2*nza*lza,2*lza*mza;
    lya*lza,mya*mza,nya*nza,mya*nza+mza*nya,nya*lza+nza*lya,lya*mza+lza*mya;
    lza*lxa,mza*mxa,nza*nxa,mxa*nza+mza*nxa,nxa*lza+nza*lxa,lxa*mza+lza*mxa;
    lxa*lya,mxa*mya,nxa*nya,mxa*nya+mya*nxa,nxa*lya+nya*lxa,lxa*mya+lya*mxa];

%% direction cosines of the unit vector in the borehole coordinate

lx=cos(beta2)*cos(alpha2);
mx=cos(beta2)*sin(alpha2);
nx=-sin(beta2);
ly=-sin(alpha2);
my=cos(alpha2);
ny=0;
lz=sin(beta2)*cos(alpha2);
mz=sin(beta2)*sin(alpha2);
nz=cos(beta2);

T2=[lx^2,mx^2,nx^2,mx*nx,nx*lx,lx*mx;
    ly^2,my^2,ny^2,my*ny,ny*ly,ly*my;
    lz^2,mz^2,nz^2,mz*nz,nz*lz,lz*mz;
    2*ly*lz,2*my*mz,2*ny*nz,my*nz+mz*ny,ny*lz+nz*ly,ly*mz+lz*my;
    2*lz*lx,2*mz*mx,2*nz*nx,mx*nz+mz*nx,nx*lz+nz*lx,lx*mz+lz*mx;
    2*lx*ly,2*mx*my,2*nx*ny,mx*ny+my*nx,nx*ly+ny*lx,lx*my+ly*mx];

T1(abs(T1)<power(10,-10))=0;
T2(abs(T2)<power(10,-10))=0;
```

```
%%
A=T2*(T1.')*Compliance*T1*(T2.');
end
```

Appendix C

MATLAB Code for Borehole Tensile Fracture Tracing in Anisotropic Materials

```
% Fracture tracing (tensile only). Anisotropice case
% This program doesn't consider fracture width.

%%%%%%%%%%%%%%%%%%%%%%%%%%%%%COPYRIGHT%%%%%%%%%%%%%%%%%%%%%%%%%%%%%%%%%%%%%%%
% This program was written for research purposes.
% AUTHOR:Qing Jia
% University of Alberta
% qjia@ualberta.ca
%%%%%%%%%%%%%%%%%%%%%%%%%%%%%COPYRIGHT ENDS%%%%%%%%%%%%%%%%%%%%%%%%%%%%%%%%%%%%

clear all;
close all;

%% dimensions of the mesh (can be changed)
length0=1;
width=2;
nex=200;
ney=200;   % Number of elements along x and y axis.
% nex>=ney

%%
Nelement = nex*ney;    % Number of elements in the Mesh;
NodeEle = 4;         % Number of nodes per element
npx = nex+1;
npy = ney+1;           % Number of nodes along x and y axis
nnode = npx*npy;       % Number of nodes in the whole mesh

%% Discretization
nx = linspace(0,length0,npx);
ny = linspace(0,width,npy);
[x,y]=meshgrid(nx,ny);

%% Nodal connectivity matrix
coordinates = [x(:) y(:)];
[m,n] = size(coordinates); % m is the number of points in the mesh

theta=coordinates(:,1);
height=coordinates(:,2);

theta=2*pi.*theta/length0;

%% stress deteremination and assign to each point
% assume the stress is aligned with the global coordinate.
sigmax0 = 50;
sigmay0 = 10;
Sv = 20;
inclination = 50;
```

```
azimuth = 40;
poisson = 0.25;
pw = 0;
sigma_borehole=stress_transformation(sigmax0,sigmay0,Sv,0,0,0,inclination,azi
muth,0,0);

sigmax0=sigma_borehole(1);
sigmay0=sigma_borehole(2);
sigmaz0=sigma_borehole(3);
taoxy0=sigma_borehole(6);
taoxz0=sigma_borehole(5);
taoyz0=sigma_borehole(4);

% elastic constants
c11=40.2326;
c13=15.2456;
c33=28.2326;
c44=9.8684;
c66=12;
c12=c11-2*c66;
c22=c11;
c23=c13;

S=[c11,c12,c13,0,0,0;
    c12,c22,c23,0,0,0;
    c13,c23,c33,0,0,0;
    0,0,0,c44,0,0;
    0,0,0,0,c44,0;
    0,0,0,0,0,c66];

A1=S^(-1);
A=compliance_transformation(0,0,inclination,azimuth,A1);

a11=A(1,1);
a12=A(1,2);
a13=A(1,3);
a21=A(2,1);
a22=A(2,2);
a23=A(2,3);
a33=A(3,3);
a34=A(3,4);
a35=A(3,5);
a36=A(3,6);
a44=A(4,4);
a66=A(6,6);

beta55=A(5,5)-(A(5,3)*A(5,3))/a33;
beta45=A(4,5)-(A(4,3)*A(5,3))/a33;
beta44=A(4,4)-(A(4,3)*A(4,3))/a33;
beta11=A(1,1)-(A(1,3)*A(1,3))/a33;
beta16=A(1,6)-(A(1,3)*A(6,3))/a33;
beta12=A(1,2)-(A(1,3)*A(2,3))/a33;
beta66=A(6,6)-(A(6,3)*A(6,3))/a33;
beta26=A(2,6)-(A(2,3)*A(6,3))/a33;
beta22=A(2,2)-(A(2,3)*A(2,3))/a33;
beta15=A(1,5)-(A(1,3)*A(5,3))/a33;
```

```
beta14=A(1,4)-(A(1,3)*A(4,3))/a33;
beta56=A(5,6)-(A(5,3)*A(6,3))/a33;
beta25=A(2,5)-(A(2,3)*A(5,3))/a33;
beta46=A(4,6)-(A(4,3)*A(6,3))/a33;
beta24=A(2,4)-(A(2,3)*A(4,3))/a33;

p1=[beta55,-2*beta45,beta44];
p2=[beta11,-2*beta16,(2*beta12+beta66),-2*beta26,beta22];

miu11=roots(p1);
miu22=roots(p2);

miu3=miu11(1);
miu1=miu22(1);
miu2=miu22(3);

l2_miu1=beta55*miu1^2-2*beta45*miu1+beta44;
l2_miu2=beta55*miu2^2-2*beta45*miu2+beta44;
l2_miu3=beta55*miu3^2-2*beta45*miu3+beta44;

l3_miu1=beta15*miu1^3-(beta14+beta56)*miu1^2+(beta25+beta46)*miu1-beta24;
l3_miu2=beta15*miu2^3-(beta14+beta56)*miu2^2+(beta25+beta46)*miu2-beta24;
l3_miu3=beta15*miu3^3-(beta14+beta56)*miu3^2+(beta25+beta46)*miu3-beta24;

if l2_miu1==0
    lamda1=0;
else
lamda1=-l3_miu1/l2_miu1;
end

if l2_miu2==0
    lamda2=0;
else
lamda2=-l3_miu2/l2_miu2;
end

if l2_miu3==0
    lamda3=0;
else
lamda3=-l3_miu3/l2_miu3;
end

triangle=miu2-miu1+lamda2*lamda3*(miu1-miu3)+lamda1*lamda3*(miu3-miu2);

D=(pw-sigmax0).*cos(theta)-taoxy0.*sin(theta)-1i.*((pw-
sigmax0).*sin(theta)+taoxy0.*cos(theta));
E=-(pw-sigmay0).*sin(theta)+taoxy0.*cos(theta)-1i.*((pw-
sigmay0).*cos(theta)+taoxy0.*sin(theta));
F=-taoxz0.*cos(theta)-taoyz0.*sin(theta)-1i.*(taoyz0.*cos(theta)-
taoxz0.*sin(theta));

phi1=(D.*(lamda2*lamda3-1)+E.*(miu2-lamda2*lamda3*miu3)+F.*(miu3-
miu2)*lamda3)./(2.*triangle.*(miu1.*cos(theta)-sin(theta)));
phi2=(D.*(1-lamda1*lamda3)+E.*(lamda1*lamda3*miu3-miu1)+F.*(miu1-
miu3)*lamda3)./(2.*triangle.*(miu2.*cos(theta)-sin(theta)));
```

```
phi3=(D.*(lamda1-lamda2)+E.*(miu1*lamda2-miu2*lamda1)+F.*(miu2-
miu1))./(2.*triangle.*(miu3.*cos(theta)-sin(theta)));

sigmax=sigmax0+2.*real(miu1^2.*phi1+miu2^2.*phi2+lamda3*miu3^2.*phi3);
sigmay=sigmay0+2.*real(phi1+phi2+lamda3.*phi3);
taoxy=taoxy0-2.*real(miu1.*phi1+miu2.*phi2+lamda3*miu3.*phi3);
taoxz=taoxz0+2.*real(lamda1*miu1.*phi1+lamda2*miu2.*phi2+miu3.*phi3);
taoyz=taoyz0-2.*real(lamda1.*phi1+lamda2.*phi2+phi3);
sigmaz=sigmaz0-
(a13*2.*real((miu1^2).*phi1+(miu2^2).*phi2+lamda3*miu3^2.*phi3)+a23*(2*real(p
hi1+phi2+lamda3.*phi3))+a34.*(taoyz-taoyz0)+a35.*(taoxz-taoxz0)+a36.*(taoxy-
taoxy0))/a33;

hoop=(sin(theta)).^2.*sigmax+(cos(theta)).^2.*sigmay-sin(2.*theta).*taoxy;
axial = sigmaz;
tao_hoop_axial = cos(theta).*taoyz-sin(theta).*taoxz;

min_stress=0.5.*(hoop+axial)-0.5.*((hoop-
axial).^2+4.*tao_hoop_axial.^2).^0.5;

% normalized by Sv
min_stress = min_stress./Sv;
color_number=length(unique(min_stress));
% Assign colors
% Make sure that the color of colorbar colors(ii) is in the arrange as
min_stress(ID(ii))
[nothing ID]=sort(min_stress);
colors1=colormap(gray(color_number));

colors=zeros(m,3);
colors(1,:)=colors1(1,:);
jj=1;
for ii=2:m
    if min_stress(ID(ii))==min_stress(ID(ii-1))
        colors(ii,:)=colors(ii-1,:);
    else
        jj=jj+1;
        colors(ii,:)=colors1(jj,:);
    end
end

figure(1);
subplot(2,1,1);
scatter(theta(ID(:)),height(ID(:)),10,colors);
% Plot stress point from the smallest to the largest and plot the color
corespondingly.
xlim([min(theta),max(theta)]);
set(gca,'ytick',[]);
ylabel('height');
xlabel('theta (unwrapped borehole wall)');
h = colorbar;
hold on;

if min(min_stress) ~= max(min_stress)
    set(gca,'CLim',[min(min_stress),max(min_stress)]);
```

```
    colorbar;
elseif min_stress(:) == 0
    disp('minimum stress value equals to zero');
else
    printf('minimum stress equals to %d\n',min_stress);
end

%% find the greatest principal tensile stress within the mesh, which is the
initiation point of fractures

max_tensile = min(min_stress(:));

if max_tensile>=0
    error('no tensile fracture');
end

if max(min_stress(:)) <= 0
    error('borehole fail');
end

ID1=find(min_stress==max_tensile);

% based on the azimuth and nodes number in x direction, system sometimes
% can only detect one max tensile straw. Therefore, if that happens, we
% arbitrarily define the second max tensile straw, which may not be accurate.
if length(ID1) < 2*npy && ID1(1) < nnode/2 % the detected max tensile line is
on the left side
    ID2 = [ID1;ID1+((npx-1)/2)*npy];
    ID1 = ID2;
elseif length(ID1) < 2*npy && ID1(1) > nnode/2
    ID2 = [ID1;ID1-((npx-1)/2)*npy];
    ID1 = ID2;
end

if inclination==0
    % the trace will be a vertical line which is aligned with the borehole
    % axis.

    xx=zeros(length(ID1),1);
    yy=zeros(length(ID1),1);

    for ii=1:length(ID1)
        xx(ii)=theta(ID1(ii));
        yy(ii)=height(ID1(ii));
    end

    line(xx(1:npy),yy(1:npy),'LineWidth',5,'Color','g');
    hold on;
    line(xx(npy+1:2*npy),yy(npy+1:2*npy),'LineWidth',5,'Color','g');
    hold off;
else
   % The borehole is inclined, so the fracture will not be vertical.
   % Find the start point with max tensile, and it is set to be on the top
   % of the figure.
   ID_max_height=zeros(2,1);
```

```
   mm=1;
   for ii=1:length(ID1)
       if height(ID1(ii))==fix(width) % initiation point is in the middle of
the width
           if mm==3
               break; % Avoiding three tensile azimuth initiation places
           end
           ID_max_height(mm)=ID1(ii);
           mm=1+mm;
       end
   end
   % Finding which straw is the first fracture in.
   straw_number = fix(ID_max_height(1)/npy);
   straw_number2 = fix(ID_max_height(2)/npy);

   %% Calculating slope
   % Check if the gamma is negative, for negative gamma, reverse theta to
   % display
   aa = 2.*tao_hoop_axial(ID_max_height(:));
   bb = hoop(ID_max_height(:))-axial(ID_max_height(:));

   gamma_check = 0.5.*atan2(aa,bb);

   if abs(gamma_check(1)) == pi/2   % Since gamma_check(1) should be the
opposite of gamma_check(2), we only check the first one.
       xx=zeros(length(ID1),1);
       yy=zeros(length(ID1),1);

    for ii=1:length(ID1)
        xx(ii)=theta(ID1(ii));
        yy(ii)=height(ID1(ii));
    end

       line(xx(1:npy),yy(1:npy),'LineWidth',5,'Color','g');
       hold on;
       line(xx(npy+1:2*npy),yy(npy+1:2*npy),'LineWidth',5,'Color','g');
       hold off;
       [theta_unique,rows_theta_o1]=unique(theta);
   else
   ff=gamma_check>0;

   [theta_unique,rows_theta_o1]=unique(theta);

   rows_theta1 = rows_theta_o1(straw_number:end);
   rows_theta2 = rows_theta_o1(1:straw_number-1);
   rows_theta = [rows_theta1;rows_theta2];
   if ff(1)==1 % gamma_check(1) is negative, everything in right sequence.
   % make rows_theta in the right sequence
      rows_theta_reverse=zeros(length(rows_theta),1);
      rows_theta_reverse(1)=rows_theta(1);
      rows_theta_reverse(2:end)=rows_theta(end:-1:2);
      rows_theta = rows_theta_reverse;
   end

   rows_theta1 = rows_theta_o1(straw_number2:end);
```

```
    rows_theta2 = rows_theta_o1(1:straw_number2-1);
    rows_theta2 = [rows_theta1;rows_theta2];

    if ff(2)==1
       rows_theta_reverse=zeros(length(rows_theta2),1);
       rows_theta_reverse(1)=rows_theta2(1);
       rows_theta_reverse(2:end)=rows_theta2(end:-1:2);
       rows_theta2 = rows_theta_reverse;
    end

    % put the reverse one as the second line
    if ff(1)==1
        rows_theta_test=rows_theta2;
        rows_theta2=rows_theta;
        rows_theta=rows_theta_test;
    end

    % Eliminate boundary side-effect
    if theta(rows_theta(1)) == max(max(theta))
        rows_theta = rows_theta(2:end);
    end

    if theta(rows_theta2(1)) == 0
        rows_theta2 = rows_theta2(2:end);
    end

    line_stops=find(min_stress(rows_theta)>=0);
    rows_theta_o=rows_theta(1:line_stops-1);

    line_stops2 = find(min_stress(rows_theta2)>=0);
    rows_theta2_o=rows_theta2(1:line_stops2-1);

    gamma = 0.5.*atan2(2.*tao_hoop_axial(rows_theta_o),(hoop(rows_theta_o)-
axial(rows_theta_o)));
    gamma2 = 0.5.*atan2(2.*tao_hoop_axial(rows_theta2_o),(hoop(rows_theta2_o)-
axial(rows_theta2_o)));

    % check if the gamma change signs during propagation. the number of
    % gamma of be limited by ney/2
    oo1 = gamma(:) > 0;
    rows_reverse1 = find(oo1 == 1);

    if sum(oo1) >= 1 && rows_reverse1(1) ~= length(oo1)
        rows_reverse = rows_reverse1(1);
        gamma = 0.5.*atan2(2.*tao_hoop_axial(rows_theta),(hoop(rows_theta)-
axial(rows_theta)));
        gamma(rows_reverse+1:2:end) = gamma(rows_reverse-1);
        gamma(rows_reverse+2:2:end) = gamma(rows_reverse);
        rows_theta(rows_reverse+1:2:end) = rows_theta(rows_reverse-1);
        rows_theta(rows_reverse+2:2:end) = rows_theta(rows_reverse);
    else
        rows_theta = rows_theta_o;
    end

    oo2 = gamma2(:) < 0;
```

```
    rows_reverse2 = find(oo2 == 1);

    if sum(oo2) >= 1 && rows_reverse2(1) ~= length(oo2);
        rows_reverse = rows_reverse2(1);
        gamma2 = 0.5.*atan2(2.*tao_hoop_axial(rows_theta2),(hoop(rows_theta2)-
axial(rows_theta2)));
        gamma2(rows_reverse+1:2:end) = gamma2(rows_reverse-1);
        gamma2(rows_reverse+2:2:end) = gamma2(rows_reverse);
        rows_theta2(rows_reverse+1:2:end) = rows_theta2(rows_reverse-1);
        rows_theta2(rows_reverse+2:2:end) = rows_theta2(rows_reverse);
    else
        rows_theta2 = rows_theta2_o;
    end

    slope = tan(gamma);
    slope2 = tan(gamma2);
    % gamma is the angle between the direction vertical to the direction
    % of maximum tensile and the direction parallel to the borehole
    % axis.
    % Take absolute value of slope since slopes are in opposite sign for two
    % opposite positions.

    %% Calculate yy
    mm=length(rows_theta);
    nn=length(rows_theta2);
    yy1=zeros(1,mm);
    yy2 = zeros(1,nn);
    yy1(1)=height(ID_max_height(1));
    yy2(1)=yy1(1);
    control = 0;

    for ii=2:mm % ney straw in total, take only half of them
        % starting from the initial point, the fracture trace follows the
        % direction vertical to the minimum compressive stress.
        % Then try to find the intersection point between the trace and the
        % neighbour straw.

        if theta(rows_theta(ii))==0 && control~=1
            intercept=yy1(ii-1);
            yy1(ii) = yy1(ii-1);
            control = 1;
        else
            intercept = yy1(ii-1)-slope(ii-1)*theta(rows_theta(ii-1));
            yy1(ii) = slope(ii-1)*theta(rows_theta(ii))+intercept;
        end

    end

    for ii=2:nn
        if theta(rows_theta2(ii))==2*pi && control ~= 2
            intercept2=yy2(ii-1);
            yy2(ii) = yy2(ii-1);
            control = 2;
        else
            intercept2 = yy2(ii-1)-slope2(ii-1)*theta(rows_theta2(ii-1));
```

```
            yy2(ii) = slope2(ii-1)*theta(rows_theta2(ii))+intercept2;
        end

    end
    yy1(yy1<0) = NaN;
    yy2(yy2<0) = NaN;

    xx1 = theta(rows_theta(:));
    xx2 = theta(rows_theta2(:));

    %% Eliminate lines drew across the whole figure.

    decrease_row = 0;
    decrease_row2 = 0;

    for ii = 2:mm
        if xx1(ii) < xx1(ii-1) && xx1(ii) == 0
            decrease_row = ii;
            break;
        end
    end

    if decrease_row ~= 0 % to confirm if there is any cross through the whole
figure
        line(xx1(1:decrease_row-1),yy1(1:decrease_row-
1),'LineWidth',5,'Color','g');

line(xx1(decrease_row:end),yy1(decrease_row:end),'LineWidth',5,'Color','g');
        hold on;
    else
        line(xx1(:),yy1(:),'LineWidth',5,'Color','g');
        hold on;
    end

    for ii = 2:nn
        if xx2(ii) > xx2(ii-1) && xx2(ii) == 2*pi
            decrease_row2 = ii;
            break;
        end
    end

    if decrease_row2 ~= 0 % to confirm if there is any cross through the whole
figure
        line(xx2(1:decrease_row2-1),yy2(1:decrease_row2-
1),'LineWidth',5,'Color','g');

line(xx2(decrease_row2:end),yy2(decrease_row2:end),'LineWidth',5,'Color','g')
;
        hold off;
    else
        line(xx2(:),yy2(:),'LineWidth',5,'Color','g');
        hold off;
    end
    end
```

```
gamma_plot =
0.5.*atan2(2.*tao_hoop_axial(rows_theta_o1),(hoop(rows_theta_o1)-
axial(rows_theta_o1)));
subplot(2,1,2);
plot(theta_unique,gamma_plot);
xlabel('theta');
ylabel('fracture inclinations');
end
```